

NASA TECHNICAL
MEMORANDUM

NASA TM X-64772

APOLLO 17 HEAT FLOW AND CONVECTION EXPERIMENTS

FINAL DATA ANALYSES RESULTS

By T. C. Bannister, P. G. Grodzka, L. W. Spradley,
S. V. Bourgeois, R. O. Hedden, and B. R. Facemire
Space Sciences Laboratory

CASE FILE
COPY

July 16, 1973

NASA

*George C. Marshall Space Flight Center
Marshall Space Flight Center, Alabama*

1. REPORT NO. NASA TM X-64772		2. GOVERNMENT ACCESSION NO.		3. RECIPIENT'S CATALOG NO.	
4. TITLE AND SUBTITLE Apollo 17 Heat Flow and Convection Experiments Final Data Analyses Results				5. REPORT DATE July 16, 1973	
7. AUTHOR(S) T.C. Bannister, P.G. Grodzka, * L.W. Spradley, * S.V. Bourgeois, * R.O. Hedden, * and B.R. Facemire				6. PERFORMING ORGANIZATION CODE	
9. PERFORMING ORGANIZATION NAME AND ADDRESS George C. Marshall Space Flight Center Marshall Space Flight Center, Alabama 35812				8. PERFORMING ORGANIZATION REPORT #	
12. SPONSORING AGENCY NAME AND ADDRESS National Aeronautics and Space Administration Washington, D. C. 20546				10. WORK UNIT NO. OMSF 975-90-95-1500	
				11. CONTRACT OR GRANT NO. NAS8-25577	
15. SUPPLEMENTARY NOTES Prepared by Space Sciences Laboratory, Science and Engineering *Lockheed Missiles and Space Co., Inc.				13. TYPE OF REPORT & PERIOD COVERED Technical Memorandum	
				14. SPONSORING AGENCY CODE	
16. ABSTRACT <p>A group of experiments called the Apollo 17 Heat Flow and Convection (HFC) Experiments was conducted by Astronaut Ron Evans on December 8, 1972, aboard the Apollo 17 spacecraft while in translunar coast on the way to the moon. These experiments together with the HFC experiments flown on Apollo 14 demonstrated and provided data on two types of low-g natural convection: cellular, surface tension-driven convection and convection in confined fluids caused by spacecraft and astronaut movements. Observed convection onset times show that surface tension-driven convection occurs at lower temperature gradients in low-g than in one-g environments. Data on heat flow in confined fluids show that spacecraft and astronaut movements can cause significant degrees of convection.</p> <p style="text-align: center;">EDITOR'S NOTE</p> <p>Use of trade names or names of manufacturers in this report does not constitute an official endorsement of such products or manufacturers, either express or implied, by the National Aeronautics and Space Administration or any other agency of the United States government.</p>					
17. KEY WORDS			18. DISTRIBUTION STATEMENT Unclassified - Unlimited <i>Tommy C Bannister</i>		
19. SECURITY CLASSIF. (of this report) Unclassified		20. SECURITY CLASSIF. (of this page) Unclassified		21. NO. OF PAGES 164	22. PRICE NTIS

ACKNOWLEDGMENTS

The Apollo 17 Heat Flow and Convection team wishes to express its thanks to Astronauts Ronald E. Evans and Stuart A. Roosa. Their enthusiastic interest and careful performance of the Heat Flow and Convection (HFC) Experiments were in large measure responsible for the successes achieved.

The indispensable guidance, suggestions, and management skills of Dr. James H. Bredt, NASA Headquarters, and Mr. Brian O. Montgomery, George C. Marshall Space Flight Center (MSFC), as well as the assistance of a number of individuals at the Johnson Space Center and the Kennedy Space Center are also acknowledged.

The successful outcome of the Apollo 17 HFC experiments also is undoubtedly the result of the outstanding team spirit which pervaded the entire project. The NASA-Lockheed team worked together on the apparatus design, research and development, fabrication, and data analysis with an enthusiasm and dedication that inspired each member anew. The following people comprised the Apollo 17 MSFC-Lockheed team:

MSFC Members

Tommy C. Bannister
Bernie S. Blake
Barbara Facemire
Larry W. Russell
James Parker
Robert L. Holland
Luke Ginn
Frank Key
John Boggess
David Taylor
Fred Dolan
Ronald P. Harris

Lockheed Members

Philomena G. Grodzka
Paul T. Johnson
John Benefield
Lawrence Spradley
Sidney Bourgeois
Ray Hedden
Paul Biscenius
Kip Heimendinger
Robert A. Wyman
Robert L. Chaney
Gus Marino
Billie Joe Osmer

A number of people assisted with certain phases of the apparatus design and the data analysis. These include:

Fred Rodrigue (NASA)
Ronald Graham (NASA)
Robert L. Holland (NASA)
Dick Saylor (Computer Sciences Corporation)
E. L. Koschmieder (University of Texas)



Astronaut Ron Evans performing the Apollo 17 Heat Flow
and Convection Experiments. (Apparatus is at left
of picture.)

FOREWORD

On December 8, 1972, while the Apollo 17 spacecraft was 145 178 n. mi. from the earth and traveling at the speed of 3543 ft/sec, Astronaut Ronald E. Evans performed a series of experiments called the Apollo 17 Heat Flow and Convection Experiments. The Apollo 17 experiments expand and complement similar experiments conducted aboard the Apollo 14 spacecraft by Astronaut Stuart A. Roosa on February 7, 1971, during the lunar flyback. This report describes the results of an analysis of the Apollo 17 Heat Flow and Convection Experiments data.

TABLE OF CONTENTS

	Page
SUMMARY	1
I. INTRODUCTION.	3
II. EXPERIMENTAL APPARATUS, CONDITIONS, AND PROCEDURES	6
III. FLIGHT RESULTS	20
A. Flow Pattern Experiment.	20
B. Radial and Lineal Heating Experiments	32
IV. INTERPRETATIONS	40
A. Summary of Interpretations	40
B. Flow Pattern Experiment.	40
C. Radial and Lineal Heating Experiments	51
V. IMPLICATIONS FOR SPACE PROCESSING	69
APPENDIX A — APOLLO 17 LIQUID CRYSTAL CALIBRATION STUDIES	72
A. Instrument Errors	75
B. Aging	78
C. Dynamic versus Isothermal	81
D. Different Observers' Sensitivity and Observation Techniques	82
E. Initial Temperature and Heating Rates	82
F. Heating versus Cooling	84
G. Previous Thermal History	84
H. Lighting	85
I. Angle of Viewing	85
J. Pressure and Gravity Effects	85
K. Assignment of Error Bands	85
L. Final Values of Color versus Temperature	86

TABLE OF CONTENTS (Concluded)

	Page
APPENDIX B — UTILITY AND DEFINITION OF PERTINENT DIMENSIONLESS NUMBERS	87
APPENDIX C — ERROR ANALYSES FOR RADIAL AND LINEAL EXPERIMENTS.	92
A. Liquid Crystal Calibration Errors.	92
B. Power Fluctuations.	93
APPENDIX D — CONDUCTION-RADIATION THERMAL MODELS	96
A. Thermal Analysis.	97
B. Thermal Models.	98
C. Radial Heating Temperature-Time Curves	105
D. Lineal Heating Temperature-Time Curves	117
E. Flow Pattern Temperature Profile Curves	129
APPENDIX E — LOCKHEED GENERAL CONVECTION PROGRAM	138
APPENDIX F — REVIEW OF GEBHART'S THEORY OF RANDOM CONVECTION.	142
REFERENCES.	145

LIST OF ILLUSTRATIONS

Figure	Title	Page
1.	Apparatus configuration for the Heat Flow and Convection Demonstration for Apollo 17.	7
2.	Panel face of Apollo 17 Heat Flow and Convection apparatus	8
3.	Details of the Apollo 17 Heat Flow and Convection Experiments	9
4a.	Gravity level in z direction of the HFC apparatus	12
4b.	Gravity level in x direction of the HFC apparatus	13
4c.	Gravity level in y direction of the HFC apparatus	14
5.	Illustration of color bands in a liquid crystal tape	15
6.	Location of liquid crystals on Apollo 17 HFC.	16
7.	Convection cells obtained in 2-mm deep oil during Apollo 17 flight	22
8.	Convection cells obtained in 4-mm deep oil during Apollo 17 flight	23
9.	Convection cells obtained in 2-mm deep oil in ground test. . .	24
10.	Convection cells obtained in 4-mm deep oil in ground test. . .	25
11.	Convection cells obtained in Apollo 14 HFC Experiment	26
12.	Computed thermal profile through 2-mm Krytox layer 18 sec after application of heat.	27

LIST OF ILLUSTRATIONS (Continued)

Figure	Title	Page
13.	Computed thermal profile through 4-mm Krytox layer 48 sec after application of heat	28
14.	Computed thermal profile through 2-mm Krytox layer 2 min after application of heat	29
15.	Computed thermal profile through 4-mm Krytox layer 2 min after application of heat	30
16.	Temperature-time curve at 0.50 cm from Radial heater post	33
17.	Temperature-time curve at 0.75 cm from Radial heater post	34
18.	Temperature-time curve at 0.635 cm from Apollo 14 Radial heater post, heating rate = 5.73 W.	35
19.	Temperature-time curve at 0.9 cm from Apollo 17 Lineal heater, heating rate = 18.0 W	37
20.	Temperature-time curve at 1.1 cm from Apollo 17 Lineal heater, heating rate = 18.0 W	38
21.	Zone heating temperature 3.165 cm from cell center (Apollo 14)	39
22.	Temperature versus time at $r = 0.6$ cm in the Radial cell for varying gravity levels	55
23.	Theoretical isotherm maps at $t = 600$ sec in the Apollo 17 HFC Radial cell	56
24.	Theoretical velocity contour maps at $t = 600$ sec in Apollo 17 HFC Radial cell	57
25.	Bubble displacement in Apollo 14 Zone Heating Cell versus time.	61

LIST OF ILLUSTRATIONS (Continued)

Figure	Title	Page
26.	Comparison of calculated curves assuming various g-levels with Apollo 14 Radial cell data	64
27.	Isotherm plots for a cylinder problem demonstrating the coupling of gravity and thermal expansion convection	65
28.	Attenuation of the effect of vibration with increasing values of Ra	67
A-1.	Illustration of basic isothermal and dynamic concepts.	73
A-2.	Schematic of basic calibration apparatus	75
A-3.	Diagram of the two dynamic test apparatuses used.	76
A-4.	Method of thermocouple attachment.	77
A-5.	Isothermal apparatus, Tests I and II	79
A-6.	Isothermal apparatus, Tests III and IV.	79
A-7.	Illustration of effect of initial temperature	83
C-1.	Voltages at the time of Radial/Lineal run 1.	94
C-2.	Voltages at the time of Radial/Lineal run 2.	95
D-1.	Nodal network for conduction/radiation thermal model of Apollo 17 HFC Radial cell	99
D-2.	Nodal network for conduction thermal model of Apollo 17 HFC Lineal cell	100
D-3.	One-dimensional nodal network for conduction/radiation thermal model of Apollo 17 HFC Flow Pattern cell.	101
D-4.	Radial heating temperature-time curve ($r = 0.5$, run 1)	106

LIST OF ILLUSTRATIONS (Continued)

Figure	Title	Page
D-5.	Radial heating temperature-time curve ($r = 0.6$, run 1)	107
D-6.	Radial heating temperature-time curve ($r = 0.75$, run 1)	108
D-7.	Radial heating temperature-time curve ($r = 0.9$, run 1)	109
D-8.	Radial heating temperature-time curve ($r = 1.2$, run 1)	110
D-9.	Radial heating temperature-time curve ($r = 0.5$, run 2)	111
D-10.	Radial heating temperature-time curve ($r = 0.6$, run 2)	112
D-11.	Radial heating temperature-time curve ($r = 0.75$, run 2)	113
D-12.	Radial heating temperature-time curve ($r = 0.9$, run 2)	114
D-13.	Radial heating temperature-time curve ($r = 1.2$, run 2)	115
D-14.	Lineal heating temperature-time curve ($X = 0.7$, run 1)	118
D-15.	Lineal heating temperature-time curve ($X = 0.9$, run 1)	119
D-16.	Lineal heating temperature-time curve ($X = 1.1$, run 1)	120
D-17.	Lineal heating temperature-time curve ($X = 1.2$, run 1)	121
D-18.	Lineal heating temperature-time curve ($X = 1.5$, run 1)	122
D-19.	Lineal heating temperature-time curve ($X = 0.6$, run 2)	123
D-20.	Lineal heating temperature-time curve ($X = 0.8$, run 2)	124
D-21.	Lineal heating temperature-time curve ($X = 1.1$, run 2)	125
D-22.	Lineal heating temperature-time curve ($X = 1.5$, run 2)	126
D-23.	Lineal heating temperature-time curve ($X = 1.9$, run 2)	127

LIST OF ILLUSTRATIONS (Concluded)

Figure	Title	Page
D-24.	Flow pattern temperature profile curve ($Q = 7.56$, $t = 18$, $T_a = 25^\circ$, $y_m = 1.89$)	130
D-25.	Flow pattern temperature profile curve ($Q = 7.56$, $t = 18$, $T_a = 25^\circ$, $y_m = 2.0$)	131
D-26.	Flow pattern temperature profile curve ($Q = 5.18$, $t = 48$, $T_a = 25^\circ$, $y_m = 3.73$)	132
D-27.	Flow pattern temperature profile curve ($Q = 5.18$, $t = 48$, $T_a = 25^\circ$, $y_m = 4.0$)	133
D-28.	Flow pattern temperature profile curve ($Q = 7.56$, $t = 18$, $T_a = 18.3^\circ$, $y_m = 1.89$)	134
D-29.	Flow pattern temperature profile curve ($Q = 7.56$, $t = 18$, $T_a = 18.3^\circ$, $y_m = 2.0$)	135
D-30.	Flow pattern temperature profile curve ($Q = 5.18$, $t = 48$, $T_a = 18.3^\circ$, $y_m = 3.73$)	136
D-31.	Flow pattern temperature profile curve ($Q = 5.18$, $t = 48$, $T_a = 18.3^\circ$, $y_m = 4.0$)	137
F-1.	Effect of disturbances on heat transfer.	143

LIST OF TABLES

Table	Title	Page
1.	Physical Properties of Apollo 17 and 14 Fluids	10
2.	Apollo 17 HFC Demonstration Experiment — Flight Boundary Conditions	11
3.	Values of Liquid Crystal Dynamic and Isothermal Temperatures	17
4.	Measured Liquid Levels in Flow Pattern Cell	18
5.	Flow Pattern Convection Onset Times for Apollo 17 and Ground Cases	26
6.	Marangoni and Rayleigh Numbers at Flow Pattern Convection Onset	31
7.	Apollo 17 Convection Cell Areas and Diameters.	31
8.	Apollo 17: Manner of Cellular Convection Onset	32
9.	Summary of Theoretical Predictions of Cellular Convection	42
10.	Comparison of Apollo 17 Flow Pattern Results with Pearson's Theory.	43
11.	Flow Pattern Convection Onset Times and Corresponding Marangoni and Rayleigh Numbers	44
12.	Apollo 17 Convection Dimensionless Parameters for Flow Pattern Unit	45
13.	Summary of Literature Conclusions Regarding Nonlinear Temperature Profiles	47
14.	Summary of Assumptions Regarding Surface Deformability	49
D-1.	Thermal and Fluid Properties	102

NOMENCLATURE (Appendix D Not Included)

a	dimensionless wave number
Ac	dimensionless vibratory acceleration
Bi	Biot number
Bo	Bond number
C_n	constant
C_p	specific heat at constant pressure
Cr	Crispation number
d	depth of fluid layer
F_m	dimensionless vibration Fourier number
g	gravity acceleration
g_e	gravity acceleration at the earth's surface (9.80 m/sec^2)
h	convective heat transfer coefficient
H	height of container
k	thermal conductivity
ℓ	diameter of convection cell
L	length of container
Ma	Marangoni number
Ma_c	critical Marangoni number
Nu	Nusselt number without vibration

NOMENCLATURE (Concluded)

\overline{Nu}	average Nusselt number
Nu_0	Nusselt number with vibration
Pr	Prandtl number
Q	heating rate
R	radius
Ra	Rayleigh number
Ra_c	critical Rayleigh number
Re	Reynolds number
s	significant dimension
t	time
T	temperature
V	velocity
α	thermal diffusivity
β	$\frac{1}{V} \left(\frac{dV}{dT} \right)_P$ coefficient of volume expansion
μ	absolute viscosity
ν	kinematic viscosity
Ω	dimensionless frequency
ρ	density
σ	surface tension
τ_c	period of vibration

APOLLO 17 HEAT FLOW AND CONVECTION EXPERIMENTS

FINAL DATA ANALYSES RESULTS

SUMMARY

A group of experiments called the Apollo 17 Heat Flow and Convection (HFC) Experiments was conducted by Astronaut Ron Evans on December 8, 1972, aboard the Apollo 17 spacecraft while in translunar coast on the way to the moon. Three experiments were conducted. In the Flow Pattern Experiment, cellular convection which developed as the result of heating an open pan of oil was observed. In the Radial Heating Experiment, a closed dish of argon gas was heated by means of a center post heater, and the resultant temperature changes were tracked by means of liquid crystals. The Flow Pattern and Radial Heating Experiments were improved test cells of experiments conducted by Astronaut Stuart Roosa aboard Apollo 14. The third Apollo 17 HFC Experiment called the Lineal Heating Experiment consisted of heating a cylinder of oil from one end. Fluid motion and temperature changes were tracked by means of suspended magnesium particles and liquid crystals, respectively. Observational and tracking data were recorded on motion picture film.

Results of data analyses show (references are given in the text):

Flow Pattern Experiment

- The sizes of the observed surface tension-driven convection cells agree fairly well with those predicted by linear analysis of surface tension-driven, cellular convection.
- Convection occurred at lower temperature gradients in low-g than in one-g. Surface tension and gravity, therefore, apparently do not reinforce each other in a manner predicted by one analysis of cellular convection.
- The Flow Pattern Experiment data substantiate in principle the postulate that gravity modulates cellular convection onset.

- The onset of a concentric side roll and center polygonal cells in the Flow Pattern Experiment occurred at about the same time. The occurrence of a roll is contrary to expectations based on latest literature. The observed onset pattern tends to confirm an earlier view that rolls are side wall effects and are not particularly characteristic of the driving mechanism.

Radial and Lineal Heating Experiments

- No significant convection was observed in the Radial or Lineal Heating Experiments. The data, however, validate the accuracy of the measuring technique and allow the conclusion that:

- The convection observed in the Apollo 14 Radial and Zone cells was probably caused by HFC unit and spacecraft vibrations.

I. INTRODUCTION

The exploitation of space for the benefit of mankind is rapidly evolving in several areas such as transcontinental TV communications, astronomy, weather satellites, earth resources, and space processing. Space processing [1-3] is being developed to exploit the unique environment of a space laboratory to research, develop, and finally manufacture products having improvements over those made on earth. Several examples have often been cited: better semiconductor crystals for use in solid-state electronic devices, purification of organic and biological materials for use in biochemistry and vaccines, development of new metal alloys, and better lens glass materials [4]. Fundamental to all these processes is the use of low-gravity to reduce unwanted fluid motions and settling of heavier materials while the product is being produced from the molten or gaseous state. Fluid mechanics (or convection) in space with varying boundary conditions of temperature, time, pressure, and artificial gravity levels, therefore, is a major concern. (The term convection is used herein in the sense of any perturbing force that can cause a contained fluid in low gravity to be nonstatic.)

One of the chief foreseen advantages of conducting manufacturing processes in space is the reduction in vigor of gravity-driven, natural convection. Gravity-driven, natural convection occurs spontaneously when certain conditions of container geometry, heating rates, solute concentration gradients, etc., are right. The result of convection is a stirring action which is deleterious to many processes because the stirring perturbs internal temperature and concentration gradients. The onset and vigor of gravity-driven, natural convection are very difficult to predict and, therefore, to control. In the low- or zero-g environments of orbiting spacecraft, gravity-driven convection will be much less of a problem. Gravity, however, is not the only driving force for fluid flow. A number of previous studies [5-7] have identified and discussed such nongravity forces as surface tension, interfacial tensions, thermal volumetric expansions, phase-change occasioned volume changes, electric and magnetic fields, rotation accelerations, and linear accelerations. Many of these nongravity types of convection often are not considered on earth because the gravity force is so much stronger and, thus, predominates. As a result, little is known about the nongravity forces. In low-g environments the nongravity forces will be of comparable magnitude to the low-g force. It is thus essential to know for control purposes the characteristics of convection caused by these nongravity forces and how they may couple with low gravity fields.

Convection studies in space are essential, therefore, to space processing, not to prove whether the various endeavors will work, but rather to establish the degree of suppression of thermal convection and to study previously masked forms of low-level convection. Such studies will provide criteria for future space processing activities.

To obtain information on the nature and magnitude of natural convection in low-g environments, two sets of experiments were conducted in the low-g environments encountered in space flight. The first set was conducted aboard the Apollo 14 flight by Astronaut Stewart Roosa on February 7, 1971. Results of the Apollo 14 Heat Flow and Convection Demonstration Experiments are given in References 8, 9, and 10. The Apollo 17 HFC Experiments were conducted on December 8, 1972, by Astronaut Ron Evans. A preliminary report of the results of the Apollo 17 HFC Experiments is given in Reference 11, and the present report presents the final results of an extensive data analyses study.

In the Apollo 14 HFC, three experimental tests were conducted. Cellular motion, which developed as the result of heating an open pan of oil, was observed in the Flow Pattern Experiment. Fine aluminum flakes suspended in the oil rendered the flow pattern visible. In the Radial Heating Experiment, a closed dish of carbon dioxide gas was heated by means of a center post heater, and the resultant temperature changes were tracked. The third test consisted of zone-heating cylindrical containers of pure water and 20-percent sugar solution and tracking the resultant temperature changes. Liquid crystal tapes which respond to temperature changes by changing color were the temperature detectors. The results of the experiments showed significant convection caused by nongravity motive forces. The Flow Pattern Experiment showed visible surface tension-driven cellular convection. The Radial Experiment showed two different kinds of low-g convection: a sustained mode, called first-order, and an oscillatory mode, called second-order. The magnitude of the first-order convective heat transfer was estimated (very approximately) to be on the order of from 10 to 30 percent above that of pure conduction and radiation prediction. The amount of first-order convective heat transfer observed in the two zone-heating experiments was lower, and it was therefore not meaningful to give a reliable estimate of its magnitude. Second-order convection was also noted in the zone-heating experiments.

In the Apollo 17 HFC, two of the experiments, the Flow Pattern Experiment and the Radial Heating Experiment, were repeated in cells of improved design. The Apollo 17 Radial Heating Experiment also utilized a different gas (argon). The third experiment, replacing the Apollo 14 Zone Heating

Experiment, was the Lineal Heating Experiment. In this latter experiment a cylinder of oil was heated from one end. Suspended magnesium particles and an internal grid of liquid crystals were the fluid flow and temperature sensors, respectively. The results of the Apollo 17 HFC Experiments were listed previously in the Summary.

In the following discussions the details of experiment construction, results, and interpretations are given. Implications of the results of the HFC experiments for space processing operations are also considered.

II. EXPERIMENTAL APPARATUS, CONDITIONS, AND PROCEDURES

The apparatus used in the Apollo 17 HFC Experiments is shown in Figure 1. A schematic identifying the various experiments is shown in Figure 2. More detailed drawings of the test cells are shown in Figure 3. Hardware, design, and operating details can be found in Reference 12. Table 1 summarizes the physical properties of the fluids involved, and Table 2 gives most of the flight boundary conditions at the time the experiments were performed. Data on the magnitude of the acceleration levels and the variation of the g-vector with time were obtained from magnetic tape gyroscope data. These data were analyzed via a computer program, and plots of each g-component versus time were obtained for a time interval (a meaningful visual scale was used) during the performance of the HFC Experiments. The data included not only the roll rate of the spacecraft but the variation of roll rate with time. The data, therefore, consist of oscillatory profiles of g versus time, taken at 2-sec intervals. A sample of this information is shown in Figures 4a through 4c. The g-level is seen to oscillate (g-jitter) about "zero" with an amplitude of about $10^{-7} g_e$ and with the frequency somewhat random. Careful examination reveals a mean magnitude of about $10^{-9} g_e$ during the HFC Experiments. (A preliminary analysis shows that the probable error of the g-calculations is approximately $1 \times 10^{-9} g_e$. The accuracy will be further detailed in a forthcoming report by Holland et al.) The same type of data for the Apollo 14 flight was taken at 30-sec intervals. An accurate determination of the variation in roll rate, therefore, was not possible and, as a result, the g-jitter is not as accurately defined as in the Apollo 17 case. The magnitude of the mean gravity level experienced during the Apollo 14 HFC was about the same as in the Apollo 17 flight; i. e., a mean magnitude of about $10^{-9} g_e$ with an occasional spike into the $10^{-5} g_e$ range [13]. Although a mean g-jitter level for the Apollo 14 case was indicated to be about $10^{-9} g_e$ by the data, this value is questionable because of the previously mentioned lack of knowledge concerning the roll rate variation. Additional evidence from tracking bubble movement in the Apollo 14 Zone Heating cell indicates that the vibration level at the location of the Apollo 14 HFC unit was of the order of 10^{-3} to $10^{-4} g_e$. (See Section IV. C. 3.)

As mentioned in the introduction, liquid crystal tapes were used as temperature sensors in the Radial and Lineal cells. Liquid crystal tapes were also used to obtain temperatures of the apparatus box and the ambient cabin temperature for each test. Liquid crystals are a class of organic compounds which have the property of selectively scattering light frequencies as a function of temperature. When applied in a thin layer to a black background,

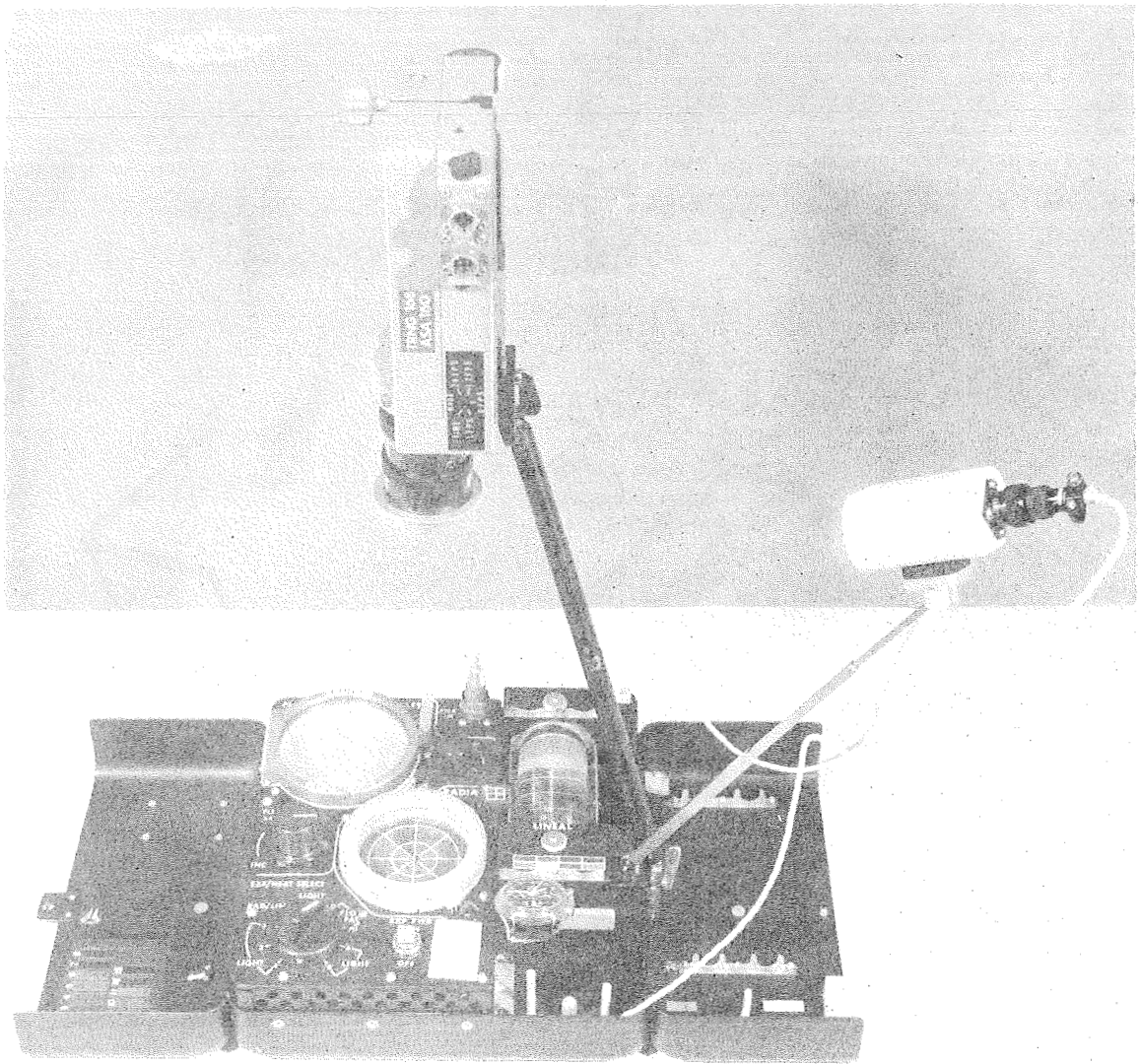


Figure 1. Apparatus configuration for the Heat Flow and Convection Demonstration for Apollo 17.

these liquid crystals are transparent below their response range so that an observer sees the black background. As the temperature increases, light is scattered so that an observer sees various colors in the order of amber to green to blue. Amber corresponds to the lower temperature and blue to the higher temperature. Liquid crystals which have been made into tapes are available commercially. These tapes consist of a thin, black Mylar sheet

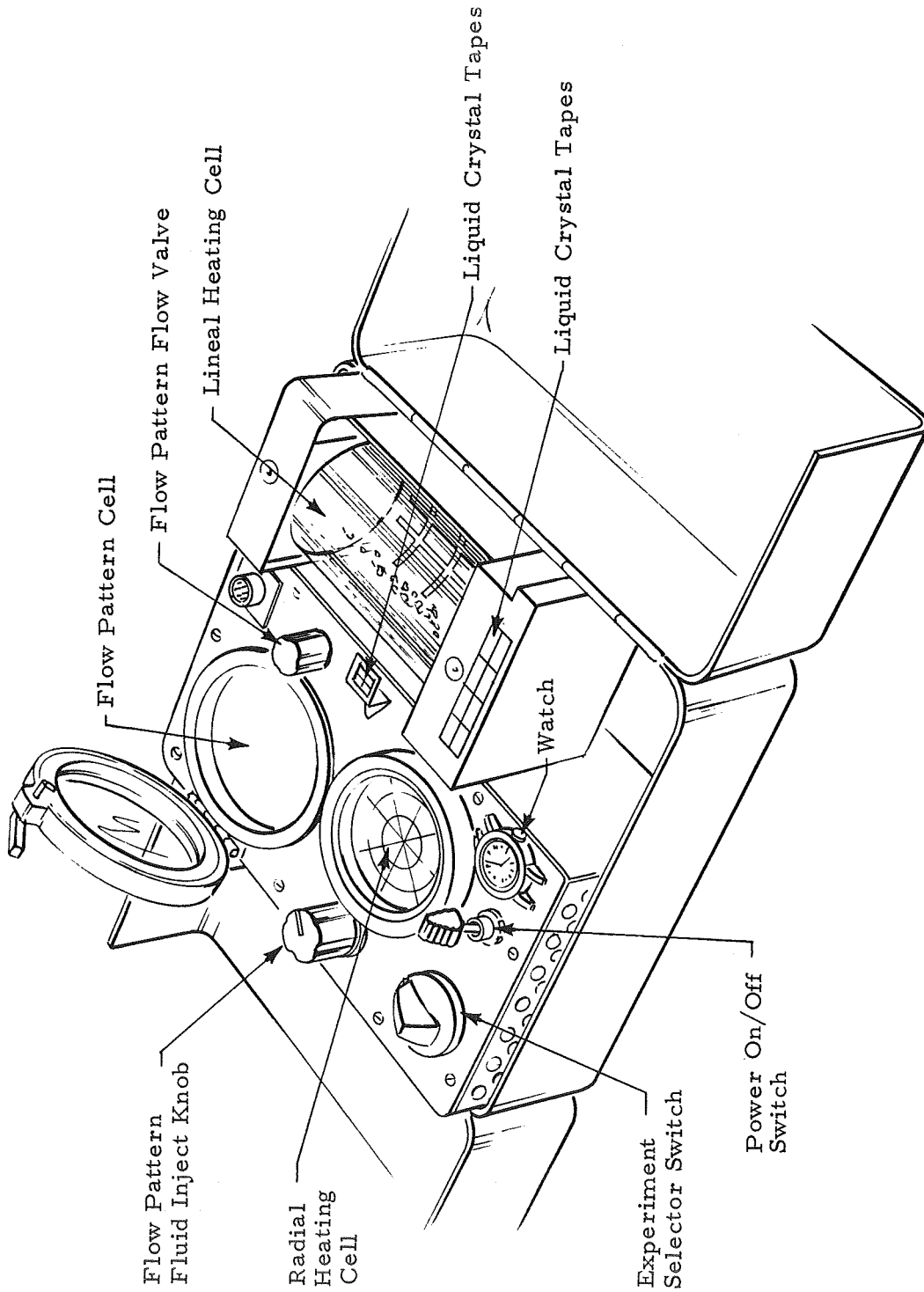
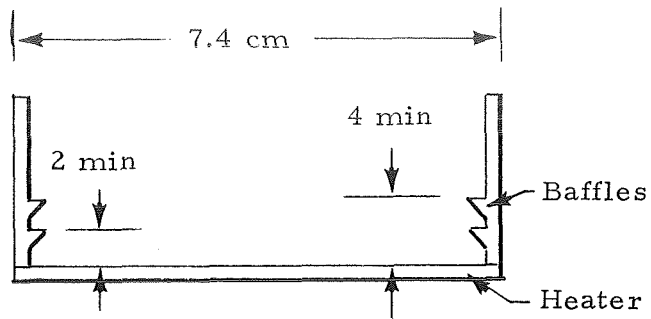
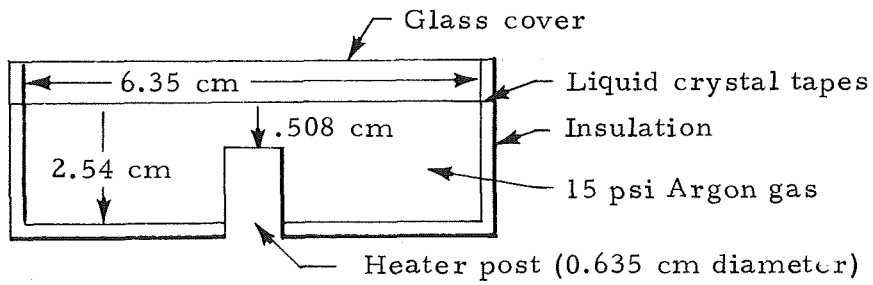


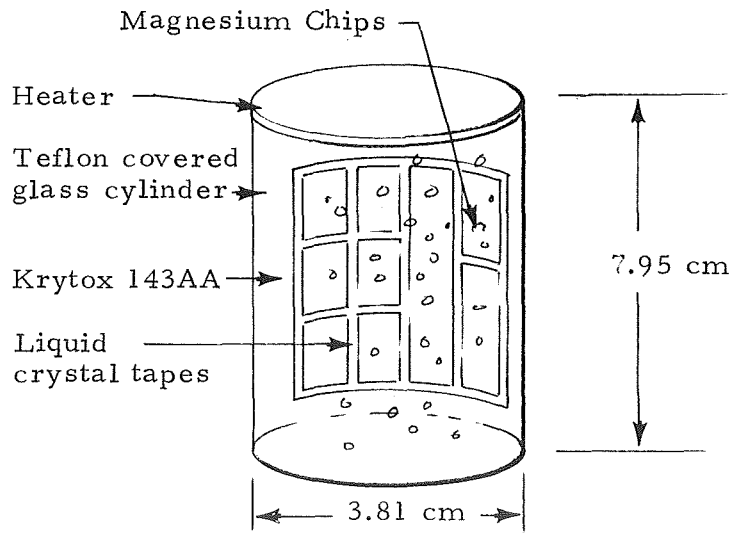
Figure 2. Panel face of Apollo 17 Heat Flow and Convection apparatus.



a. Flow Pattern Cell Diagram (Side Cutaway)



b. Radial Heating Cell Diagram (Side Cutaway)



c. Lineal Unit Diagram

Figure 3. Details of the Apollo 17 Heat Flow and Convection Experiments.

TABLE 1. PHYSICAL PROPERTIES OF APOLLO 17 AND 14 FLUIDS

Fluid	T, °C	ρ , gm/cm ³	μ , poise	ν , cm ² /sec	k, cal/cm/ sec °C	α , cm ² /sec	β , °C ⁻¹	C _p , cal/gm/ °C	Pr
Argon	0	1.78×10^{-3}	2.1×10^{-4}	0.118	3.76×10^{-5}	0.176	3.70×10^{-3}	0.12	0.955
	149	1.64×10^{-3}	2.9×10^{-4}	0.177	5.57×10^{-5}	0.262	3.70×10^{-3}	0.13	0.68
Carbon Dioxide	65.5	1.6×10^{-3}	1.70×10^{-4}	0.106	4.63×10^{-5}	0.140	3.72×10^{-3}	0.210	0.76
	149	1.31×10^{-3}	2.04×10^{-4}	0.155	6.16×10^{-5}	0.216	3.72×10^{-3}	0.230	0.72
Krytox 143AA ^a	65.5	1.85	0.666	0.36	2.02×10^{-4}	0.45×10^{-3}	1.045×10^{-3}	0.243	800
	93.3	1.74	9.38×10^{-2}	0.054	1.96×10^{-4}	0.437×10^{-3}	1.045×10^{-3}	0.259	123
Water	37.8	0.992	6.83×10^{-3}	6.88×10^{-3}	1.50×10^{-3}	1.52×10^{-3}	2.07×10^{-4}	0.998	4.53
	65.5	0.98	4.35×10^{-3}	4.43×10^{-3}	1.59×10^{-3}	1.62×10^{-3}	2.07×10^{-4}	1.000	2.74
Krytox 143AZ ^{a, b}	37.8	1.83	0.329	0.18			1.1×10^{-3}		

a. Krytox 143AZ and 143AA are DuPont trade names for a series of perfluoroalkylpolyester oils. These oils were chosen because they met flight safety requirements.

b. The actual fluid used in the Apollo 14 and 17 Flow Pattern Experiments consisted of the following mixture: Krytox 143AZ plus 0.15 percent by weight fine aluminum powder (Alcoa grade 422) and 1/600 by volume Krytox 157 (a surfactant to keep the aluminum particles suspended).

Notes: T — temperature
 ρ — density
 μ — coefficient of viscosity
 ν — kinematic viscosity
k — thermal conductivity

α — thermal diffusivity
 β — volumetric expansion coefficient
C_p — specific heat
Pr — Prandtl number ($= \frac{\nu}{\alpha}$)

TABLE 2. APOLLO 17 HFC DEMONSTRATION EXPERIMENT —
FLIGHT BOUNDARY CONDITIONS

Event	WT ^a (hr:min:sec)	GET ^b (hr:min:sec)	Frame No. of Motion Picture Data	Heating Rates	Line Voltage, Vdc	Cabin Temperature, °C	Cabin Pressure, psi
Watch Set	18:30:01	42:56:52			29.0 ± 0.4	17.8	4.8
First Tests							
• Radial/Lineal							
On	6:34:01	43:00:52	58	Radial — 5 W	29.0 ± 0.4		
Off	6:44:05	43:10:56		Lineal — 18 W			
• Begin Pumping Krytox	6:49:20	43:16:11					
• End Pumping Krytox	6:53:00	43:19:51					
• Flow Pattern (2-mm nominal depth)							
On	7:04:05	43:30:56		7.5 W	28.8 ± 0.4		
Off	7:19:09	43:46:00					
Watch Reset	9:04:00	45:30:38				18.3 to 20	
Second Tests							
• Radial/Lineal							
On	9:05:05	45:31:38	3044	Radial — 5 W	28.7 ± 0.4		
Off	9:15:04	45:41:42		Lineal — 18 W			
• Flow Pattern (4-mm nominal depth)							
On	9:37:48	46:04:26		5 W			
Off	9:53:25	46:20:03					

a. Watch time.
b. Ground elapsed time.

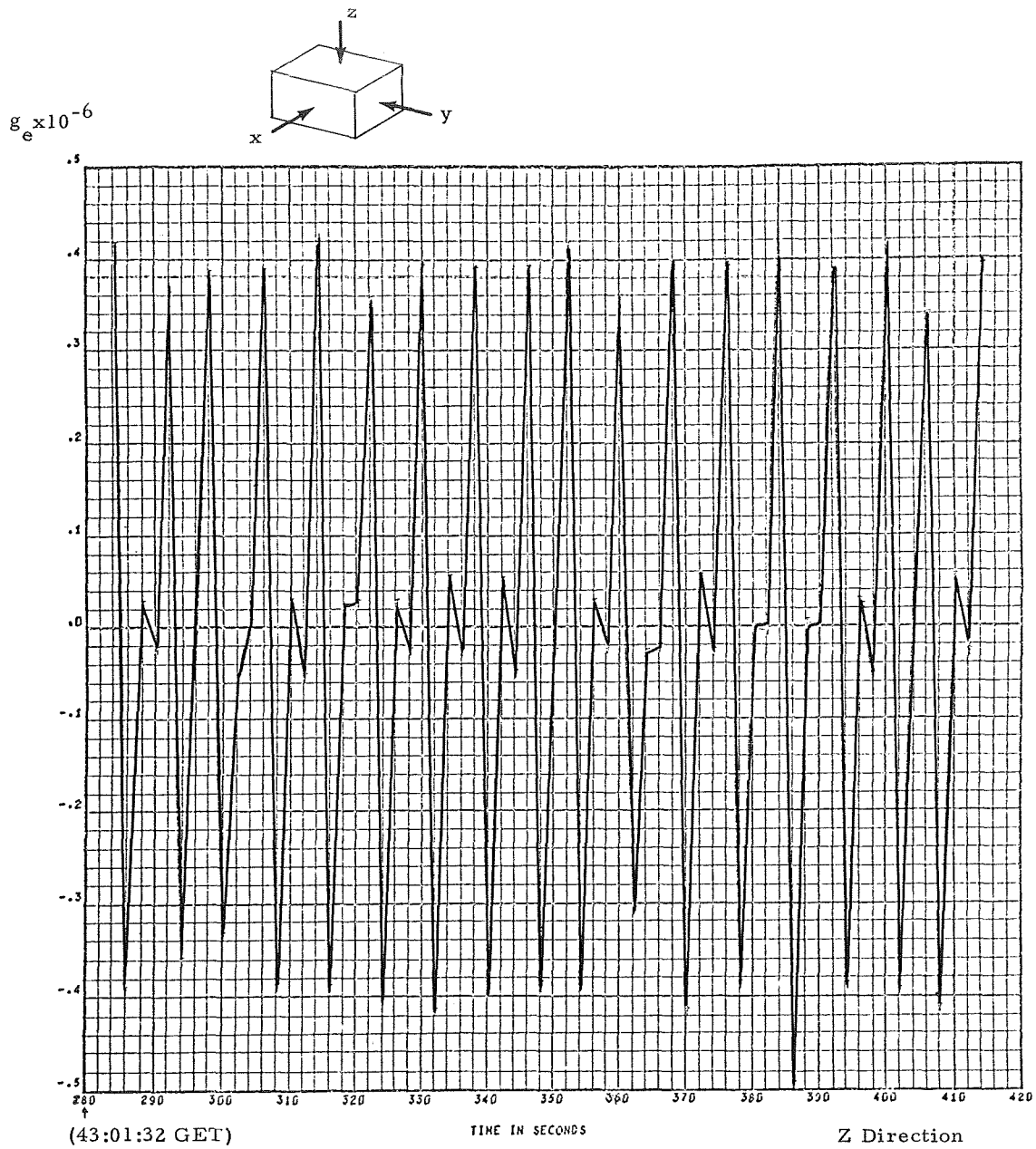


Figure 4a. Gravity level in z direction of the HFC apparatus.

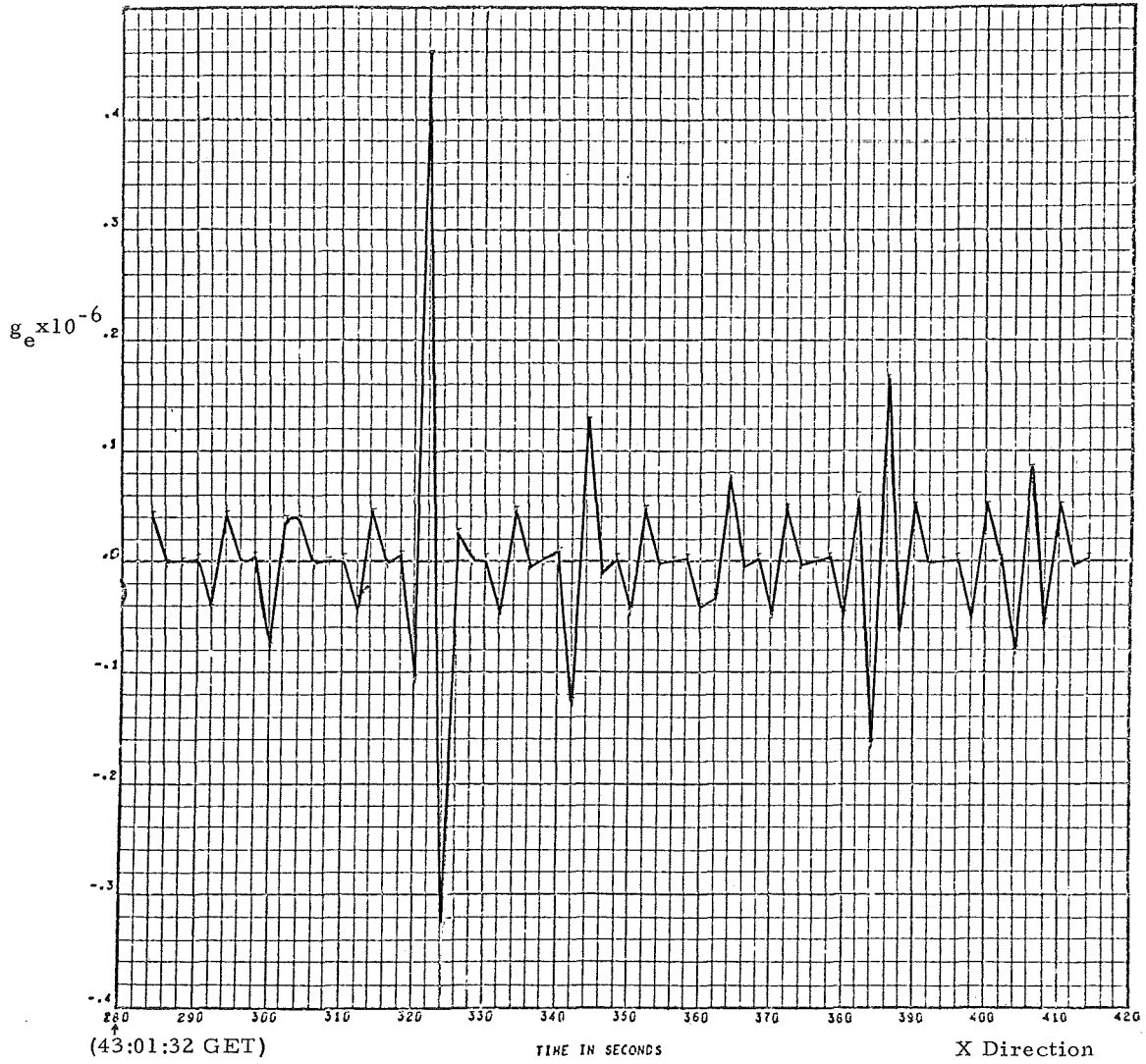
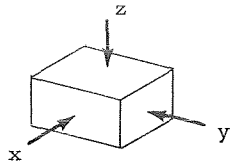


Figure 4b. Gravity level in x direction of the HFC apparatus.

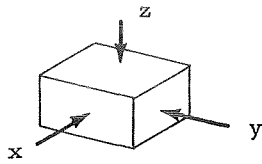


Figure 4c. Gravity level in y direction of the HFC apparatus.

coated with liquid crystal material and covered with clear plastic. An adhesive is coated on the back of these tapes so that they can easily be applied to a surface for temperature measurement. By varying the composition of the compounds used in the tapes, different temperature response ranges can be achieved. The temperature response of the tapes is unaffected by small pressure variations and low-g environments (see Appendix A).

Each identifiable color actually represents a segment of the total response range of the crystal. For instance, if a liquid crystal tape has a range of 30 to 36° C, then amber might represent 30 to 33° C, green 33 to 35° C, blue 35 to 36° C, and black 35 to 36° C. By using the leading edge of a color band as a reference point, temperatures can be determined with a good degree of precision. This is illustrated in Figure 5.

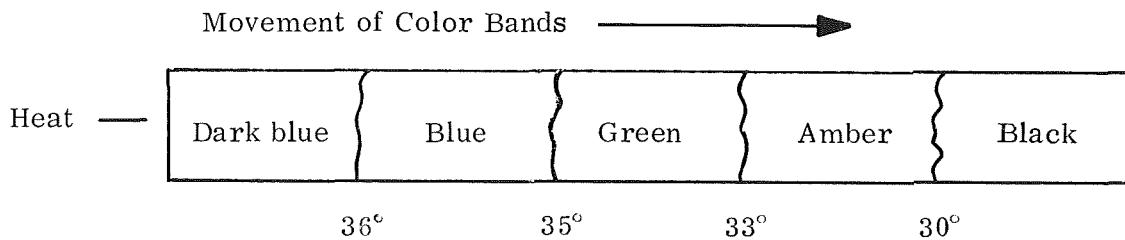


Figure 5. Illustration of color bands in a liquid crystal tape.

The liquid crystal tapes used on the Apollo HFC were obtained from Hoffmann LaRoche Company. The crystal tape designation and the manufacturer's nominal temperature ranges are shown in the following table. Figure 6 shows the locations of these tapes on the HFC unit, and Table 3 gives precise calibrated temperature values.

Crystal Designation	A	B	C	D	E	F	G	H	I	J	K
Nominal Temperature Range, °C	16.5-21.5	21.0-28.0	23.0-25.75	24.0-30.0	27.0-36.25	29.5-35.0	32.0-37.75	34.8-44.0	35.0-46.5	40-46.5	20.0-23.0

Data from the experiment were in the form of a 16-mm film taken at 1 frame/sec. From this film, color position versus time could be obtained for each crystal in the cells. Also the initial colors of each crystal at the

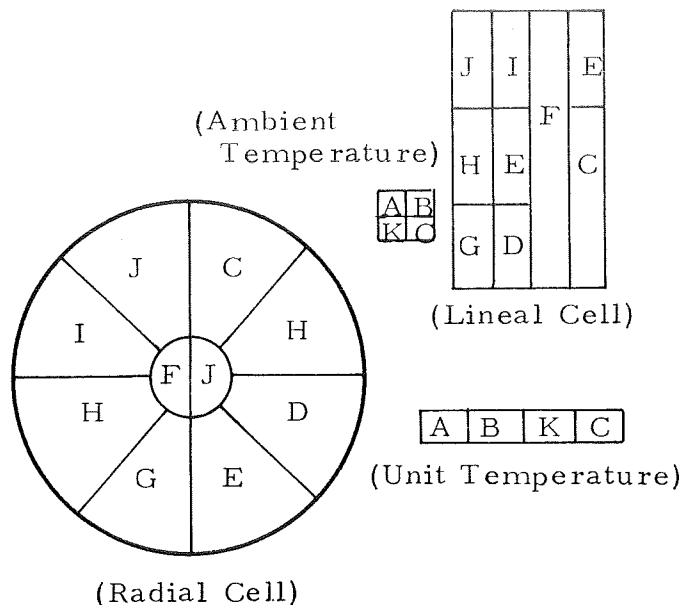


Figure 6. Location of liquid crystals on Apollo 17 HFC.

beginning of each run were determined, thus giving initial and ambient temperatures within the test cells.

The theory of utilizing liquid crystal tapes to determine the temperature of a surface was considered in the Apollo 14 HFC research and development work. Both isothermal (the case of a surface which is slowly heated or cooled over its entire area) and dynamic (the case of a surface being heated or cooled such that a temperature gradient exists in the surface) studies were made [9], and a technique for calibrating liquid crystal tapes for the application of mapping convective heat transfer was developed. In the present study, more extensive calibration studies were conducted. The details of these studies are given in Appendix A. Table 3 presents both the isothermal and dynamic temperature values for the Apollo 17 liquid crystal tapes obtained in the calibration studies. The accuracy of the calculated theoretical curves set the accuracy requirement of the liquid crystal tapes approximately at $\pm 1^\circ\text{C}$. Assuming the precision error reflects the accuracy error of the liquid crystal tapes, it can be seen from Table 3 that the accuracy of the liquid crystal tapes falls well within the required limit.

A number of ground tests were conducted to ascertain the error associated with liquid level height in the Flow Pattern Experiment. The procedure followed to determine the error consisted of measuring the height of the liquid

TABLE 3. VALUES OF LIQUID CRYSTAL DYNAMIC AND ISOTHERMAL TEMPERATURES

Dynamic Temperatures

Tape and Color	°C	Precision (rms)	Tape and Color	°C	Precision (rms)
Tape D			Tape H		
Amber	24.7	±0.2	Amber	36.3	±0.3
Green	26.5	±0.3	Green	37.4	±0.4
Blue	28.8	±0.6	Blue	39.0	±0.7
Tape E			Tape I		
Amber	26.9	±0.8	Amber	35.7	±0.2
Green	28.6	±0.5	Green	37.8	±0.2
Blue	30.7	±0.6	Blue	41.0	±0.4
Tape F			Tape J		
Amber	30.0	±0.4	Amber	42.6	±0.4
Green	31.8	±0.5	Green	44.7	±0.4
Blue	34.5	±0.8	Blue	47.3	±0.9
Tape G					
Amber	32.0	±0.9			
Green	33.5	±0.6			
Blue	35.1	±0.8			

Isothermal Temperatures

Tape Color	C		D		E	
	Value	Precision (rms)	Value	Precision (rms)	Value	Precision (rms)
Brown	22.9	±0.4	24.6	±0.3	27.0	±0.5
Amber	23.4	±0.2	25.5	±0.4	27.5	±0.6
Yellow Green	23.8	±0.2	26.2	±0.2	28.1	±0.4
Green	24.2	±0.3	26.8	±0.3	28.7	±0.5
Blue Green	24.6	±0.2	28.2	±0.6	29.5	±0.5
Dark Blue Green	25.0	±0.2	28.7	±0.5	30.1	±0.6
Blue	25.4	±0.2	29.6	±0.4	30.7	±0.7
Dark Blue	25.8	±0.3	30.5	±0.6	31.4	±0.8

introduced into the Flow Pattern pan with a microheight gauge to which a needle was attached. The needle gauge facilitated locating the free liquid surface. Liquid was introduced into the Flow Pattern cell according to directions given in the Operating Procedures document [12]. These directions are: Rotate FLUID INJECT CW evenly and slowly until liquid is just sighted entering the pan. Slowly continue rotation exactly four revolutions CW. The HFC apparatus was designed so that four revolutions CW would result in a nominal liquid layer depth of 2 mm. The measurement obtained by four different observers is shown in Table 4.

TABLE 4. MEASURED LIQUID LEVELS
IN FLOW PATTERN CELL

2-mm Level		4-mm Level	
Height	Observer	Height	Observer
1.89	1	3.73	2
1.81	1	3.76	2
1.94	1	3.58	1
1.95	2	3.64	1
1.88	2	3.80	3
2.00	3	3.67	4
1.96	4	3.79	1
1.83	1	3.83	1
<u>2.06</u>	1	—	
1.89 (Avg)		3.73 (Avg)	
Root Mean Square Error: ± 0.11		Root Mean Square Error: ± 0.09	

The Radial and Lineal Heating Experiments were run concurrently. The astronaut, after light setup and camera start, simply turned the operations switch to start the heat. Heating continued for 10 min during which time

the color changes on the liquid crystal tapes and any magnesium particle movements in the Lineal cell were photographed by the motion picture camera. Photography of the color changes on cooldown continued for 2 min after the heat was stopped.

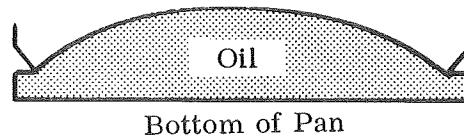
Upon completion of the Radial-Lineal run, the cover on the Flow Pattern unit was opened. The flow valve was then opened and the fluid inject knob was turned slowly four complete revolutions. Four turns of the knob allowed sufficient Krytox oil to flow into the pan to give a 2-mm deep layer of oil over the bottom of the pan. The bottom of the pan was constructed of aluminum which is wet by the oil. Spreading of the oil when first injected into the pan in zero-g was caused by adhesion forces. The oil layer was constrained to maintain an approximately flat surface in zero-g by small side baffles (Fig. 2). After the oil was injected, a waiting period of 2 min was allowed to permit fluid motion introduced by pumping to damp out. After this period, the heat was turned on and subsequent motions were recorded on film. The experiment ran 15 min. A total of 2 min of cooldown time was also photographed.

The complete sequence of experiments was repeated at a later time. The only difference between the two sequences was that a layer 4 mm deep rather than 2 mm deep was heated in the Flow Pattern Experiment.

III. FLIGHT RESULTS

A. Flow Pattern Experiment

Cellular convection was observed in both the 2-mm and 4-mm deep layers. Before the photographs of these figures are contemplated, however, it is well to keep in mind that the layers of fluid in which the convection developed were not perfectly flat. In filling the pan prior to the performance of the flight test, it was discovered that sizeable air bubbles somehow had been introduced into the test fluid. The cause of the bubbles is not known. No trouble with sizeable air bubbles had been encountered in the Apollo 14 HFC test. Because of the bubbles the designated number of turns of the fluid inject knob failed to completely cover the bottom of the pan. Astronaut Ron Evans, after conferring with the Principal Investigators on the ground, then injected more fluid until the bottom of the pan was completely covered.¹ In doing so, he probably injected more fluid than the baffle could constrain to a reasonably flat surface. Astronaut Evans reported that the layer of heated oil was convex in shape as shown in the sketch below. He estimated that the thickness in the center was twice the baffle height.



Some difficulties resulted in a convex shaped layer in the 4-mm case also. Exact fluid depths in the Flow Pattern tests are, therefore, not known.

1. While discussing the bubble problems with the Principle Investigators on the ground, two methods of circumventing the difficulty were conceived and attempted. Prior to the 2-mm run, Astronaut Evans attempted to puncture the bubbles with his pen. The bubbles moved to one side or the other, resulting in no bubbles being eliminated. The second method was attempted between the 2-mm and 4-mm runs. In this approach, the fluid was pumped back into the reservoir and the bubbles tended to remain in the dish. Astronaut Evans wiped the dish clean at a point when about 80 percent of the fluid had been returned. Thus, only a few bubbles remained in the 4-mm run and are believed by the authors to be the origin of the two regions of smaller Bénard cells in the 4-mm run. Apollo 14 Astronaut Stuart Roosa was in the control room during this time period on Apollo 17 and proved to be an invaluable asset in running this experiment.

Figures 7 and 8 show the types of convective cells observed in the Apollo 17 Flow Pattern Experiment. Figures 9 and 10 show the types of cells obtained in ground tests. For comparison the type of convection cell obtained in the Apollo 14 HFC Flow Pattern Experiment is shown in Figure 11.

The time intervals between when the heat was first turned on and when convection was first noted are tabulated in Table 5.

Conduction temperature profiles at the time of convection onset were calculated by means of a computer for various cases. (See Appendix B for details of the modeling.) Figures 12 through 15 are typical of the types of temperature profiles obtained. It can be seen that the temperature profiles are somewhat curved (nonlinear) instead of being straight lines (linear). From these curves it is possible to determine an overall temperature drop through the layers; i. e. ,

$$\Delta T = T_{\text{surface}} - T_{\text{heated wall}} \quad .$$

Knowing the ΔT then enables calculation of appropriate dimensionless numbers. (See Appendix B for definitions and discussions of various dimensionless numbers used in the present study.) The relevant numbers of interest here are the Marangoni number, Ma , and the Rayleigh number, Ra . These numbers for the various cases of interest are given in Table 6 (for a flight nominal gravity level of $10^{-9} g_e$).

Average cell sizes were obtained by determining from a photograph, with a planometer, the area of each cell. The areas were then averaged and an average diameter was determined from the average area, assuming the cells were circular in shape. The areas and cell diameters determined in this way are given in Table 7.

The manner in which cellular convection developed is summarized in Table 8. The data presented indicate that the side baffles for retaining the 2-mm oil layer did not exert any appreciable effect on the observed convection in the 4-mm layer.

The presence of bubbles in the test fluid apparently influenced the manner in which cellular convection began. Although it was not evident from the film record, Astronaut Evans reported that in the 2-mm case each bubble looked like the locus or the start of a cell. In the 4-mm case, only a few bubbles were visible and these did not seem to exert any appreciable influence



Figure 7. Convection cells obtained in 2-mm deep oil during Apollo 17 flight (14 min 19 sec after convection onset, 7.5-W heating rate).

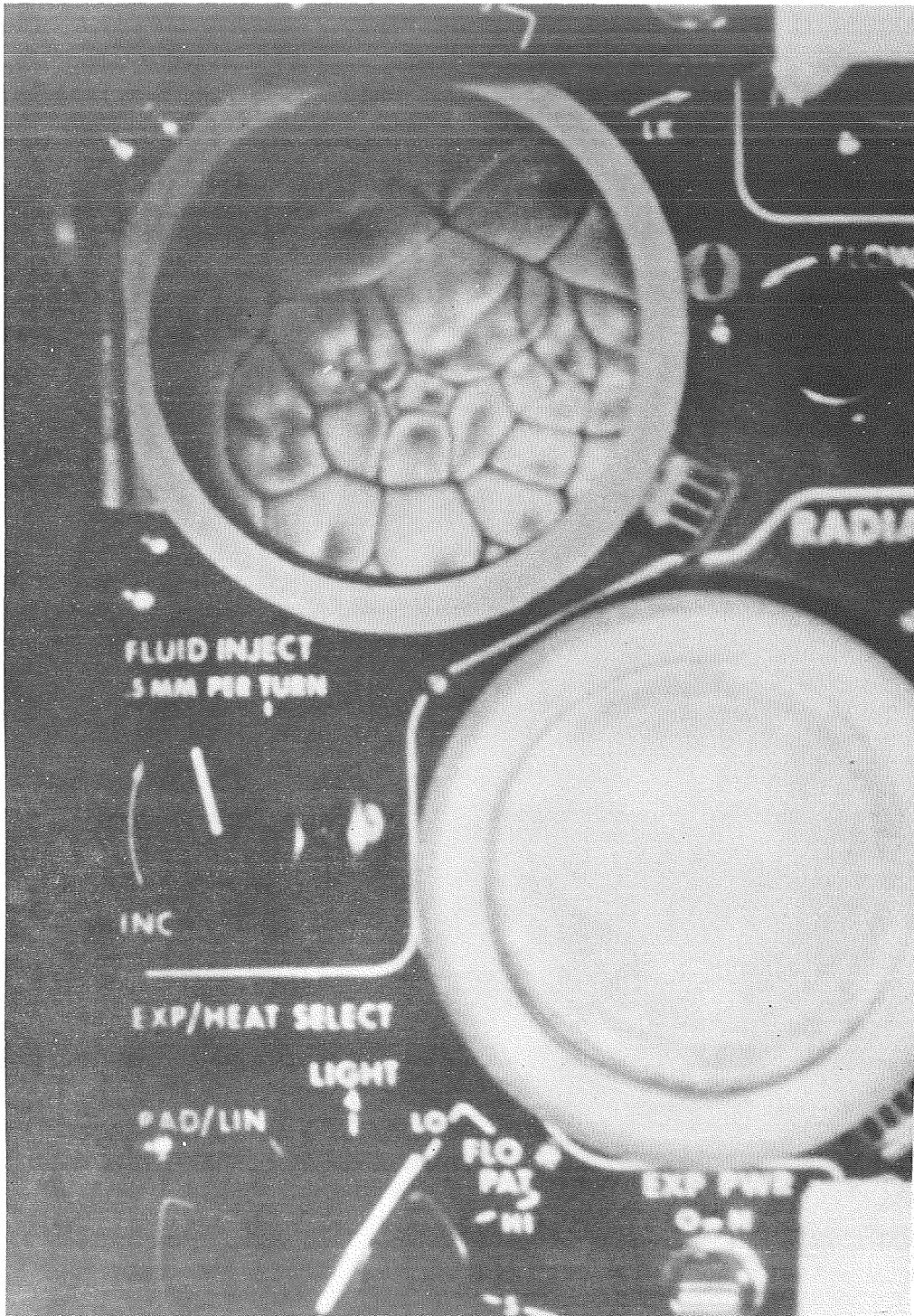


Figure 8. Convection cells obtained in 4-mm deep oil during Apollo 17 flight (10 min 55 sec after convection onset, 5-W heating rate).

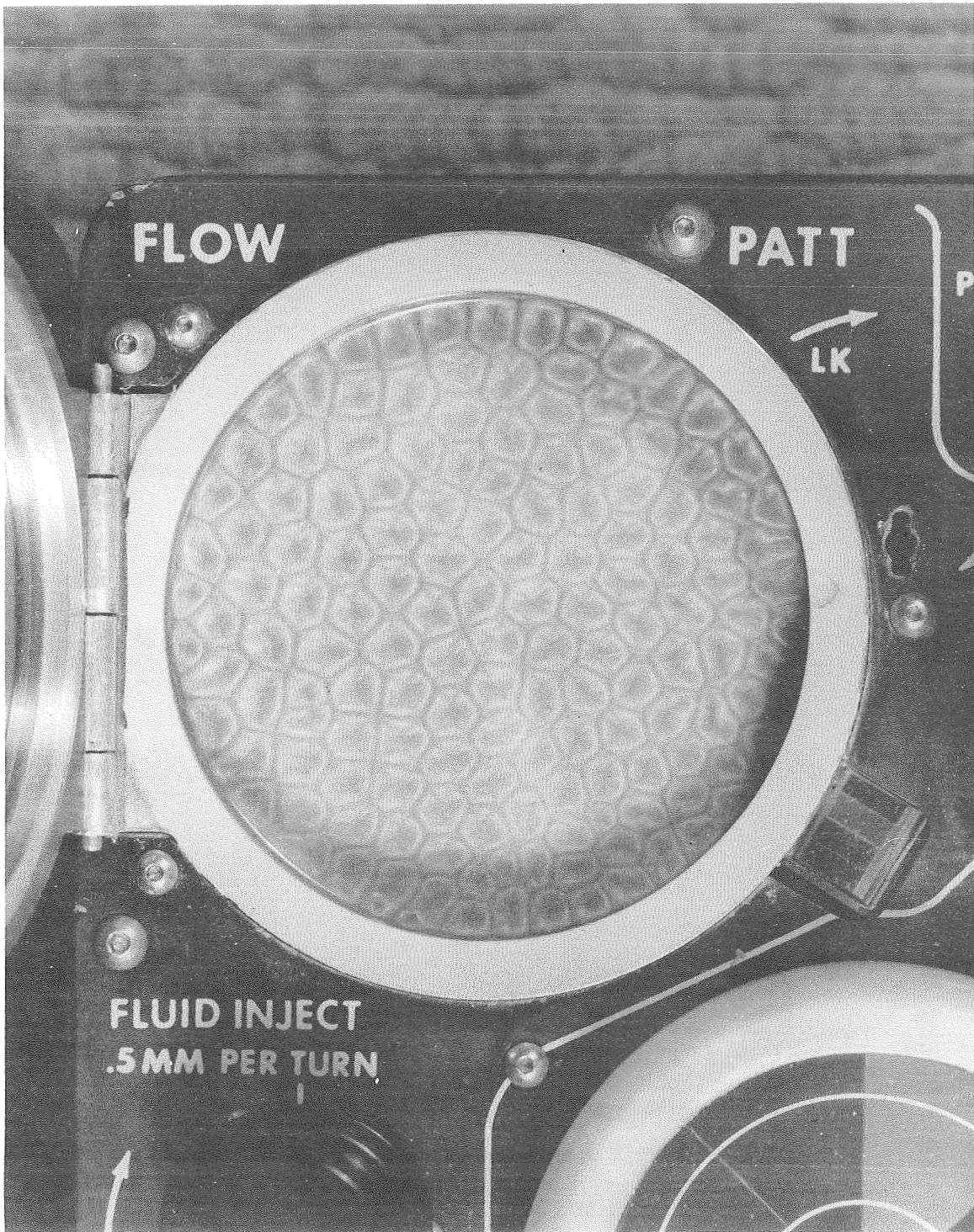


Figure 9. Convection cells obtained in 2-mm deep oil in ground test
(14 min 20 sec after convection onset,
7.5-W heating rate).

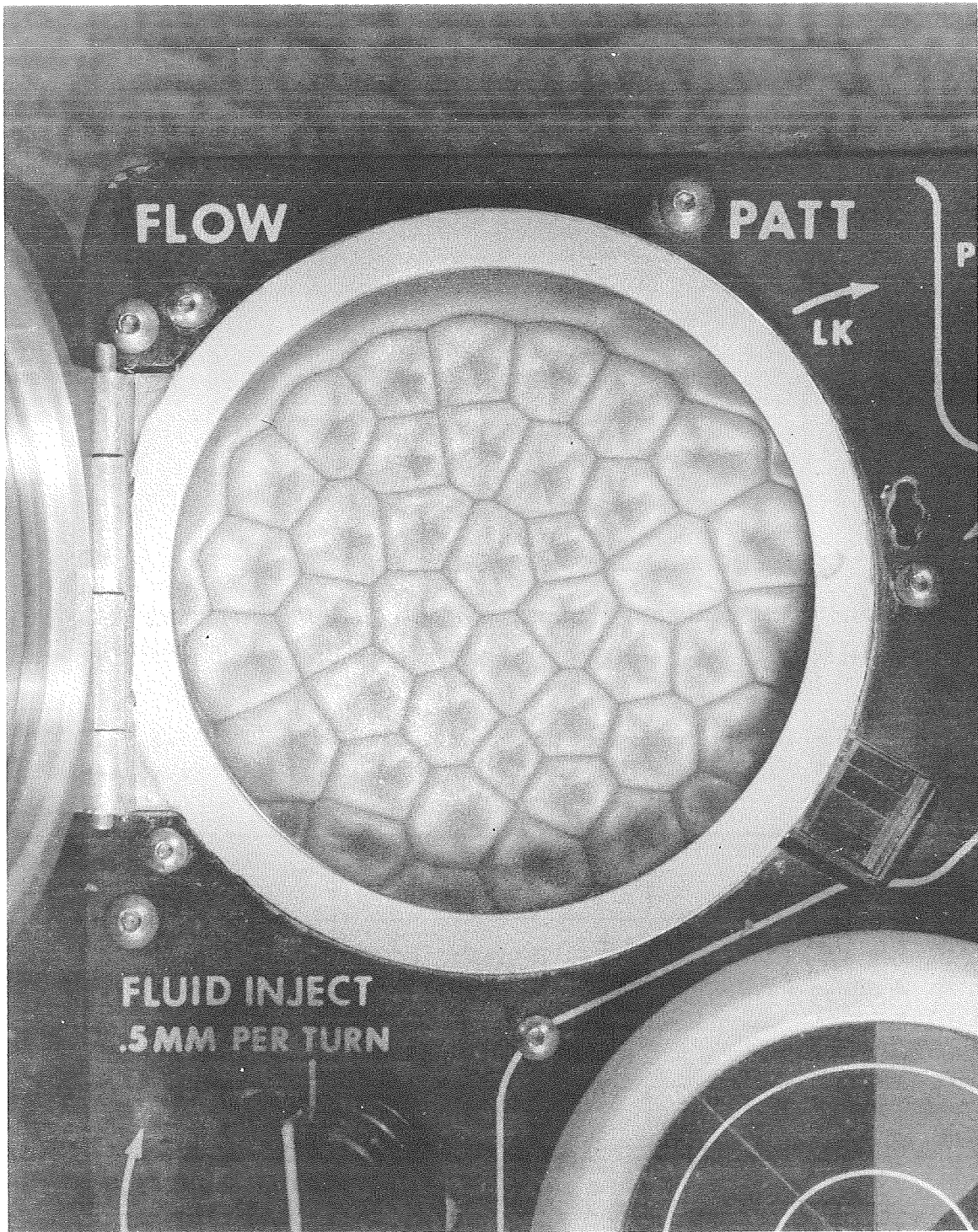


Figure 10. Convection cells obtained in 4-mm deep oil in ground test (10 min 43 sec after convection onset, 5-W heating rate).

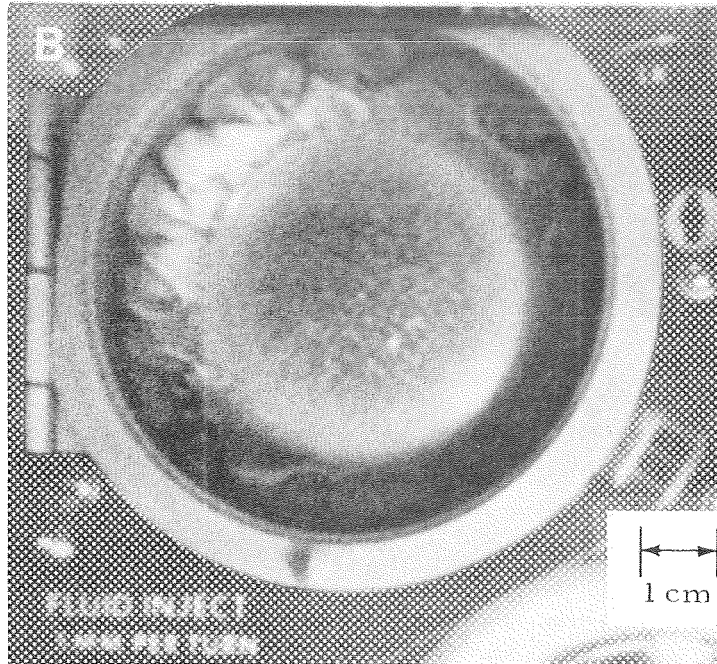


Figure 11. Convection cells obtained in Apollo 14 HFC Experiment (7.4-W heating rate, liquid volume sufficient to give 2-mm layer on ground).

TABLE 5. FLOW PATTERN CONVECTION ONSET TIMES FOR APOLLO 17 AND GROUND CASES

Apollo 17	Convection Onset Times	Heating Rate, W
Nominal 2 mm	18-21 sec	7.5
Nominal 4 mm	48-60 sec	5.0
Ground Tests		
0.986 mm	9.5 min	7.5
0.998 mm	7.5 min	7.5
1.25 mm	3 min	7.5
1.78 mm	3.5 min	7.5
1.84 mm	2 min	7.5
1.94 mm	1.75 min	7.5
1.97 mm	2 min	7.5
2.84 mm	2.5 min	5.0
3.96 mm	2 min	5.0

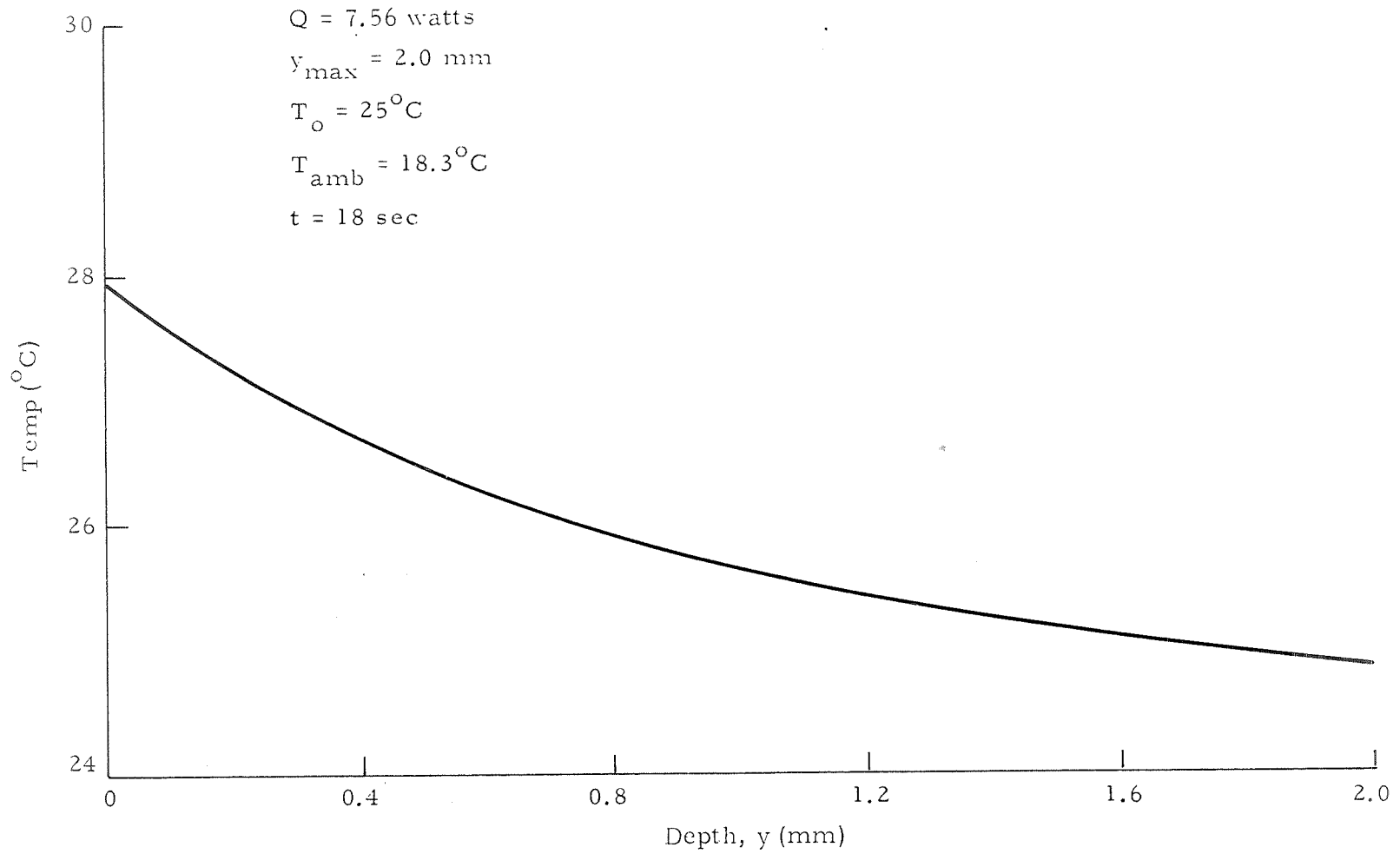


Figure 12. Computed thermal profile through 2-mm Krytox layer
18 sec after application of heat.

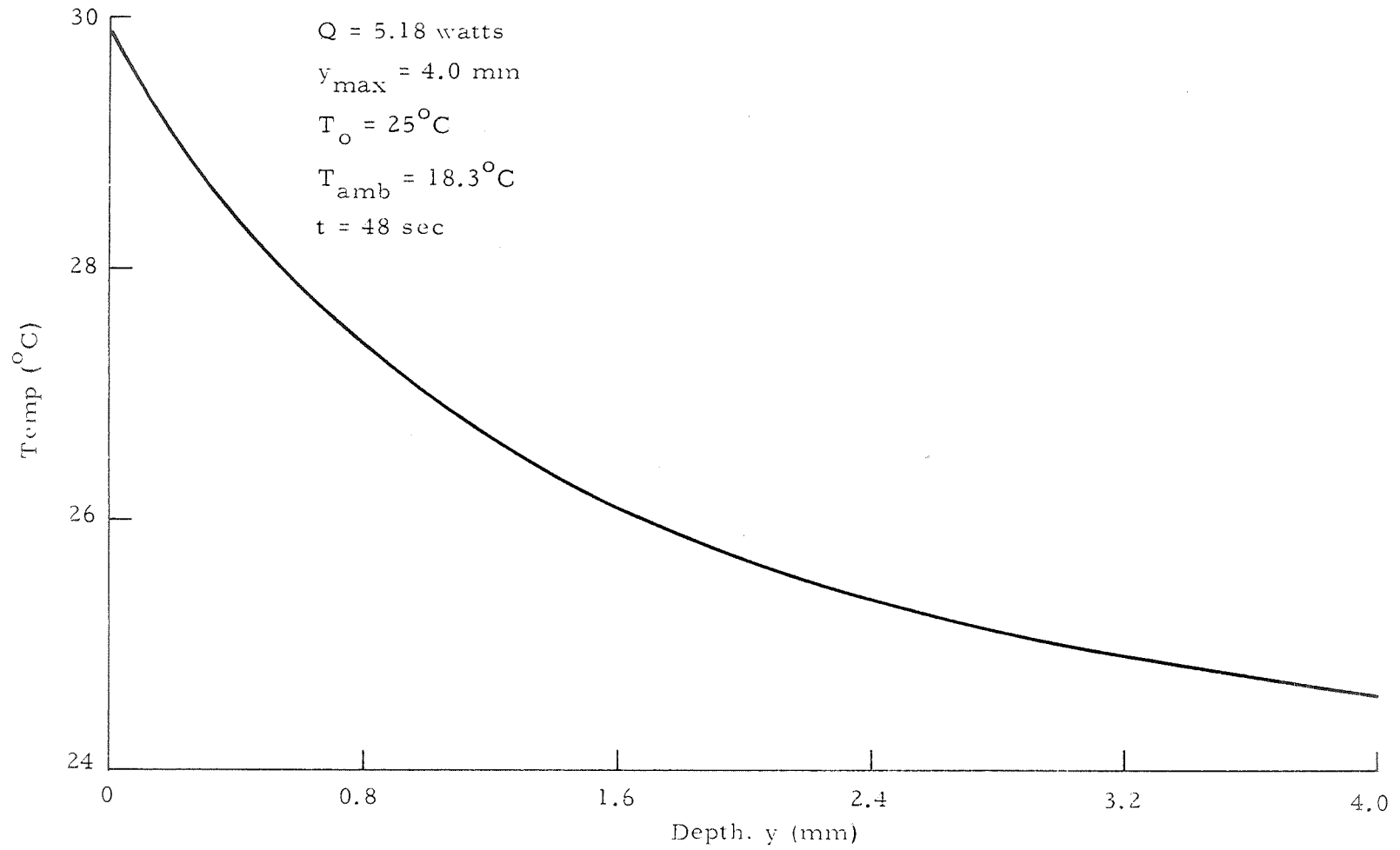


Figure 13. Computed thermal profile through 4-mm Krytox layer
48 sec after application of heat.

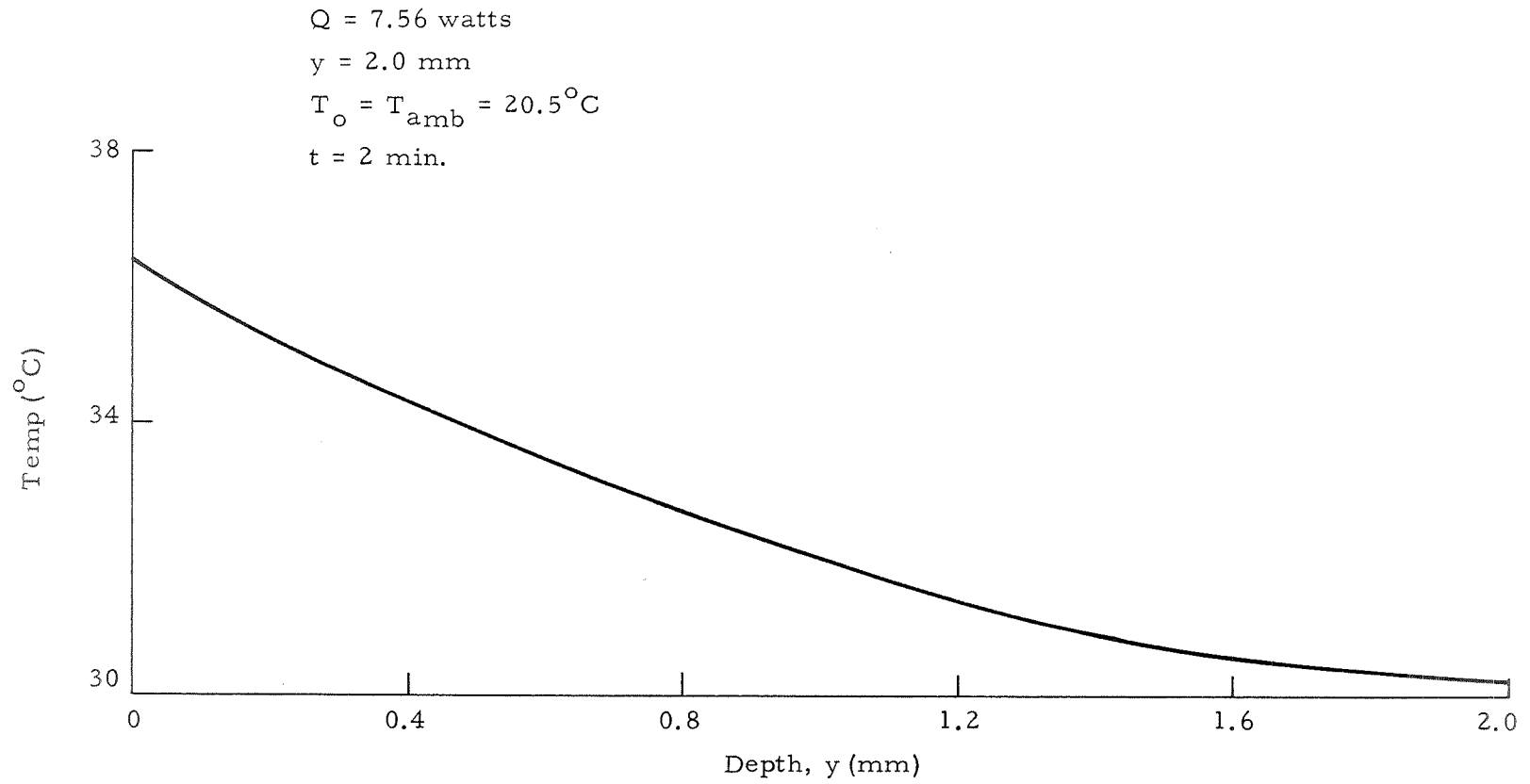


Figure 14. Computed thermal profile through 2-mm Krytox layer
2 min after application of heat.

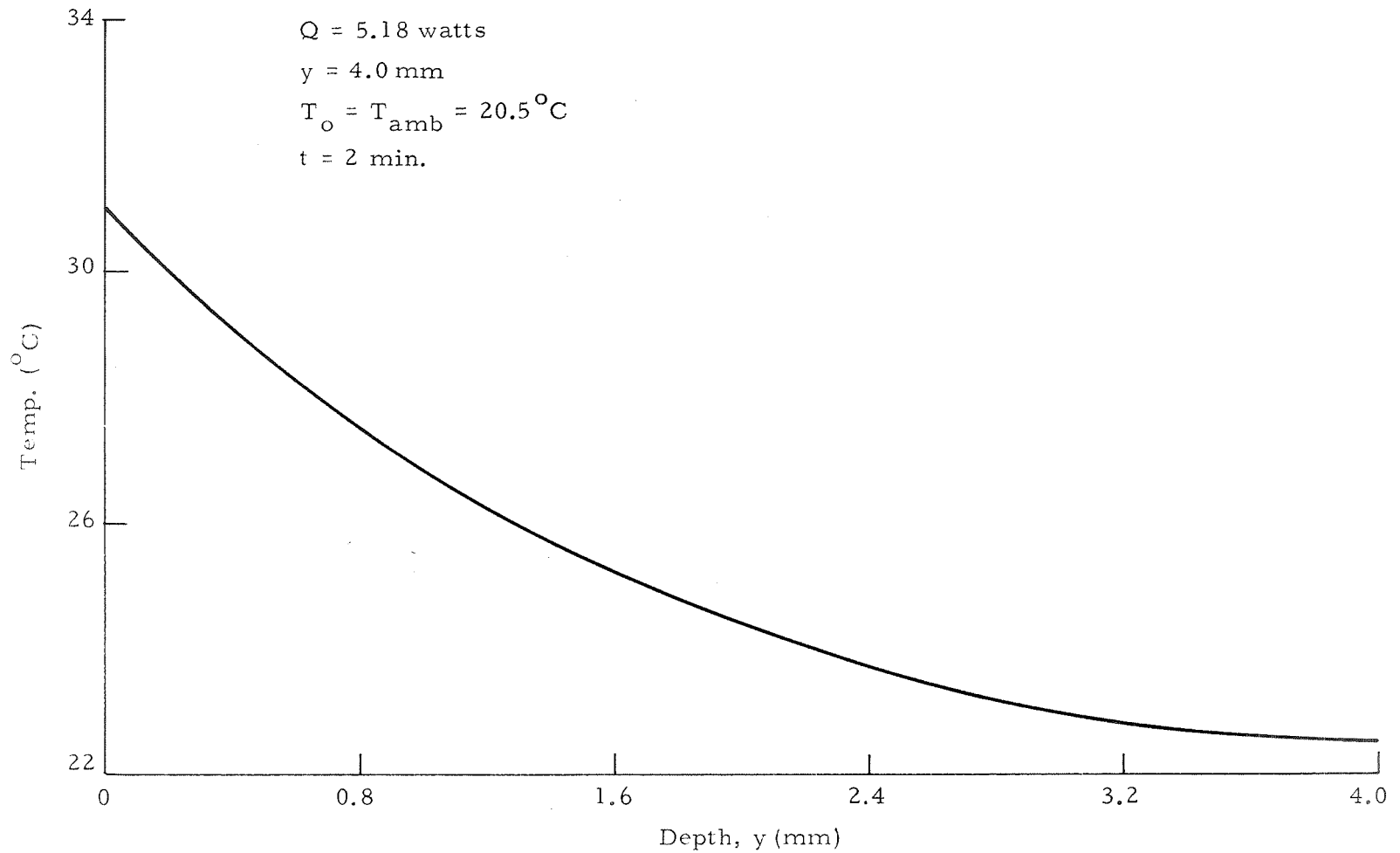


Figure 15. Computed thermal profile through 4-mm Krytox layer
2 min after application of heat.

TABLE 6. MARANGONI AND RAYLEIGH NUMBERS
AT FLOW PATTERN CONVECTION ONSET

	Ma	Ra
Apollo 17		
2-mm Case	400	3×10^{-7}
4-mm Case	1320	4×10^{-6}
Ground Test		
2-mm Case	927	695
4-mm Case	2580	7710

TABLE 7. APOLLO 17 CONVECTION CELL
AREAS AND DIAMETERS

	Average Area, cm ²	Average Deviation, cm ²	Average Diameter, cm	Average Deviation, cm
Apollo 17	0.4	±0.2	0.7	±0.2
2-mm Case	1.5	±0.8	1.4	±0.4
4-mm Case				
Ground Test				
2-mm Case	0.5	±0.1	0.8	±0.1
4-mm Case	1.5	±0.2	1.4	±0.1

upon the observed convection. However, Astronaut Evans reported that when upon completion of the test he pumped oil out of the pan he noticed two bubbles attached to the surface of the pan.

In view of these observations concerning bubbles, a ground test was conducted in which a pan of fluid, of the same composition as used in the flight test, was put in a vacuum chamber. The chamber was evacuated and pumping was continued until no evidence of dissolved air remained. The fluid was then heated from below. No differences in convection onset times or manner of convection onset, as compared to aerated fluid, were noted. It may, thus, be concluded that although the bubbles influenced convection onset times and onset manner somewhat, there was no major effect.

TABLE 8. APOLLO 17: MANNER OF CELLULAR CONVECTION ONSET

Apollo 17		
2-mm Case	7.5-W Heating	<ul style="list-style-type: none"> ● Polygonal cells start in center of pan first. Side roll about a second later. Cells invade side roll about 3 min 28 sec later.
4-mm Case	5-W Heating	<ul style="list-style-type: none"> ● Large circular cells which subdivide into smaller cells. ● Side rolls and center polygonal cells form at the same time. ● Cells eventually fill entire pan.
	7.5-W Heating	<ul style="list-style-type: none"> ● About same size cells as at low heating rate. Flows are faster, however.
Ground Tests		
2-mm Case		Rings first form around edge which then break down into cells. Cells appear in center last.
4-mm Case		
Apollo 14 Case		
Fluid volume sufficient to form 2-mm layer on ground. Fluid depth in center of pan about 0.25 mm.		Polygonal cells form in 8 min in thin center layer. Cells toward edge of pan form about 23 sec later.

B. Radial and Lineal Heating Experiments

Figures 16 and 17 are typical of the curves obtained from the motion picture film of the Apollo 17 Radial Heating Experiment. The solid theoretical curves were calculated by computer assuming that conduction and radiation are the only forms of heat transfer present. A discussion and evaluation of possible errors associated with the experimental curves are given in Appendix C. Details of the thermal modeling and a full set of temperature-time curves are given in Appendix D. For comparison a similar typical curve obtained from Apollo 14 HFC is shown in Figure 18.

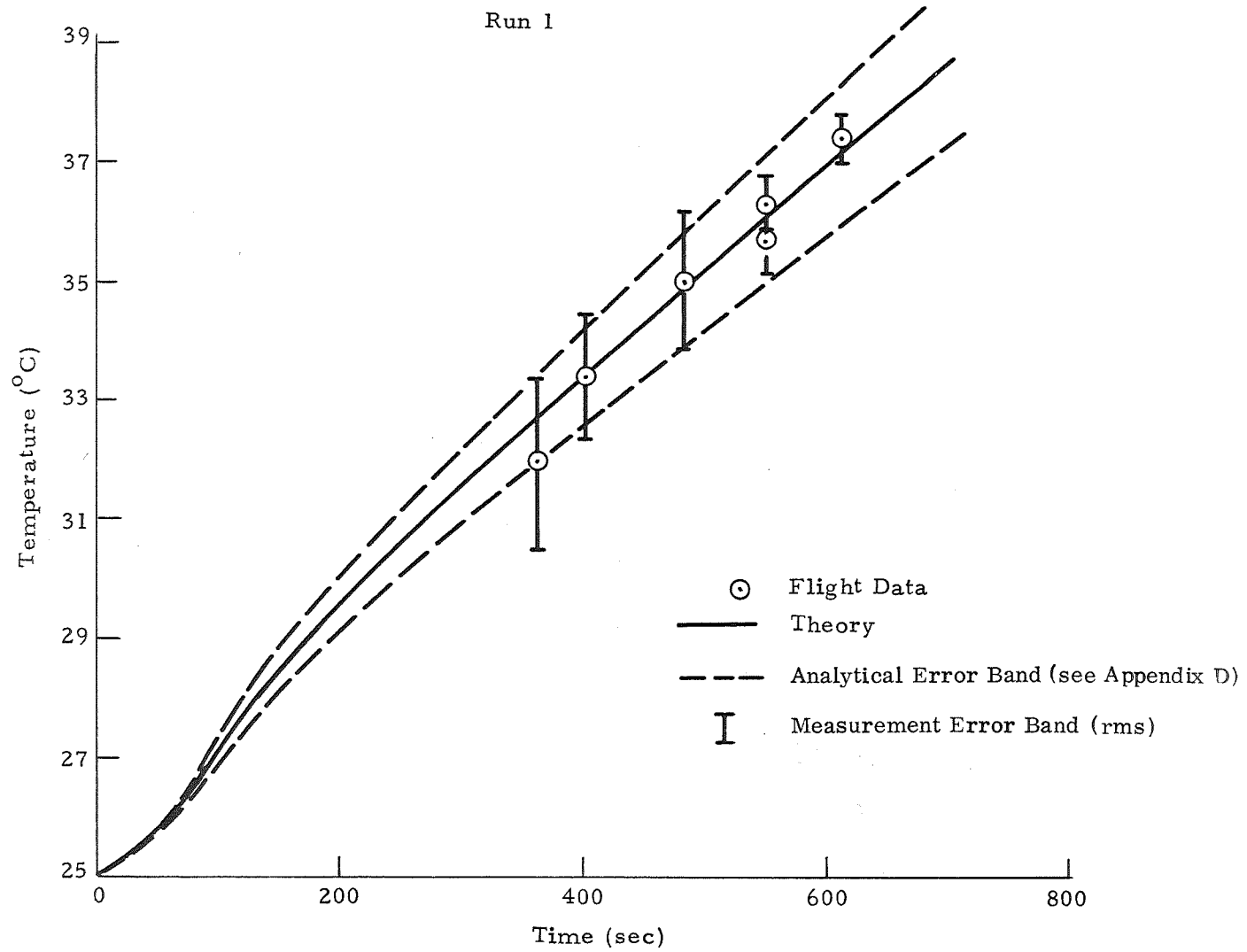


Figure 16. Temperature-time curve at 0.50 cm from Radial heater post.

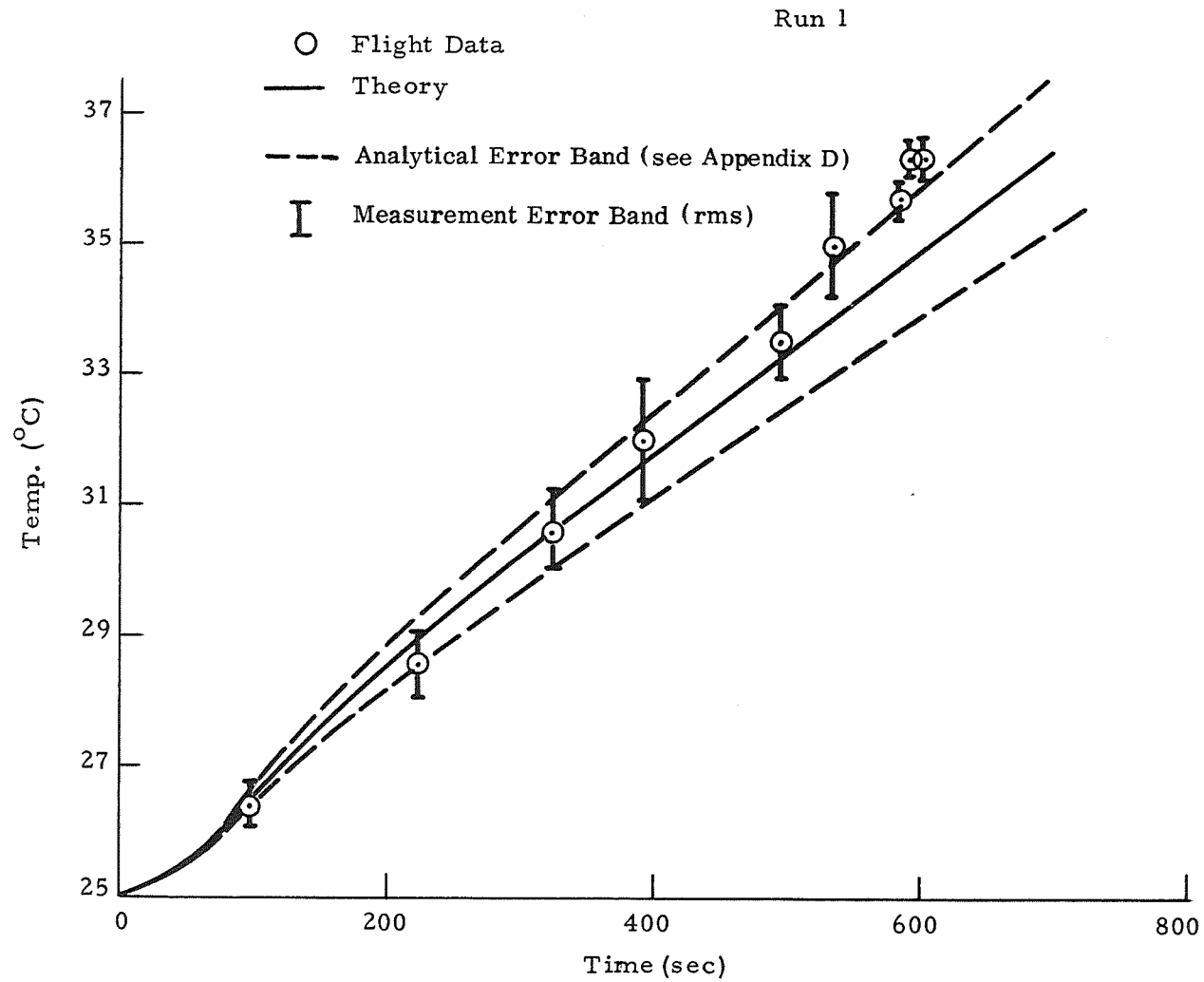
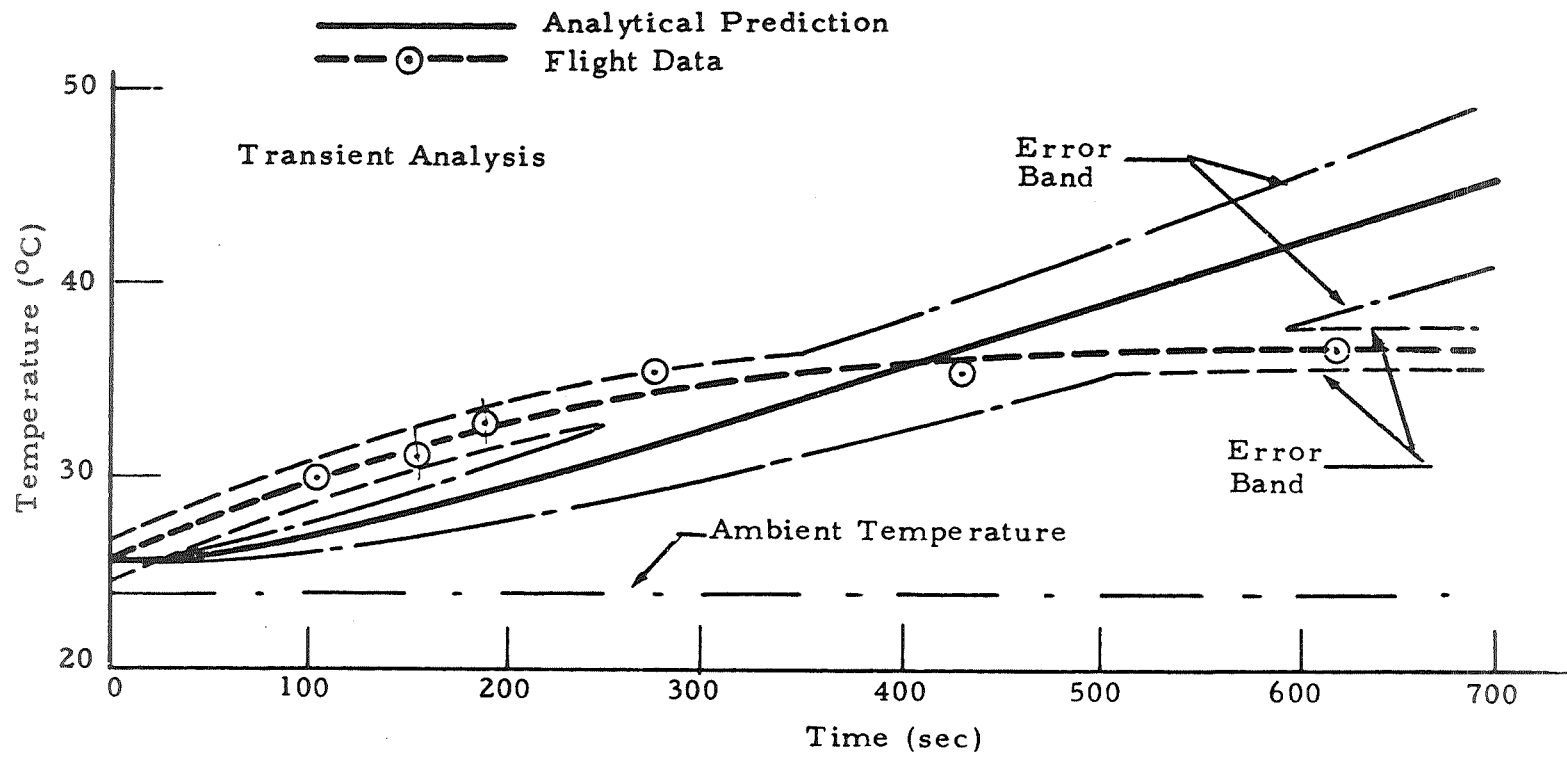


Figure 17. Temperature-time curve at 0.75 cm from Radial heater post.



Figures 19 and 20 are typical of the curves obtained from the Apollo 17 HFC motion picture film of the Lineal Heating Experiment. As in the Radial Heating Experiment, the solid theoretical curves are the theoretical conduction-radiation curves. Details of the thermal modeling of the Lineal cell are given in Appendix D along with a full set of flight curves. For comparison, a similar typical curve obtained from the Apollo 14 Zone Heating Experiment is shown in Figure 21.

Run 1

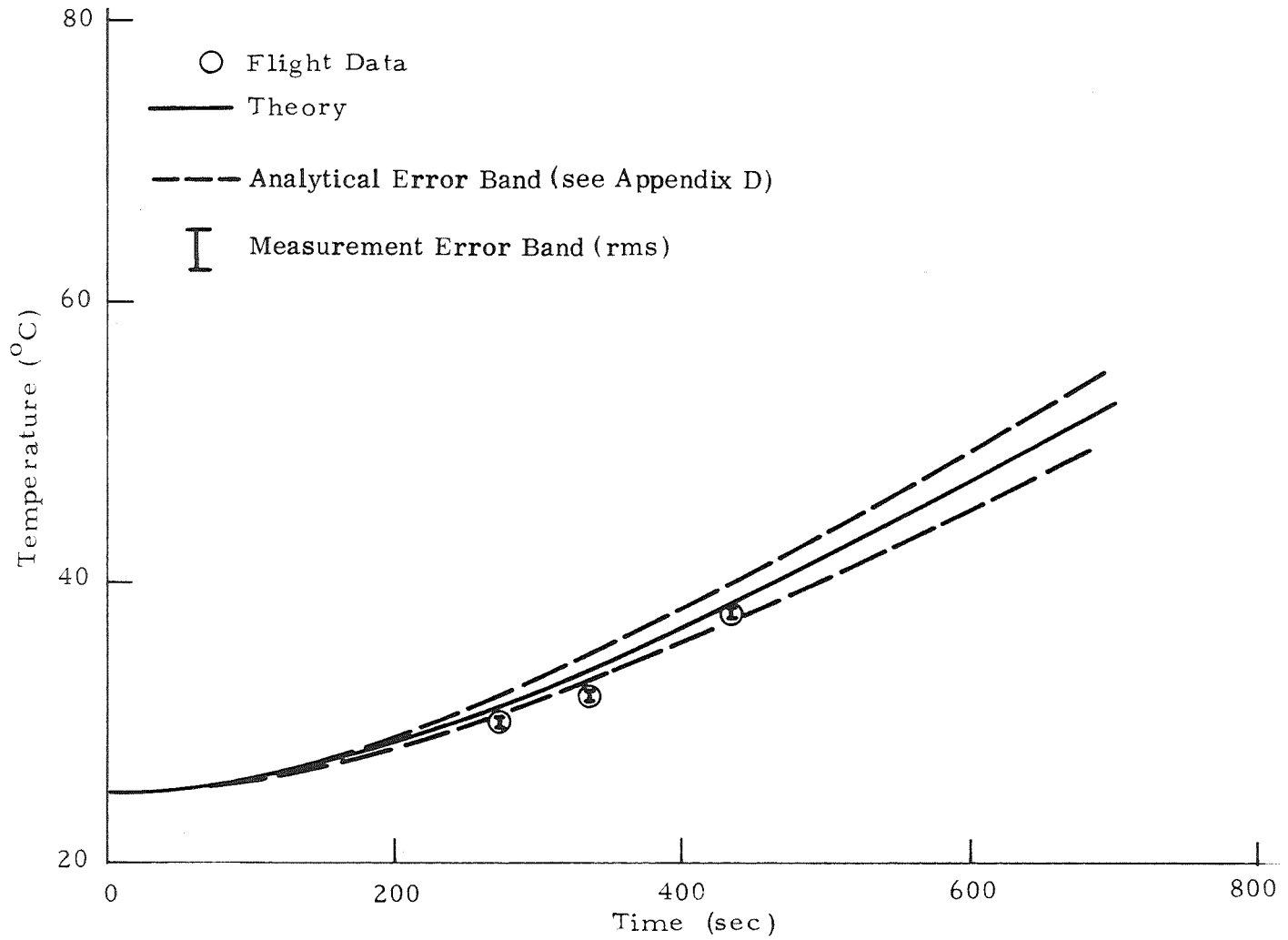


Figure 19. Temperature-time curve at 0.9 cm from Apollo 17 Lineal heater, heating rate = 18.0 W.

Run 2

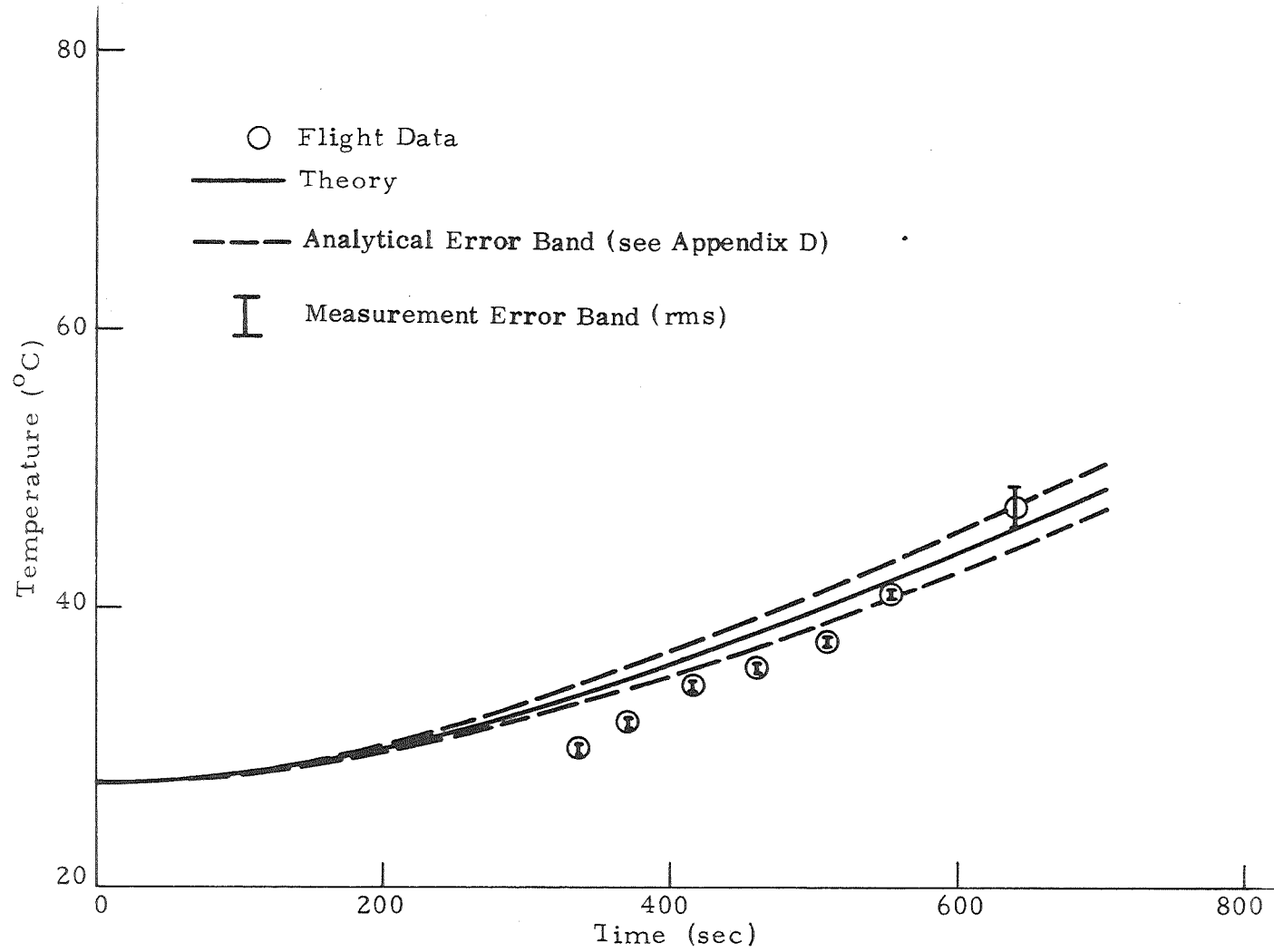


Figure 20. Temperature-time curve at 1.1 cm from Apollo 17 Lineal heater, heating rate = 18.0 W.

Transient Analysis

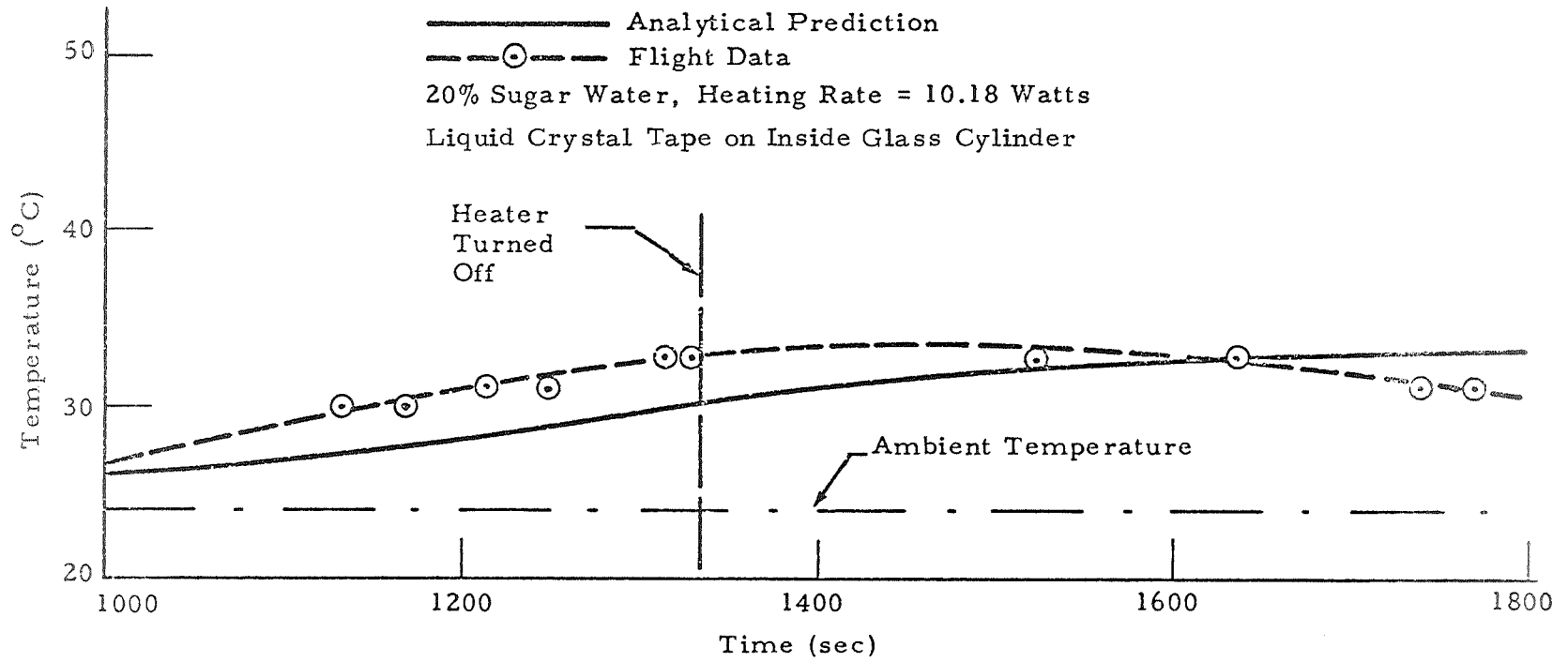


Figure 21. Zone heating temperature 3.165 cm from cell center (Apollo 14).

IV. INTERPRETATIONS

A. Summary of Interpretations

Flow Pattern Experiment

- The sizes of the observed surface tension-driven convection cells agree fairly well with those predicted by linear analysis of surface tension-driven, cellular convection.
- Convection occurred at lower temperature gradients in low-g than in one-g. Surface tension and gravity, therefore, apparently do not reinforce each other in a manner predicted by one analysis of cellular convection.
- The Flow Pattern Experiment data substantiate in principle the postulate that gravity modulates cellular convection onset.
- The onset of a concentric side roll and center polygonal cells in the Flow Pattern Experiment occurred at about the same time. The occurrence of a roll is contrary to expectations based on latest literature. The observed onset pattern tends to confirm an earlier view that rolls are side wall effects and are not particularly characteristic of the driving mechanism.

Radial and Lineal Heating Experiments

- No significant convection was observed in the Radial or Lineal Heating Experiments. The data, however, validate the accuracy of the measuring technique and allow the conclusion that:
- The convection observed in the Apollo 14 Radial and Zone cells was probably caused by HFC unit and spacecraft vibrations.

B. Flow Pattern Experiment

Briefly, the Apollo 14 Flow Pattern Experiment showed [10]:

- Surface tension alone can drive cellular convective flow of visible magnitude.
- A critical temperature gradient is required for surface tension-driven cellular convection.

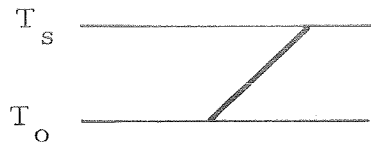
- A polygonal cellular pattern is preferred for surface tension-driven convection in a thin liquid layer of uniform thickness.

- A low-g, edge type, surface tension-driven convection is caused by a radial temperature gradient.

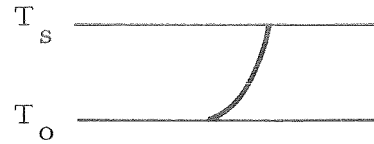
Because the Apollo 17 experiment produced more quantitative data, more rigorous comparisons with theory are therefore possible. In the following discussions the Apollo 17 data are compared to the predictions of a number of theories. It is found that the size of the observed Apollo 17 convection cells are in fair agreement with the predictions of Pearson's theory [14]. The observed Apollo 17 convection onset times, however, indicate that, contrary to Nield's theory [15], gravity and surface tension are not coupled in a manner that would result in strong reinforcement at all convective wavelengths; i. e., if the cells caused by gravity and by surface tension tend to be the same size, then they tend to annul fluid motion. If the cell sizes tend to be considerably different, however, then gravity and surface tension tend to reinforce motion. Although the determinants of possible cell size at present are not well understood, the dimensions of the container and the fluid depth are probably two of the most important. The latter interpretation derives from the theories of Scriven and Sternling [16] and of Smith [17] which take into account possible surface deformations.

Before comparisons with theory are discussed, it may be well to mention that the mean $10^{-9} g_e$ gravity level obtained during performance of the Apollo 17 HFC Flow Pattern Experiment was much too low to have caused the cellular convection observed. The value of the critical Rayleigh number, which must be exceeded for gravity-driven cellular convection to occur in a layer of fluid heated from below, is on the order of 513. (See Appendix B for a discussion of dimensionless numbers.) In the Apollo 17 case, the Rayleigh number at the time convection was seen to occur was on the order of 10^{-7} . Thus, the Apollo 17 cellular convection was driven by surface tension alone. The Apollo 17 data, therefore, can serve to yield information not only on the nature of pure surface tension-driven convection but also on the manner in which surface tension couples with gravity on earth.

1. Comparisons with Linear Theories. We consider here Pearson's and Nield's theories of cellular convection. Pearson's theory deals with cellular convection driven by surface tension alone. Nield's theory takes into account surface tension and gravity. Both theories require that the temperature gradient through the liquid be linear at the onset of convection, as shown in the following sketch.



linear temperature gradient



non-linear temperature gradient

To achieve linear temperature profiles in actual practice, very slow heating rates are used. In the Apollo 14 and 17 Flow Pattern Experiments fairly substantial heating rates were used. Pearson's and Nield's theories also assume a rigid nondeformable liquid surface. This assumption is usually not realistic. The surface of a convecting layer of Krytox oil does show considerable deformation [5]. A further assumption of both theories is that the layer of fluid being heated is infinite in extent. The theories of Pearson and Nield, therefore, are not strictly applicable. They do serve, however, as points of comparison. The effects of side walls, temperature nonlinearity, and surface nondeformability on the predictions of Pearson's and Nield's theories are considered subsequently.

The theoretical predictions of Pearson's and Nield's theories are presented in Table 9 in summary form.

A comparison of Pearson's prediction of the values of the critical Marangoni number and the cell size for the conditions of this experiment to the Apollo 17 results is presented in Table 10.

It can be seen that the observed cell sizes compare quite well with those predicted by Pearson's theory. The observed values of the critical Marangoni number, however, are higher. The given observed values, however, should really not be compared to Pearson's predicted value because the observed values were calculated from nonlinear temperature profiles as discussed in Section III.

Nield's theory would lead to the expectation that the onset of convection would occur later (at larger temperature differentials) in the zero-g case than in the one-g case. According to Nield's theory the convective driving forces of surface tension and gravity reinforce each other. Actual data showed just the reverse trend. Table 11 summarizes the actual comparisons.

The Apollo 17 data indicate that surface tension and gravity do not reinforce each other. Surface tension and gravity apparently work against each other. Before any conclusions can be reached regarding Nield's theory, a number of other considerations need to be discussed because Nield's theory has received experimental verification [18] in one-g conditions when very slow

TABLE 9. SUMMARY OF THEORETICAL PREDICTIONS
OF CELLULAR CONVECTION

<u>Pearson's Theory</u>					
●	Value of critical Marangoni Number (Ma) 80.				
●	For a given temperature gradient a critical liquid depth exists.				
●	Diameter of convecting cell, ℓ $\left(\ell = \frac{4\pi d}{3a} \times 1.732 \right)$				
	<table style="margin-left: 40px;"> <tr> <td>$d = 2 \text{ mm}$</td> <td>4 mm</td> </tr> <tr> <td>$\ell = 7.3 \text{ mm}$</td> <td>14.6 mm</td> </tr> </table>	$d = 2 \text{ mm}$	4 mm	$\ell = 7.3 \text{ mm}$	14.6 mm
$d = 2 \text{ mm}$	4 mm				
$\ell = 7.3 \text{ mm}$	14.6 mm				
●	Presence or absence of convection depends on direction of temperature gradient.				
<u>Nield's Theory</u>					
●	Gravity and surface tension couple in a manner such that convection is easier to initiate when coupling is present than when it is not.				
●	Presence of convection possible when heating from above or below .				

TABLE 10. COMPARISON OF APOLLO 17 FLOW PATTERN
RESULTS WITH PEARSON'S THEORY

	Pearson	Apollo 17
Critical Marangoni Number	80	400 (2-mm layer) 1320 (4-mm layer)
Diameter of Convecting Cells	7.3 mm (2-mm layer) 14.6 mm (4-mm layer)	7 mm (avg) 14 mm (avg)

TABLE 11. FLOW PATTERN CONVECTION ONSET TIMES
AND CORRESPONDING MARANGONI AND RAYLEIGH NUMBERS

Test	Fluid Depth, mm	Onset Time, ^a sec	Ra	Ma	Heat Rate, W
Ground Test	1.97	120	695	927	7.56
Apollo 17 Flight Test	~1.89	18	3×10^{-7}	400	7.56
Ground Test	3.96	120	7710	2580	5.18
Apollo 17 Flight Tests	~3.73	48	4×10^{-6}	1320	5.18

a. Time interval from moment heat turned on to moment convection first observed.

heating rates were employed. The Apollo 17 data, therefore, can only mean that nonlinear or boundary effects not included in Nield's theory are responsible for the observed nonreinforcement of gravity and surface tension.

In the following paragraphs some possible influences which could modify the conclusions of Nield's theory are considered.

2. Effect of Fluid Properties, Side Walls, and Other Realistic Boundary Conditions. A number of analyses have considered the effects of more realistic boundary conditions and of fluid properties on the values of the critical Rayleigh and Marangoni numbers. The effects of quantities such as the Prandtl number, Biot number, aspect ratio, heater versus fluid thermal conductivity, and sidewall conditions have been considered in varying detail. Table 12 gives values of various dimensionless parameters for the Apollo 17 case. Assuming that a linear temperature profile exists in the fluid layer,

TABLE 12. APOLLO 17 CONVECTION DIMENSIONLESS PARAMETERS^a FOR FLOW PATTERN UNIT^b

Parameter	Value
Prandtl Number	444
Biot Number	1
Aspect Ratio $\left(\frac{\text{radius}}{\text{depth}}\right)$	9
$k_{\text{Heater}}/k_{\text{Krytox}}$ ^c	1000
Crispation Number	4×10^{-5}
Bond Number	3×10^{-5}

- a. See Appendix B for definitions of the various dimensionless parameters.
- b. Fluid consists of Krytox 143AZ oil at a depth of 2 mm. Physical properties evaluated at 38°C (100°F).
- c. The symbol k represents thermal conductivity. The heater material is aluminum.

the preceding parameters and the Apollo 17 boundary conditions result in a critical Marangoni number of 115 [17, 19] and a critical Rayleigh number of 513 [20]. With the exception of Bentwich [19], no theoretical or experimental studies were found in the literature regarding the edge effects (aspect ratio and sidewall thermal conditions) on cellular motion induced by surface tension forces. Thus, the preceding value of the Marangoni number does not include possible edge effects. (See Appendix B for a further discussion of these effects on criticality conditions.)

Although the critical Marangoni number is raised from 80 to 115 when more realistic fluid properties and boundary conditions are considered, the observed flight values of 400 (2-mm layer) and 1320 (4-mm layer) and ground values of 787 (2-mm layer) and 2341 (4-mm layer) are still quite a bit higher. Existing theories of fluid property and boundary condition corrections, therefore, cannot account for the discrepancies.

One other possible explanation for the increased ΔT required on the flight test is the unsteady gravity level or g-jitter which existed. Previous investigations of heating-from-below problems have shown that time-varying gravity increases the critical Rayleigh number [21, 22].

3. Effect of Temperature Nonlinearity. To assess the effect of temperature nonlinearity on the predictions of Pearson's and Nield's theories, the conclusions of a number of papers dealing with this topic were considered. A summary of these conclusions is presented in Table 13.

An examination of the various conclusions presented in Table 13 indicates that the theoretical situation is contradictory and unsettled. On the basis of the experimental papers, however, it can be concluded that a finite heating rate sufficient to cause a nonlinear temperature profile prior to the onset of convection probably would cause both the critical Marangoni and Rayleigh numbers to be larger than predicted by linear theory. The larger critical Marangoni numbers (compared to Pearson's prediction) obtained in the Apollo 17 Flow Pattern Experiment are, therefore, explainable on this basis. An exact analysis does not exist, unfortunately, for the case of surface tension-driven convection caused by relatively fast heating from below. Quantitative comparisons, therefore, cannot be made at present.

Temperature nonlinearity, on the other hand, does not seem a likely explanation for why the data of Table 11 are not in accord with expectations derived from Nield's theory. Experimental data indicate fast heating increases the critical Rayleigh and Marangoni numbers. Thus, if surface tension and

TABLE 13. SUMMARY OF LITERATURE CONCLUSIONS REGARDING
NONLINEAR TEMPERATURE PROFILES

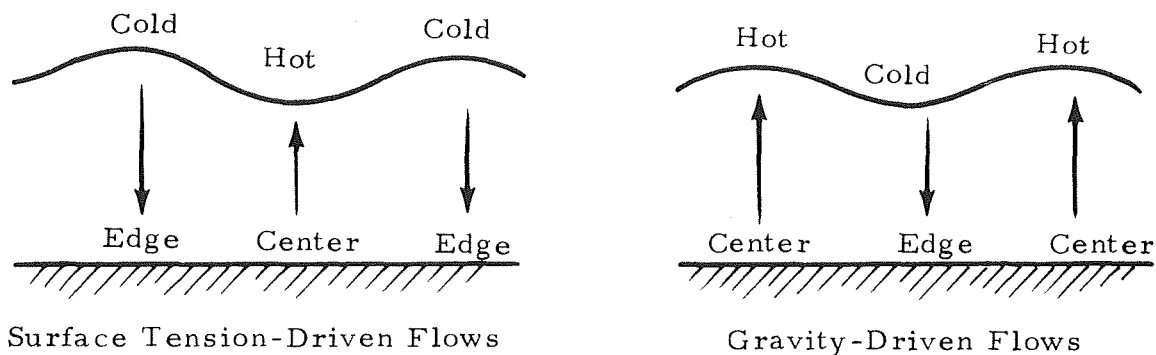
Investigators	Type of Investigation	Assumptions or Boundary Conditions	Conclusions
Vidal and Acrivos, 1968 [23]	Theoretical	Surface tension only driving force Nondeformable surface Infinite layer Cooling from above	Nonlinearity increases critical Marangoni number over that obtained in linear case
	Experimental	Evaporative cooling	
Currie, 1967 [24]	Theoretical	Gravity only driving force Heating from below Infinite layer Two rigid bounding surfaces	Temperature nonlinearity increases critical Rayleigh number
Berg et al., 1966 [25]	Experimental	Evaporative cooling	Nonlinearity increases critical Marangoni number
Debler and Wolf, 1970 [26]	Theoretical	Surface tension and gravity driving forces Heating from center Nondeformable surface	Nonlinearity decreases both critical Rayleigh and Marangoni numbers
Sparrow, Goldstein, and Jonsson, 1964 [20]	Theoretical	Gravity only driving force Free upper surface Rigid upper surface also considered Heating from center	Nonlinearity decreases critical Rayleigh number Rapid heating decreases critical Rayleigh number
Soberman, 1959 [27]	Experimental	Rigid upper and lower surfaces Heating from below	Faster heating increases critical Rayleigh number
Davenport and King, 1973 ^a	Experimental	Surface tension and gravity No meniscus effects Cooling from above	Nonlinearity increases critical Marangoni number to infinity

a. Davenport, I. F.; and King, C. J.: An Experimental Study of Convection Initiation in Deep Pools. Submitted to *J. Fluid Mechanics*, September 1972.

gravity reinforce each other, as Nield would have it, convection in the zero-g case should have started later, not sooner, than in the one-g case.

4. Effect of Surface Deformations. Two theoretical papers [16, 17] have investigated the consequences of Pearson's and Nield's assumption of a nondeformable liquid-gas interface. A summary of the conclusions of these papers is given in Table 14.

The matter of the influence of surface deformation on the stability of a heated layer was considered briefly in still another study [5]. In that study it was pointed out in Nield's result that surface tension and gravity reinforcing one another appears reasonable in light of the assumption made by Nield that the surface is nondeformable. When the surface deflections resulting from surface tension and from gravity-driven flows are considered, however, Nield's conclusion seems contrary to expectation. For example, a representation of the flows as viewed from the side and occasioned by gravity and by surface tension is shown in the following sketch [28].



As can be seen the deformations in the hot areas and the deformations in the cold areas are exactly opposite. A nulling action rather than a reinforcing action would thus be expected. The matter of possible cell size, however, was not considered in the cited study.

In the papers of Scriven and Sternling and of Smith the matter of possible cell size is considered. The manner in which cell sizes are discussed in these two papers, however, is in terms of fluid stability to disturbances of a certain wave number. A footnote in the Scriven and Sternling paper notes that [16]

TABLE 14. SUMMARY OF ASSUMPTIONS REGARDING SURFACE DEFORMABILITY

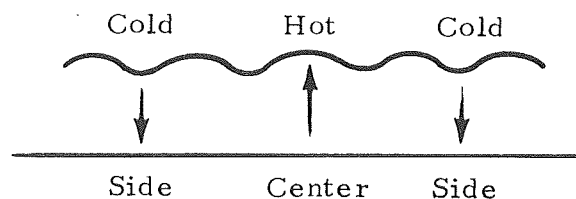
Theory	Convective Driving Forces	Assumptions	Conclusions
Pearson [14]	σ	<ul style="list-style-type: none"> ● Nondeformable surface ● Infinite layer 	Critical Ma needed for convection onset
Nield [15]	$\sigma + g$	<ul style="list-style-type: none"> ● Nondeformable surface ● Infinite layer 	$\sigma + g$ reinforce each other
Scriven and Sternling [16]	σ	<ul style="list-style-type: none"> ● Deformable surface ● Infinite layer 	No critical Ma needed for convection onset
Smith [17]	σ	<ul style="list-style-type: none"> ● Deformable surface ● Infinite layer ● Effect of gravity on surface deformation considered 	Critical Ma needed for convection onset

"for ordinary liquids in horizontal layers 1 mm or more deep the action of gravity becomes significant for wavelengths exceeding about 5 mm and could very well stabilize disturbances of longer wavelength if the free interface is on top."

The quote is translated to mean that if cells of more than 5-mm diameter tried to form, gravity would damp them out. In a zero-g condition, however, formation of larger size cells would meet with no interference from gravity. Smith's analysis confirmed Scriven and Sternling's expectation that gravity would stabilize a system with a free upper surface.

The observed easier onset of convection in the Apollo 17 case as compared to ground tests is, therefore, in general accord with Scriven and Sternling's and Smith's analyses. The fact that a finite time was taken for convection onset means that a critical Marangoni number still exists. The existence of a critical Marangoni number in the flight case is probably the result of the fact that the layers in the flight case were not infinite in extent so they, therefore, could only accommodate convection cells of certain large sizes. These sizes, however, would have been damped out in one-g conditions. In a recent telephone conversation, Dr. Scriven expressed agreement with this interpretation.

The fact that Nield's theory, as has been mentioned previously, has been experimentally verified under one-g conditions must mean that gravity and surface tension reinforce each other when the possible gravity cells are much larger than the possible surface tension cells. The reinforcement must operate somewhat in the manner shown below.

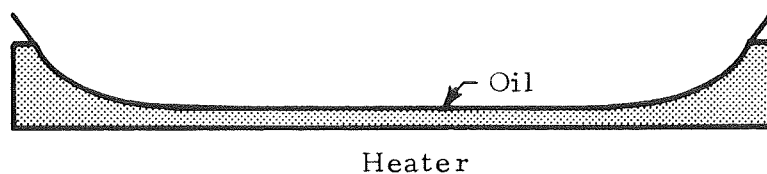


If both the gravity and surface tension cells were the same size, they would cancel flow.

5. Comparisons with Theories of Cell Morphology. The manner of convection onset is summarized in Table 8. One of the most notable features

of the onset noted in the Apollo 17 case was the formation of both rolls and polygonal cells. A number of papers have appeared which deal with the subject of what determines the shape of the convection cells. In a circular pan such as was used in the Apollo 14 and 17 experiments, only two types of cells need concern us: concentric roll cells and polygonal — tending toward the hexagonal — cells. The situation regarding the determinates of cell shape is rather confused because linear theories do not predict cell shapes and nonlinear theories are fraught with difficulties. The general consensus in the literature is that rolls are associated with buoyancy-driven convection and polygons primarily with surface tension [29]. Koschmieder [30] contends that the rolls are caused by the lateral wall and are not particularly determined by the driving force. Koschmieder further holds that if the temperature were carefully controlled above the oil-air interface, polygonal cells would not form immediately. Rolls would first develop which would then break down into polygonal cells. The topic is of enormous importance to the theory of cellular convection. It would therefore, be extremely worthwhile to repeat the Flow Pattern Experiment under carefully controlled conditions at the upper free surface to see whether convection first begins with a pattern of rolls and then breaks down into polygons. Such conditions probably will exist on the proposed Space Shuttle.

The fact that cellular convection started in the cell center as well as in the rolls after a short period of time is in accordance with the Apollo 14 HFC observations. In the case of the Apollo 14 HFC, however, such a large meniscus was present, as shown by the sketch, that the observed edge convection was probably not related to the observed center cellular convection.



Shape of Apollo 14 Flow Pattern Oil Layer

C. Radial Heating Experiment

The fact that the form of Apollo 14 temperature-time curves differed from those of Apollo 17 can be attributed to the presence of convection on Apollo 14 and the lack of convection on Apollo 17. A number of causes for the observed Apollo 14 convection are possible. These are:

- Gravity (buoyancy convection).
- Fluid thermal expansions (thermoacoustic convection).
- HFC unit and spacecraft vibrations (random convection).
- Coupled forces.

In the following discussions the experimental conditions for the Apollo 17 and 14 cases are compared to provide evidence for identifying the probable convective force. The comparisons indicate that greater spacecraft vibrations on Apollo 14 than on Apollo 17 are the most probable explanation for the observed data.

1. Buoyancy Convection. With regard to gravity-driven convection, the Radial unit is a "heating from the side" problem. As described in Appendix B, there is no critical Rayleigh number ($Ra_c = 0$) so far as fluid motion is concerned. There remains, however, a critical Rayleigh number above which heat transfer rate increases appreciably. There is also a critical Rayleigh number above which small vortices occur in the corners of the container. This effect, however, does not alter the heat transfer rate appreciably as compared with conduction [31]. Marangoni criteria for this experiment are irrelevant because no fluid-fluid interface exists for surface tension to become a significant driving force.

Experiments have been conducted on the ground for a gas confined in a rectangular container having isothermal vertical walls at different temperatures and insulated top and bottom plates [32]. The critical Rayleigh number was found to be

$$Ra_c = 500 H/L \quad , \quad (1)$$

where H is the height and L is the length of the container. This result agrees with the theoretical prediction of Batchelor [31]. The preceding relation can be used to estimate the degree of buoyant thermal convection occurring in this experiment. This estimation must be considered an order-of-magnitude analysis, however, because the system investigated and the fluid are not quite the same. A comparison of the theoretical critical and existing Rayleigh numbers for the flight experiment is, assuming a nominal gravity level of $10^{-9} g_e$, as follows:

Ra of Apollo 17 Radial Cell During Flight Experiment 32×10^{-5}

Ra_c Theoretical 400 .

These numbers were based on the radius of the cell. The average properties of argon for the temperature range of interest and the maximum temperature gradient possible in the cell were utilized. The maximum possible temperature gradients were generated using the conduction-radiation thermal model. (See Appendix D.)

It is evident that

$$Ra/Ra_c \cong 8 \times 10^{-7} \ll 1 ,$$

which means the likelihood of buoyant thermal convection was negligible in the flight test even when the temperature gradient was at a maximum. Furthermore, the theoretical critical number indicates that a gravity level of at least $10^{-3} g_e$ for the calculated temperature gradient is required to induce manifest buoyant, thermal convection. Thus, it may be concluded that sustained convection in the radial heating unit caused by gravity alone is unlikely, because the maximum g-level never exceeded $10^{-6} g_e$.

Convection sensitivity criteria for the Apollo 14 Radial cell flight test indicate that $Ra/Ra_c \cong 2 \times 10^{-6}$. For the Apollo 14 unit, the properties of CO₂ were used and a nominal gravity level of $10^{-9} g_e$. Thus, it can be concluded that although buoyant thermal convection was more probable in the Radial unit of Apollo 14 than Apollo 17, the possibility of such convection in either case is negligible.

The preceding analysis is based on the use of dimensionless numbers and can only indicate order of magnitude. More precise information is obtained from computer calculations. In the course of other studies a general computer program was developed which allows calculation of convective effects caused by gravity and thermal volume expansions. This program is called the Lockheed General Convection Program (LGCP). Details of the convection modeling used in this program are given in Appendix E. A convection analysis, using the computer program, was performed on the Apollo 14 and 17 Radial

cells in an attempt to explain the different behavior of the two flight experiments. The following paragraphs present the results of the computer analysis.

Runs were made for both the Apollo 14 and 17 cells with a constant g as a parameter. In addition, gravity oscillations or g -jitter effects were examined by inputting the actual time-varying gravity components into the computer program. The effects of thermal expansion convection alone were analyzed by using $g = 0$. (See Section IV.C.2 for an explanation of thermal expansion or thermoacoustic convection.) The results of these and other parametric studies are summarized in the following paragraphs.

The first cases studied consist of the Apollo 14 and 17 geometries and fluids at $g = 0$. These cases were run to determine the magnitude and influence of thermal expansion-driven convection in the absence of gravity. The results for both the Apollo 14 and 17 cells indicate very little increased heat transfer due to "thermoacoustic effects." The average increase in the temperature at the liquid crystal strip at $t = 600$ sec is of the order of 0.5 percent for the Apollo 17 cell and 1 percent for the Apollo 14 cell. This small difference between the pure conduction values and the thermoacoustic convection values is well into the noise level of any flight data taken. It can thus be concluded that thermal expansion convection alone contributed very little to the heat transfer in the Radial Cell Experiment.

The next cases analyzed consist of a simulation of the Apollo 17 HFC Radial cell at a constant level, $g = 10^{-6}$. Thus, both thermoacoustic and gravity-driven convection are possible. In addition, parametric cases were run with $g = 10^{-3}$ and $g = 1$ to determine the trends and magnitude of the effects of gravity on the Radial cell. The results are summarized in Figure 22. The temperature-time history of the crystal strip at $r = 0.6$ cm from the heater post is shown in Figure 22. The solid line is the pure conduction curve, and the circles are the actual HFC flight data. The 10^{-6} g case, which is also shown as the solid line, provided less than 1-percent change over the pure conduction curve. This reinforces the conclusion that no significant convection occurred in the Apollo 17 Radial Cell Experiment.

The $g = 10^{-3}$ and $g = 1$ cases show significant increases in the temperature profile over that predicted by a pure conduction analysis. This increase in the temperature of the liquid crystal strips is a result of gravity-induced buoyant forces causing fluid circulation, thus transferring more heat per unit time to the "top" of the cell. It is interesting to note that the convection curves do not bend over with time, but appear to be continually rising at $t = 600$ sec. This is verified by examining the heater post temperature-time

Apollo 17 HFC - Radial Argon

$r = 0.6 \text{ cm}$

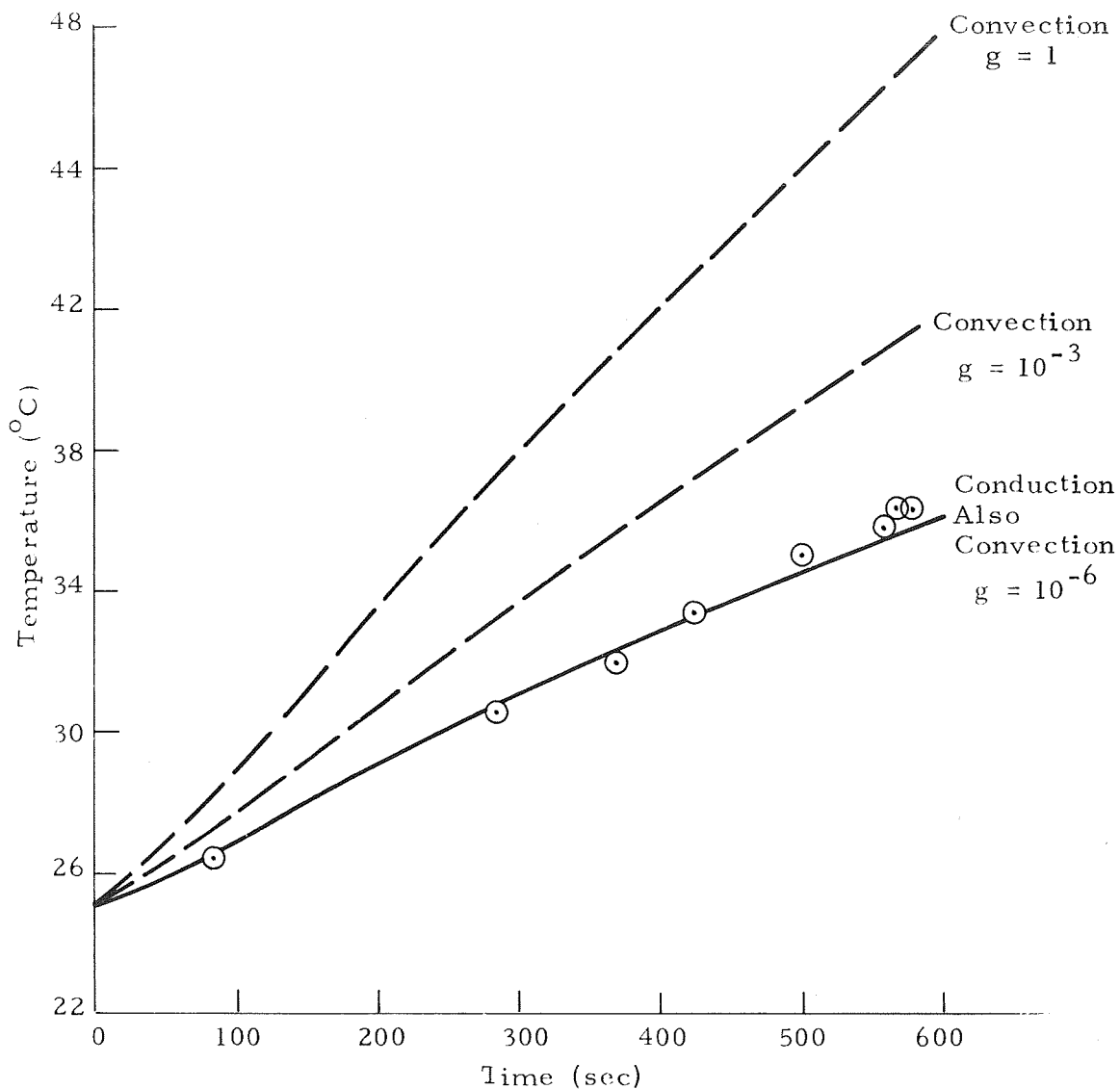


Figure 22. Temperature versus time at $r = 0.6 \text{ cm}$ in the Radial cell for varying gravity levels.

profile which has also not flattened out at $t = 600$, but is still supplying heat input to the gas. It thus appears that a steady state was not approached during the Apollo 17 HFC Radial Cell Experiment.

The computer program provides contour maps of the thermal and flow fields at selected time points. Figures 23 and 24 are shown for the Apollo 17 Radial cell at $t = 600$ sec. Figure 23 is an isotherm map showing bands of constant temperature in the r - z plane. The interesting feature of this map is the effects of the heater post geometry. The cylindrical post does not reach the crystal membrane, thus leaving a "gas-gap" above the post. This is illustrated by the contour map as the gas above the post is cooler than the post itself. Figure 24 is a contour map of the velocity field in the Apollo 17 Radial cell. Bands of constant velocity are shown in the r - z plane. These contours do indicate that a recirculating flow was set up in this cell. The magnitude of the velocities, however, is of the order of 0.6×10^{-4} cm/sec maximum. These are not large enough to affect the heat transfer significantly.

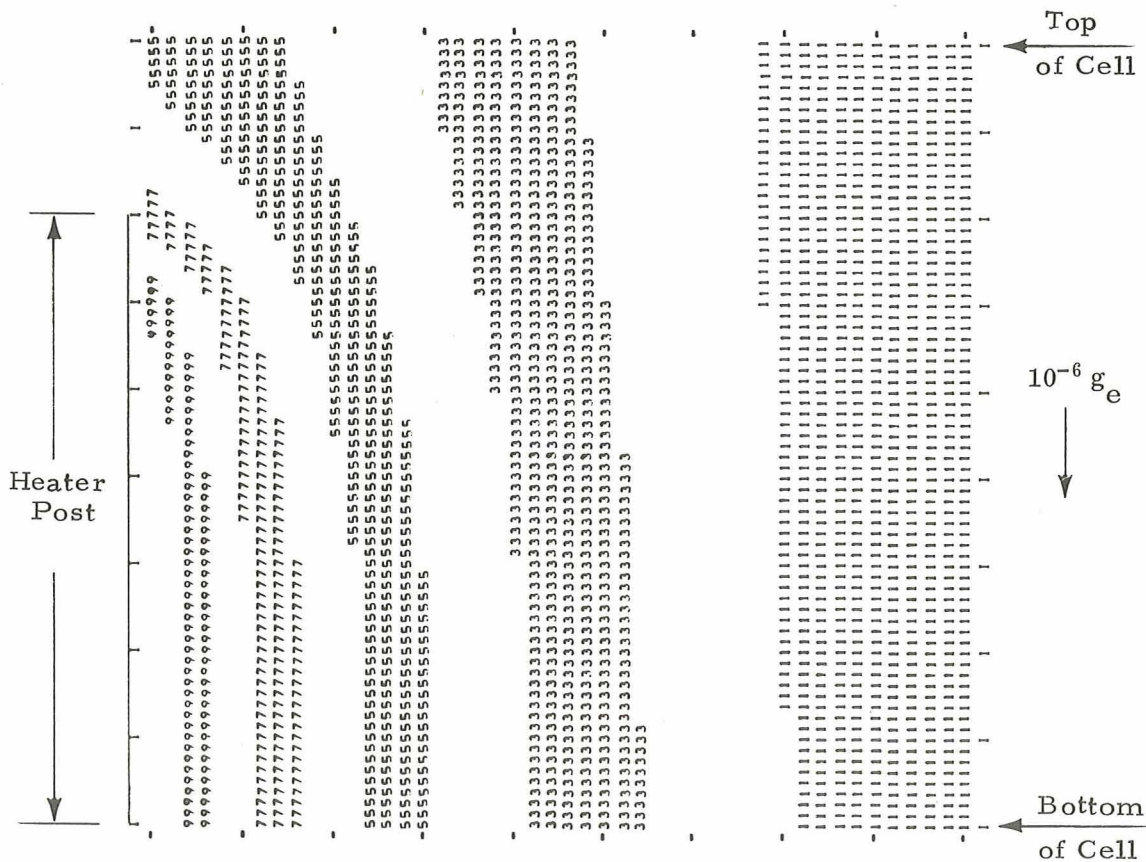


Figure 23. Theoretical isotherm maps at $t = 600$ sec in the Apollo 17 HFC Radial cell (1 indicates the lowest temperature, 9 the highest).

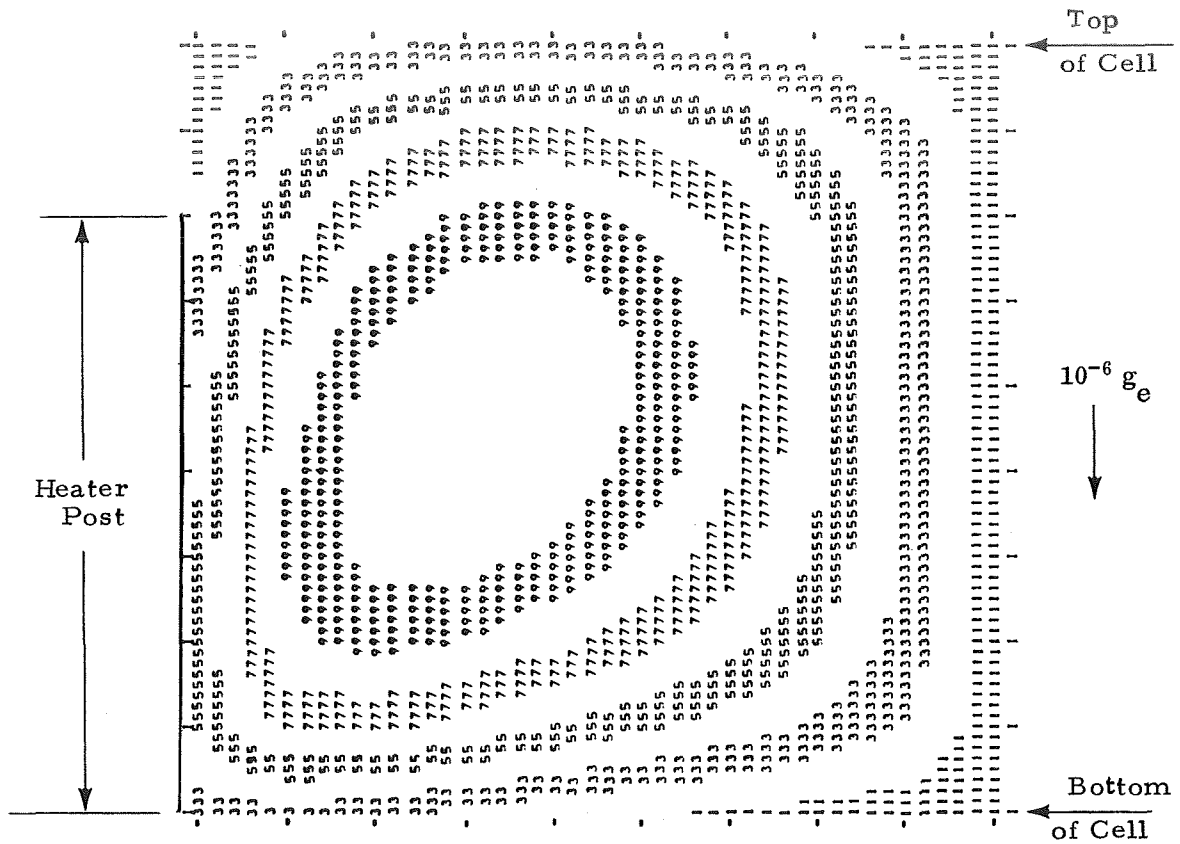


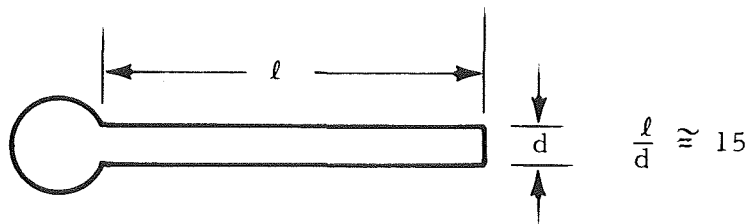
Figure 24. Theoretical velocity contour maps at $t = 600$ sec in Apollo 17 HFC Radial cell (1 indicates the lowest velocity, 9 the highest).

The same parametric cases were run for the Apollo 14 Radial cell with CO_2 as the gas. The magnitude and trends of the thermal and flow behavior were very similar to the Apollo 17 case. Again, no significant gravity convection occurred at the constant $10^{-6} g$ level. The larger gravity levels also produced similar curves to those shown in Figure 22. The convection curves, even at $g = 1$, do not bend over as indicated by the Apollo 14 HFC flight data. The primary conclusion which must be reached from this analysis is that gravity at the $10^{-6} g_e$ level, alone or even coupled with thermal volumetric expansion forces, could not have caused the type of behavior demonstrated by the Apollo 14 Radial cell data.

The effects of the g-jitter were examined by using a gravity-versus-time curve in the computer program. An oscillatory profile, with varying amplitude and frequency, was input and the case was run to $t = 600$ sec. For a maximum amplitude of 10^{-6} g, the oscillations made essentially no differences in the predicted temperature profiles. At this absolute g-level, the effects of varying frequency were also very negligible. This is not surprising since the constant $g = 10^{-6}$ case also shows no gravity-driven convection. It can be concluded that the observed fluctuations in the gravity level did not affect the heat transfer processes on the Apollo 17 HFC Radial cell. (See Section IV. C. 3 for further consideration of vibration effects.)

2. Thermoacoustic Convection. Convection caused by thermal volumetric expansion forces has been referred to previously. Because this type of convection is generally unfamiliar, a short discussion of its origins and characteristics is given here.

In the absence of gravity, a mechanism for convection can consist of the following. A suddenly heated wall causes adjacent fluid to expand. This sudden expansion sets up an acoustic wave which propagates into the fluid. Given a sufficient heat rate, container dimensions, and dissipative mechanisms, a thermoacoustic vibration can be sustained as long as the appropriate boundary conditions are maintained. The conversion of heat energy into acoustic energy was discovered and defined by Sondhauss in 1850. The phenomenon of the conversion of thermal energy into acoustic energy is now called the Sondhauss effect. The effect may be simply demonstrated by the following arrangement.



The end of the tube is open to the atmosphere. If the bulb is heated with a bunsen burner, the tube will emit an audible sound; i. e., it sings. In open or closed containers thermoacoustic waves can convect considerable heat from the heated site. The possibility was suggested that this type of convection might have been responsible for the form of the Radial and Zone curves

obtained in the Apollo 14 HFC Experiments [10]. Thermoacoustic convection has since been considered in some detail in a recent study [33]. In the cited study a computer program was written which allowed computation of the magnitude of heat transfer by thermoacoustic convection. Calculations made with the computer program have been discussed in the previous section. The results of the calculations showed, as mentioned previously, that although the Apollo 14 case showed more thermoacoustic convection than the Apollo 17 case, both are almost negligible. Apparently, the heating rates used on Apollo 14 and 17 were not high enough to generate significant thermoacoustic convection.

3. Random Convection (Spacecraft Vibrations). The possibility that spacecraft maneuvers, onboard machinery, and astronaut movement can cause convection in confined fluids was recognized [5], but a method of approximating the magnitude of onboard vibrations and of evaluating the subsequent effect on heat transfer was lacking at the time of the Apollo 14 data analyses. Recently, however, a paper by B. Gebhart was discovered [34] that provides a theoretical basis for estimating how spacecraft vibrations may affect heat transfer. In Appendix F a brief review of this paper is given. In the following, the implications of the paper with regard to the present study are considered.

First, to be able to make any sort of judgment on the extent of random vibration, some indication of the frequency and amplitude of vibrations is required. Data on g-levels were obtained from the gyroscope rate data for Apollo 14 and Apollo 17. (See Section II.) From these data the frequency and amplitude of the smaller, regular oscillations were determined. These are approximately as follows.

	<u>Approximate Frequency</u>	<u>Amplitude</u>
Apollo 17	20 sec	$2 \times 10^{-7} g_e$
Apollo 14 ²	200 sec	$5 \times 10^{-9} g_e$

The preceding data would lead to the expectation that vibrations were greater on Apollo 17 than on Apollo 14. Yet, time-temperature curves indicate

2. As previously discussed, the calculated g-jitter on Apollo 14 did not include roll-rate contributions and was calculated from 30-sec time intervals as compared to 2-sec time intervals on Apollo 17.

that convection occurred on Apollo 14 and not on Apollo 17. It must, therefore, be concluded that g-data, as calculated from rate gyros, do not sufficiently indicate actual vibration levels at the location of the experimental apparatus. One reason for this is the relatively long integration time interval required to obtain a g-data point and the subsequent fact that variation of roll rates was not included in Apollo 14 g-data. On Apollo 14, however, a couple of air bubbles were trapped in the Zone cell. By following the movement of these bubbles it was possible to obtain more accurate information on the frequency and amplitude of the vibrations at the location of the HFC unit. Figure 25 shows a typical curve of bubble displacement versus time. A g-jitter level sufficient to cause this displacement is estimated to be on the order of 10^{-3} to $10^{-4} g_e$.

From such curves it is estimated that the frequency of random vibrations during the Apollo 14 HFC Experiments was about 0.5 per sec with an amplitude of about 0.04 cm. According to Gebhart, the importance of random convection may be estimated by comparing the value of

$$\frac{C_n}{(F_m)^{\frac{1}{2}}}$$

with 1.0 (the pure conduction effect). The term F_m is given by

$$F_m = \frac{\alpha \tau_c}{s^2} ,$$

where α is the thermal diffusivity, τ_c is the period of the disturbance, and s is a significant dimension; C_n is a constant. Substituting the following values into the preceding formulas,

$$\alpha \text{ (for carbon dioxide) } = 0.18 \text{ cm}^2/\text{sec}$$

$$\tau_c = 2 \text{ sec}$$

BUBBLE MOTION FOR TIME SLICE 1

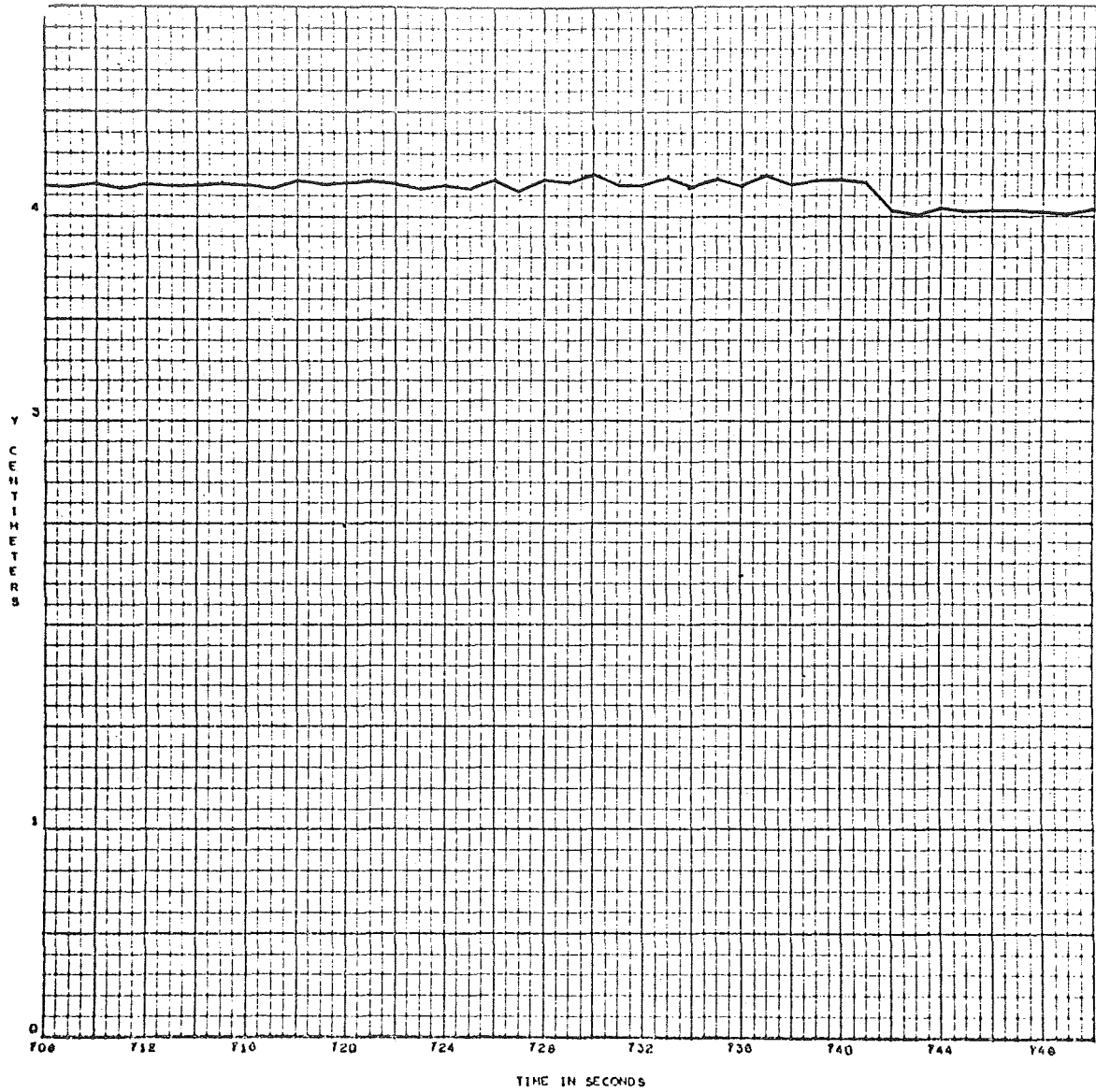


Figure 25. Bubble displacement in Apollo 14
Zone Heating Cell versus time.

$$s \text{ (height of heater post in Radial cell)} = 1.8 \text{ cm}$$

$$C_n \text{ (after Gebhart)} = 1.061 \text{ ,}$$

gives

$$\frac{C_n}{(F_m)^{\frac{1}{2}}} = 3.2 \quad .$$

This number indicates that the heat transfer caused by random convection is some 3.2 times greater than that caused by pure conduction. The actual amount of convection heat which was estimated from the Apollo 14 data was between 10 and 30 percent over the pure conduction case. The preceding calculation is, of course, very approximate as it is based on a very approximate estimate of the average disturbance period. The calculation does indicate, however, that even relatively long period disturbances can increase the heat transfer rate significantly. It, therefore, appears probable that the increased heat transfer observed in the Apollo 14 data was caused by HFC unit and spacecraft vibrations.

In contrast to the Apollo 14 case, very little vibration appears to have occurred during the Apollo 17 experiments. Movement of the magnesium particles in the Lineal cell was tracked for selected periods of time. The magnesium particles showed much less variation in position than did the bubble in the Apollo 14 Zone cell. The magnesium particles, of course, were suspended in a moderately viscous fluid so they may not have responded to vibrations as easily as the bubble which was suspended in water. There are, however, several reasons for believing that the vibration levels were higher on Apollo 14 than on Apollo 17. First, astronaut movement was much more apparent during the Apollo 14 tests than during the Apollo 17 tests. Secondly, the Apollo 17 experiments were done while the craft was on its way to the moon; the Apollo 14 experiments were done on the way back from the moon. The masses of the two spacecrafts at the time of the HFC Experiments are as follows: Apollo 14, 12 091 kg (without LEM); Apollo 17, 46 587 kg (with LEM). Vibrations on Apollo 14, therefore, were much more easily transmitted than on Apollo 17. Also, the Apollo 17 data were obtained immediately after a spacecraft stabilization correction, whereas Apollo 14 data were obtained at a random time and during Apollo 14 it is suspected that the spacecraft was rolling and precessing.

From the computer program, a time-temperature curve was calculated assuming a g-jitter of $10^{-3} g_e$. This curve along with the Apollo 14 flight

curve and curves calculated on the assumption of a constant $g = 10^{-3} g_e$ and $g = 0$ are shown in Figure 26. It can be seen that the g-jitter curve falls somewhat below the constant g-curve, bringing it closer to the flight curve. The shape of the curve, however, still does not bend as the flight curves are observed to bend. An interesting aspect of the g-jitter curve, however, is that the curve is not actually as straight as is presented in Figure 26. A definite undulatory character is just becoming evident. One of the most striking features of the Apollo 14 data was the presence of long period oscillations in the time-temperature curves. It is concluded, therefore, that the observed convection in the Apollo 14 Radial Heating Experiment was caused by random spacecraft vibration. It is most probable that if precise vibration data, including not only g-jitter but also apparatus rotation oscillations, were available, a calculated time-temperature curve could duplicate the observed Apollo 14 curves.

4. Coupled Forces. The possibility that two or more forces can couple and therefore can either reinforce or annul convection was considered in the Flow Pattern Experiment. In that case the relevant driving forces for convection are surface tension and gravity. In the case of the Radial and Lineal cells, the following combinations are relevant:

- Gravity and thermal volumetric expansions.
- Gravity and random impulses.

a. Gravity and Thermal Volumetric Expansions. A computer analysis of the Apollo 14 case showed no significant convection as the result of coupled gravity and thermoacoustic forces as mentioned previously. With the aid of the computer program, however, it was possible to do a parametric study to find the g-level at which significant coupling would occur between gravity and thermal volumetric expansion forces. Figure 27 illustrates the results for a sample problem. Figure 27a shows the distance an isotherm would travel in 1 sec if the only form of heat transfer possible were conduction. Figure 27b shows the isotherms at 1 sec, assuming only thermoacoustic convection. In one-g, gravity forces are stronger and gravity completely determines the convective pattern (Fig. 27c). At $10^{-3} g_e$, gravity and thermoacoustic forces are comparable in magnitude, and it is at this g-level that coupling effects will be important for the conditions of heating, dimensions, and fluid properties used in the sample problem (Fig. 27d). It can be seen in Figure 27d that the coupling has the effect of bending the isotherms in such a manner as to increase the rate of advance at the top surface and decrease it at the bottom surface.

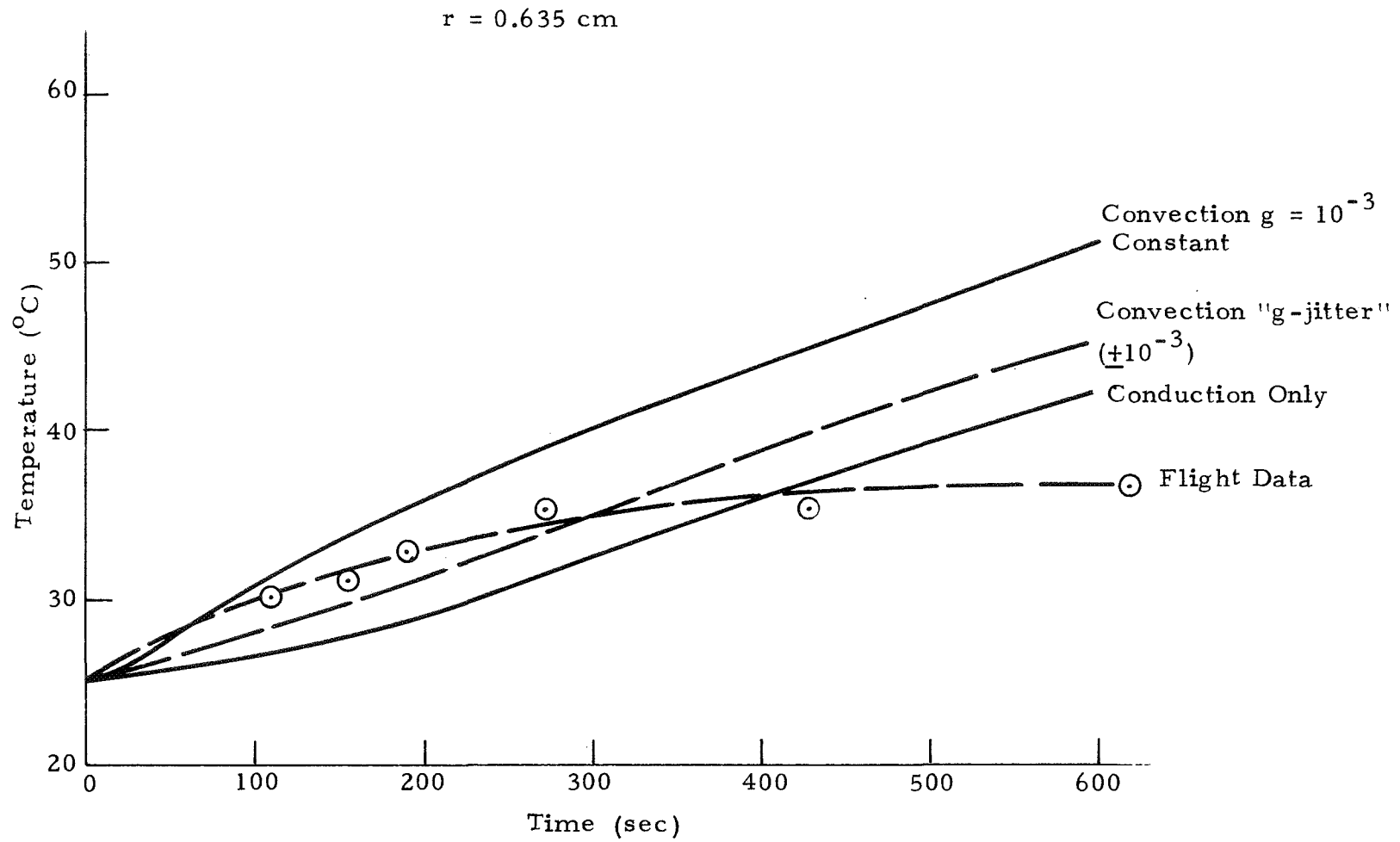
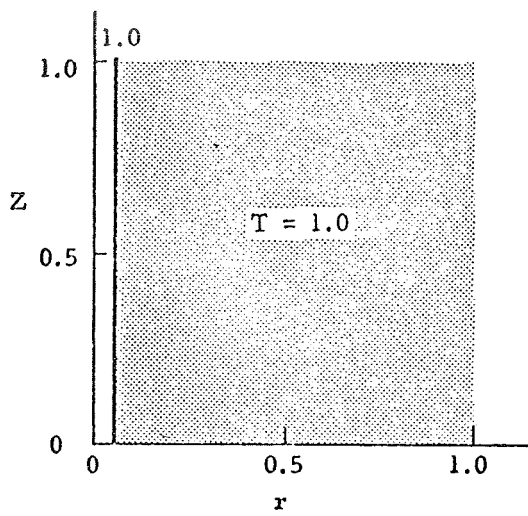


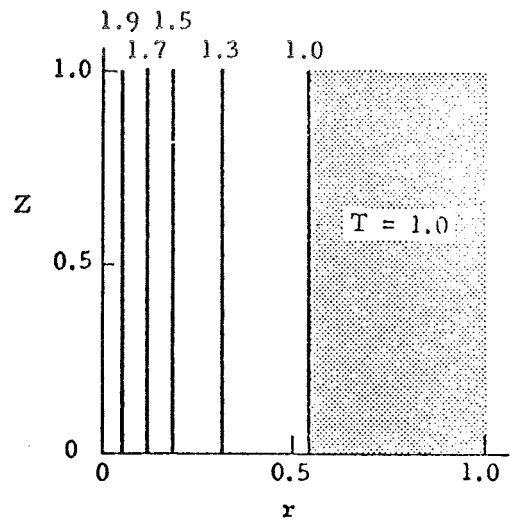
Figure 26. Comparison of calculated curves assuming various g-levels with Apollo 14 Radial cell data.

— Values of dimensionless temperature



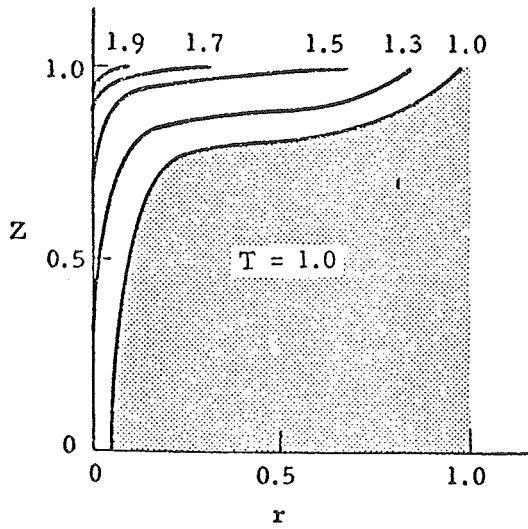
Conduction Only Solution

(A)



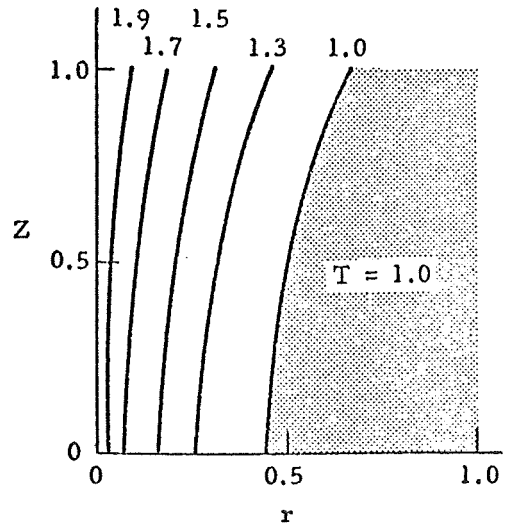
Solution with $g = 0$

(B)



Solution with $g = 1.0$ ($g's$)

(C)



Solution with $g = 10^{-3}$ ($g's$)

(D)

Figure 27. Isotherm plots for a cylinder problem demonstrating the coupling of gravity and thermal expansion convection.

b. Gravity and Random Impulses. The effect of steady mechanical vibrations for various frequencies and amplitudes on heat transfer in confined fluids was studied by Pak et al. [35]. Based on experimental data, the following correlation was developed:

$$\frac{Nu}{Nu_0} = 1 + 2.64 \frac{Re^{1.4} Pr^{0.6}}{Ra^{0.26} \Omega^{0.4}} + 0.004 \frac{Ac^{0.46}}{Ra^{0.21} \Omega^{0.1}},$$

where

Nu = Nusselt number with vibration

Nu_0 = Nusselt number without vibration

Re = Reynolds number based on motion of liquid relative to the surface

Ac = dimensionless vibratory acceleration

Ra = Rayleigh number

Ω = dimensionless frequency .

A plot of this relation versus Rayleigh number at a frequency of 120 Hz and a parameter of $G = 5$ is extrapolated to very low g-level Rayleigh numbers and is presented in Figure 28. The parameter G relates the amplitude and frequency of vibration of the base of the fluid container to the g-level of the environment. For the geometry of the container used by Pak et al., the fluid is water, the container base vibrates with a frequency of 120 Hz and an amplitude of 10^{-6} cm, the horizontal (to the g-direction) temperature gradient is 100°C , and g-level is 10^{-4} . Figure 28 predicts an increase in heat transfer of 460 percent over vibrationless heat transfer. These results indicate the gravity and vibration forces couple in an annulling manner; i. e., more heat is transferred by vibrations in the uncoupled case than in the coupled case.

The preceding discussion highlights the point that very little is known about coupling effects. In the case of vibrations, gravity apparently has a damping effect on vibration effects. In a low-g environment, therefore, vibrations will be much more of a problem than they are on earth.

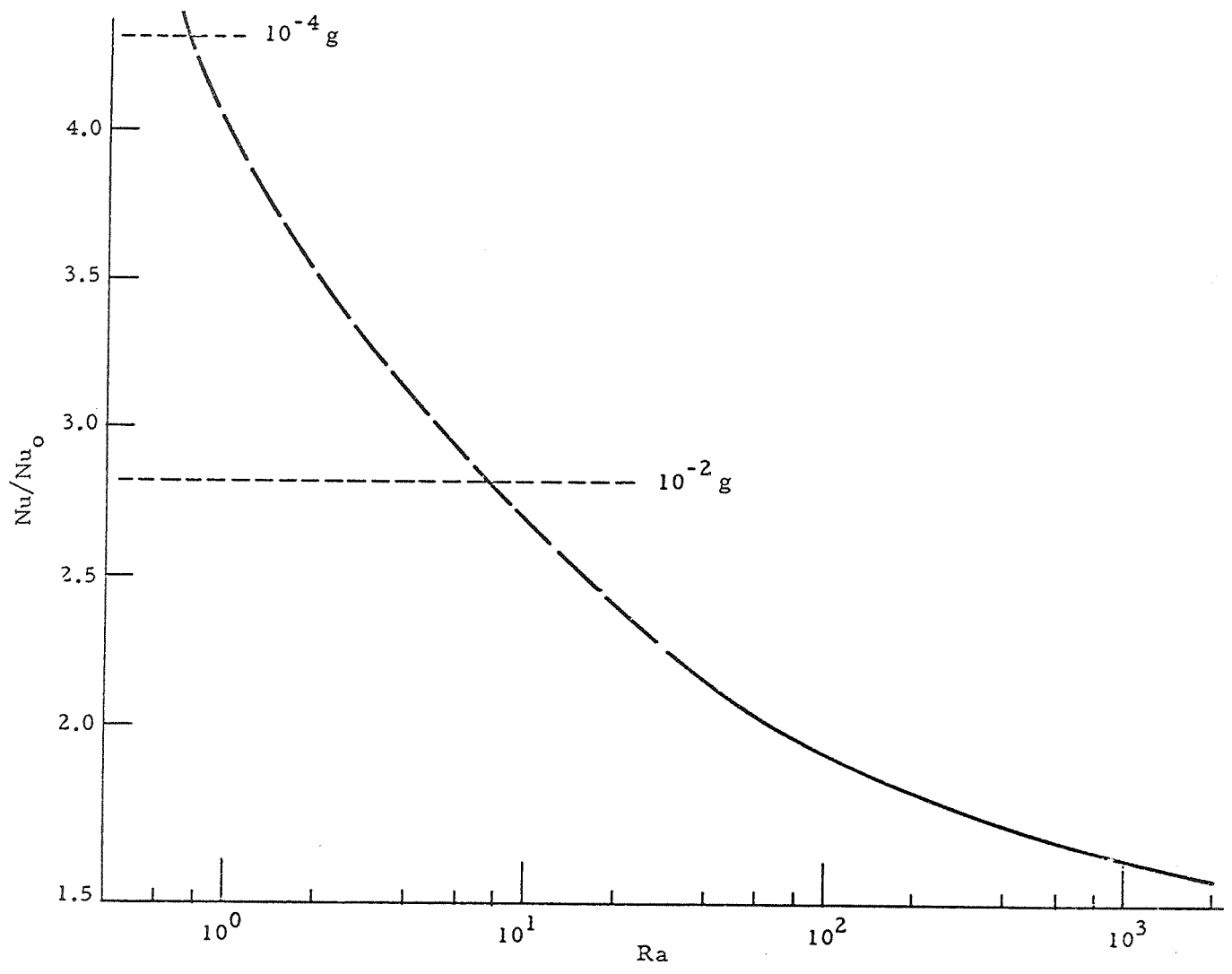


Figure 28. Attenuation of the effect of vibration with increasing values of Ra [34].

The agreement of the observed curves with the theoretical conduction-radiation curves shows that no significant convection occurred in the Lineal cell. The Apollo 17 Lineal Heating Experiment bears much the same relation to the Apollo 14 Zone Heating Experiment as the Apollo 17 Radial Heating Experiment does to the Apollo 14 Radial Heating Experiment. The conclusions regarding the observed Apollo 14 convection in the Zone cell, therefore, are the same as presented for the convection observed in the Apollo 14 Radial cell. (See Section IV. C.)

V. IMPLICATIONS FOR SPACE PROCESSING

As previously pointed out in the Introduction, convection studies in space are essential to establish the kinds and magnitudes of various forms of convection. Many types of convection have not been previously studied without the masking influence of terrestrial gravity forces. Also, the sensitivity of processes to convection in space will vary according to the boundary condition of each process during the fluid state. It is a well published fact (by Boger and Westwater and others) that small amounts of flow rapidly increase heat and mass transfer. In fact, in most instances the relationship is a power function. In any given process: (1) convection may be totally eliminated, (2) convection may be suppressed to a given degree, or (3) convection may be more controllable in space (some processes will actually utilize convection in space). The Apollo 17 Heat Flow and Convection Demonstration, along with the Apollo 14 Heat Flow and Convection Demonstration, has served as a first step toward generating previously nonexistent data necessary in defining the effects of convection in certain typical space processing type applications. The basic implications of the Heat Flow and Convection Demonstration Experiments for space processing are as follows:

1. Free surface experiments are highly susceptible to Marangoni convection.
2. Generally gravity-induced convection in confined fluids having low viscosity, low thermal gradients (less than about 10°C/cm), and 2- to 3-in. size containers is suppressed at $10^{-4} g_e$ or lower levels.
3. Gravity-induced convection in confined higher viscosity fluids is suppressed at gravity levels somewhat higher than $10^{-4} g_e$ ($\sim 10^{-3} g_e$).
4. Gravity-induced convection is suppressed at gravity levels of about $10^{-6} g_e$ in systems having larger thermal gradients (greater than about 10°C/cm) and/or having larger containers.
5. Low-gravity may lower the critical values for other types of convection; i. e., fluids in low-gravity will react more easily to surface tension forces and vibration forces.
6. In most cases, convection will be suppressed to some degree — an advantage for space processing.

7. Some space processes require laminar convection, and low-gravity may be used to reduce irregular or turbulent convection.

8. The effects of constant gravity levels and vibration (g-jitter) each affect fluids in space in a different manner.

9. More research is required on convection phenomena in space in support of the Space Processing Applications Program, especially in the areas of vibration, surface tension, thermosolutal convection, solidification, and electrohydrodynamic.

To elaborate further on each of the above, perhaps the most surprising discovery of the Apollo 17 Heat Flow and Convection Demonstration Experiment was the 18-sec onset time from initial heating for the Marangoni flow to occur in the Flow Pattern test. As previously discussed, this result was not expected. Theoretical work in this area led to the expectation that the onset times would be longer in space than on earth. The results, however, showed that vigorous convection appeared very quickly at only a few °C/cm (less than 10) in low-gravity. Many of the processes being planned for the Shuttle will employ free surfaces at elevated temperatures, meaning that even for $d\sigma/dt$'s that are an order of magnitude lower than Krytox, Marangoni convection can still be anticipated.

An interesting point brought out by Astronaut Ron Evans on the Flow Pattern test was that the visible surface remained "as smooth as a perfect lens" during the entire length of the test. With respect to space processing, this astute observation by Astronaut Evans is significant because it means that deformations of the free liquid surface large enough to be visible can apparently be avoided even though the fluid is undergoing vigorous thermal convection and contains a number of bubbles. The actual amount of microscopic surface deformation accompanying the observed convection remains to be defined in future studies. The formation of a spherical segment having a "nearly perfect shape" in zero gravity is very interesting, and possible applications have often been mentioned by others.

Concerning the second implication, the observed convection in the Apollo 14 Radial cell and lack thereof in the Apollo 17 Radial cell is attributed to vibrations in the spacecraft whose equivalent g-jitter level is on the order of 10^{-3} to $10^{-4} g_e$. Theoretical calculations show that significant convection occurs at these levels under the Apollo 14 and 17 boundary conditions whether or not the g is a constant steady value or a g-jitter.

The third implication follows directly from the above; i. e., more viscous fluids will raise the gravity level that can be tolerated without inducing convection. From dimensionless theory, the convection relationships to gravity (with all other factors constant) should be linear. Similarly, the fourth implication also comes from dimensionless analysis, as it can be shown that increasing the volume (same geometry) and/or increasing the thermal gradients will increase the requirements for lower gravity levels to suppress gravity-induced thermal convection.

The fifth implication is a very serious one because, at low-gravity levels, normally observed thresholds for convections may change because of other forces. This makes predicting convections caused by other forces very difficult. The evidence for this effect is indicated in the Flow Pattern results. Effects similar to this in other areas of convective coupling could play havoc to some space processing endeavors. Despite the importance of this fact, this is one area of convection where theory is sadly lacking and where there is a near dearth of knowledge on the new forms of convection that can occur in low-gravity. The situation here is quite serious.

On the brighter side, the point is made in the sixth implication that even though the convection situation is not perfect, it can generally be expected that thermal convection will be reduced in space, bringing an advantage to most processes. It is a fallacy to assume generally, however, that zero convection conditions will exist.

On the seventh implication, a fact that is often overlooked is that convection is necessary in many manufacturing processes on earth. This does not mean that none of them are candidates for space processing. In space it is very conceivable that convection can be much better controlled than it is on earth because undesirable coupling effects with gravity-induced convection can be eliminated. Forced convection processes in space appear to the authors to be an untapped area for study in space processing.

The eighth implication is a serious one. Vibrations drastically affect fluids. Some study has been made on the ground but extrapolation to low-gravity conditions is risky. More work is needed.

The ninth implication sums up the above to the conclusion that much more work is needed both on the ground and in space to develop a sufficient base of knowledge to elucidate the myriad of convection problems in space. As one can see, very serious problems exist in the area of convection, as shown in the subject experiments. Secondly, there are whole areas of convection yet unstudied in space. These include thermosolutal, electrohydrodynamic, interfacial, coupling with solidification, coupling with nucleation, and a host of other factors.

APPENDIX A

APOLLO 17 LIQUID CRYSTAL CALIBRATION STUDIES

Temperature data from the Apollo 17 HFC were obtained by using liquid crystal tapes. The tapes used and the general method of obtaining temperatures from the tapes have been discussed in the body of this report. This appendix will describe the techniques used to calibrate the liquid crystal tapes and discuss in some detail parameters which affect their color/temperature response.

Two types of flight data were obtained: dynamic and isothermal. In the calibration procedures an additional type was obtained. This has been called equilibrium gradient data. These three types are defined as follows:

- Dynamic — A color band moves indicating a moving temperature isotherm.
- Isothermal — The entire liquid crystal tape is at a uniform temperature and therefore a uniform color.
- Equilibrium Gradient — A color band is stationary indicating a stationary temperature isotherm.

It is essential to distinguish between the three because of the difference in an observer's ability to determine colors in each case, the difference in the number of distinguishable colors in each mode, and the varying degree each is affected by the parameters to be discussed in this appendix.

The liquid crystal tapes were calibrated according to the procedures described in Reference 9. Briefly, these procedures involved two basic types of apparatuses: one type used for isothermal tests and the other for dynamic and equilibrium gradient tests. The essential difference between the two is the positioning of the liquid crystal tape with respect to the heater. In the isothermal tests the tape was placed directly over the heater to give uniform heating; in the dynamic tests the tape was placed to one side of the heater to give a gradient in the crystal tape. This is illustrated in Figure A-1.

The procedure followed in both the isothermal and dynamic calibrations consisted of turning on the heater and observing the temperature of color changes both directly and with motion pictures.

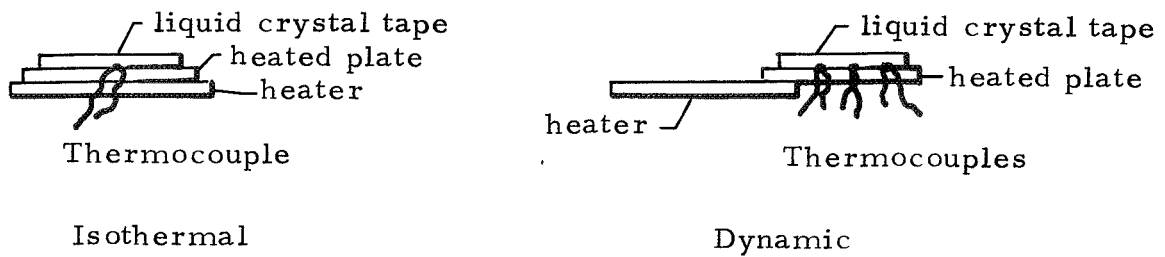


Figure A-1. Illustration of basic isothermal and dynamic concepts.

In all calibrations the following sources of error were evaluated:

- Instrument Errors
 - Thermocouple Attachment and Insulation
 - Thermocouple Errors (Heat Loss, Time Lags)
 - Reference Junction
 - Voltmeter
 - Heater Configuration and Insulation
- Aging (Light, Air, Time)
- Dynamic versus Isothermal
- Different Observers' Sensitivity
- Observation Technique (Filmed versus Direct)
- Initial Temperatures
- Heating Rates
- Heating versus Cooling
- Previous Thermal History
- Lighting
- Angle of Viewing
- Pressure and Gravity Effects

Instrument errors were found to be most significant.

Seven liquid crystal ranges were calibrated both dynamically and in an equilibrium gradient. The final temperature values assigned to the various colors are given below.

Dynamic Temperatures							
Crystal Color	D	E	F	G	H	I	J
Amber	24.7	26.9	30.0	32.0	36.3	35.7	42.6
Green	26.5	28.6	31.8	33.5	37.4	37.8	44.7
Blue	28.8	30.7	34.5	35.1	39.0	41.0	47.3

The results of the isothermal tests for the crystal tapes used to determine initial and ambient temperatures for the HFC experiments are as follows:

Isothermal Temperatures						
Crystal Color	C		D		E	
	Value	Precision	Value	Precision	Value	Precision
Brown	22.9	±0.4	24.6	±0.3	27.0	±0.5
Amber	23.4	±0.2	25.5	±0.4	27.5	±0.6
Yellow Green	23.8	±0.2	26.2	±0.2	28.1	±0.4
Green	24.2	±0.3	26.8	±0.3	28.7	±0.5
Blue Green	24.6	±0.2	28.2	±0.6	29.5	±0.5
Dark Blue Green	25.0	±0.2	28.7	±0.5	30.1	±0.6
Blue	25.4	±0.2	29.6	±0.4	30.7	±0.7
Dark Blue	25.8	±0.3	30.5	±0.6	31.4	±0.8

In the following, the means of ascertaining the magnitudes of the various errors and the means used to correct for them are discussed.

A. Instrument Errors

The basic components used in all the tests are shown in Figure A-2.

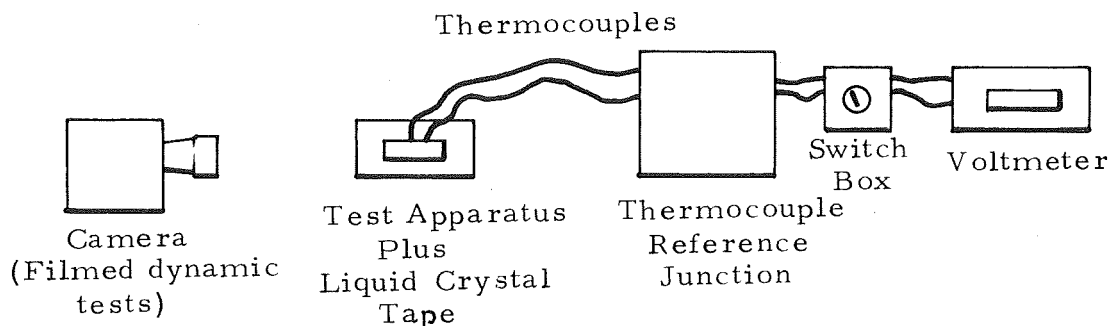
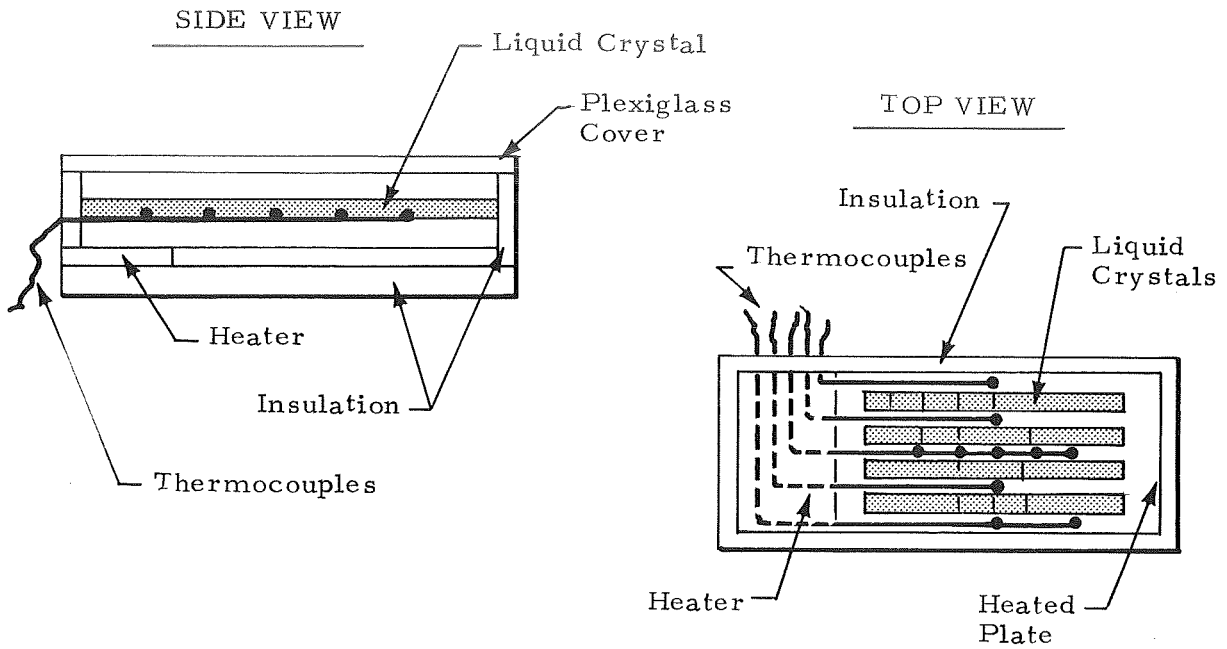


Figure A-2. Schematic of basic calibration apparatus.

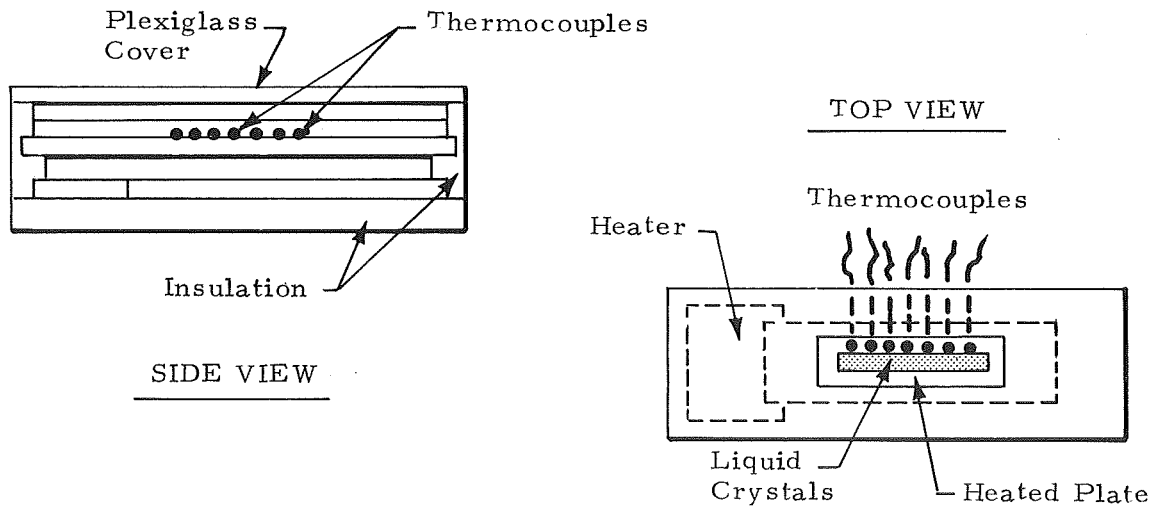
For each test apparatus using different thermocouples, the entire setup was calibrated by inserting the thermocouples into an ice bath made with distilled water. At 0°C the greatest overall systematic error was 0.6°C . However, this error was easily corrected.

The isothermal tests performed on two different apparatuses are in agreement. However, the two apparatuses used for the equilibrium gradient tests consistently gave differing results indicating an unknown source of systematic error. Figures A-3a and A-3b show a diagram of the two equilibrium gradient test setups. The first is the same apparatus as used in the Apollo 14 calibrations and the second is called the Apollo 17 setup. The Apollo 17 apparatus was also used for the dynamic calibrations.

The same reference junction and voltmeter were used in each case. In both apparatuses iron/constantan thermocouples were used. However, these were attached to the heater plate differently (Fig. A-4).

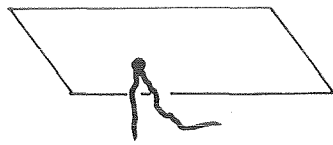


a. Apollo 14 apparatus.

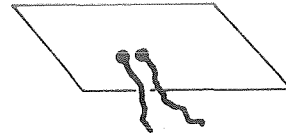


b. Apollo 17 apparatus.

Figure A-3. Diagram of the two dynamic test apparatuses used.



Apollo 14 Apparatus



Apollo 17 Apparatus

Figure A-4. Method of thermocouple attachment.

A test was conducted to determine the magnitude of any error produced using these different techniques of thermocouple attachment. The results indicate that the two techniques give the same color/temperature response.

Using Crystal H

Thermocouples Attached By	Amber	Green	Blue
Apollo 14 Method	34.8 ±0.3	35.4 ±0.4	36.3 ±0.7
Apollo 17 Method	34.7 ±0.3	35.8 ±0.4	36.9 ±0.7

The effect of insulation was checked by operating the Apollo 17 apparatus with and without insulating material. Again, this factor showed little, if any, effect.

Using Crystal G

	Amber	Green	Blue
With Insulation	31.0 ±0.2	31.9 ±0.3	33.4 ±0.3
Without Insulation	31.5 ±0.2	32.6 ±0.4	33.8 ±0.3

Yet the two sets of equilibrium gradient test data from the two apparatuses do not agree in two cases. This is illustrated in the following table.

Using Crystal J

Apparatus	Amber	Green	Blue
Apollo 14	42.7 ±0.4	45.0 ±0.8	48.7 ±0.7
Apollo 17	40.8 ±0.4	43.0 ±0.4	46.3 ±0.9

It is concluded that some undetermined systematic error is involved. An average of these two tests is used for the final values of the crystal's color/temperature response.

B. Aging

Aging of liquid crystals has the effect of slightly shifting the temperature range of the crystal. For instance, a crystal tape which initially changes from amber to blue in the range of 30 to 35° C may shift to a range of 28 to 33° C because of aging. During Apollo 14 studies, several factors were considered, and the aging was attributed to light exposure. On Apollo 17 procedures to prevent excessive exposure to light were carried out. In order to determine the correct color/temperature response of the Apollo 17 HFC liquid crystals at the time of the flight, a series of aging studies was conducted. These studies were isothermal tests.

The method used for the tests was basically very simple. Samples of each liquid crystal were heated uniformly on a plate. As color changes were noted, the temperature of the plate was recorded.

In October 1972 (Test I), each crystal tape was calibrated. In April 1973 (Test II), these same tapes were recalibrated having been kept in the laboratory in a sealed container. Additionally, two tabs containing segments of the same liquid crystals were mounted in the flight experiment. One of these (the ATP Tab) was removed before launch and the other (the Flight Tab) was returned by the astronauts in a sealed envelope after performing the experiment. These two tabs were also calibrated (ATP Tab, Test III; Flight Tab, Test IV). By comparing results from these tests, the condition of the crystals at the time of operation could be determined.

Two different apparatuses were used: one for the laboratory samples and another for the ATP and Flight Tabs. The two setups were essentially the same except for the size of the heater plate. A larger plate was needed to accommodate the tabs. Figures A-5 and A-6 show the two setups.

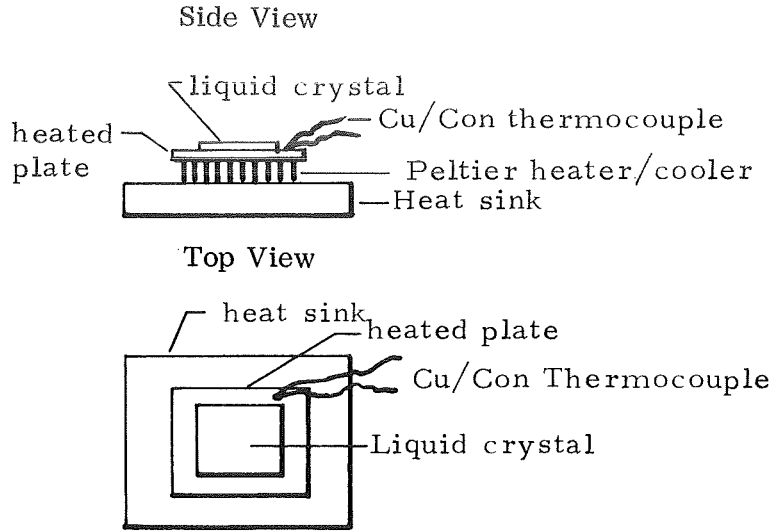


Figure A-5. Isothermal apparatus, Tests I and II.

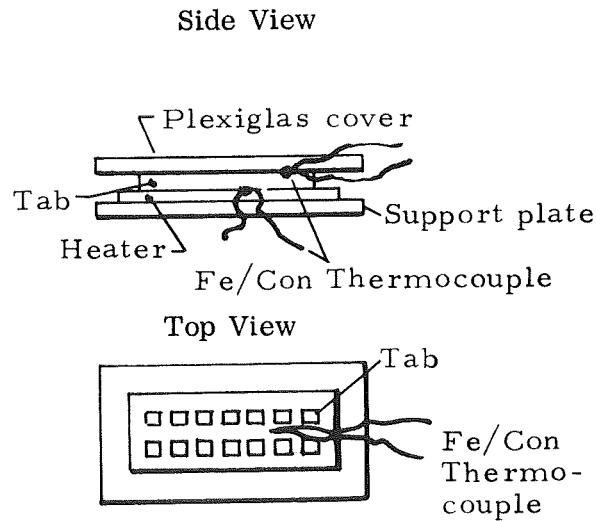


Figure A-6. Isothermal apparatus, Tests III and IV.

Although the heating method and type of thermocouples were different between the two series of tests, the technique used was the same: the thermocouples were calibrated, the liquid crystals were cooled to a point below their indicating range, heat was applied so that the crystals slowly changed colors,

and the temperatures at which these colors appeared were recorded. Each crystal strip was observed several times to get an indication of the precision of the determination. For the laboratory strips only one thermocouple was used. However, the ATP and Flight Tabs consisted of crystal strips sandwiched between two thin (2.0 mil) Teflon films, so that one thermocouple was placed under the tab and another on top of the tab and an average was used to indicate the temperature of the liquid crystal inside the "sandwich."

The apparatus shown in Figure A-5 was used in October 1972 on samples of crystals from which the flight crystals were taken and again in April 1973 on the same crystal strips which had not been exposed to light. The results of the two tests indicate slight, if any, change because of aging (not associated with light). Therefore, these two sets of data were treated as one to give values for the isothermal testing on the control samples.

The results for the ATP Tab give values for the crystals prior to launch, and the Flight Tab gives results for the time at which the experiment was performed. (When each of these tabs was removed from the unit, it was kept sealed to assure that no light degradation could take place. Since the October/April tests show no other aging effect, any differences between the tabs and the control samples would be because of a difference in exposure to light.)

A number of tests were conducted on each crystal with the conclusion that no significant aging effects occurred by flight time. The following table shows the results of these tests for Crystal K.

Color \ Test	Tests I and II	Test III	Test IV
Brown	20.0 ±0.4	20.2 ±0.1	20.5 ±0.1
Amber	20.6 ±0.4	20.9 ±0.1	21.1 ±0.1
Yellow Green	20.9 ±0.3	21.2 ±0.1	21.5 ±0.1
Green	21.3 ±0.2	21.7 ±0.1	21.9 ±0.1
Blue Green	21.8 ±0.2	22.3 ±0.1	22.6 ±0.2
Dark Blue Green	22.1 ±0.2	22.7 ±0.1	23.0 ±0.4
Blue	22.4 ±0.2	23.0 ±0.2	23.2 ±0.2
Dark Blue	22.7 ±0.3	23.3 ±0.2	23.6 ±0.2

It can be seen that within the error bands of each test, the values are in good agreement.

C. Dynamic versus Isothermal

As was mentioned previously, two types of liquid crystal data were obtained from the Heat Flow and Convection Experiment. These have been called "dynamic" and "isothermal." The difference between the two does not result in an actual shift in temperature range of the liquid crystal as with aging, but it may influence the observed color for a given temperature. In the isothermal case, as many as eight changes in color can be seen; however, in the dynamic or gradient case only three distinct color bands can be seen accurately, and it is not always possible to make a direct relationship between the two cases. That is, what is called green in a dynamic situation may correspond to the color called yellow-green in an isothermal situation, or it may correspond to green or blue-green. The following table lists the colors observed for dynamic and isothermal cases and also indicates which liquid crystals were used in the HFC Experiment in each case.

Isothermal Colors	Crystals Used	Dynamic Colors	Crystals Used
Brown	A		D
Amber	B	Amber	E
Yellow Green	C	Green	F
Green	D	Blue	G
Blue Green	E		H
Dark Blue Green	K		I
Blue			J
Dark Blue			

Although there is a subjective difference in the colors seen in each mode, any given reader is relatively consistent in determining a color change in either case. Because of this subjective distinguishing of colors in the two different modes of operation, the crystals were calibrated both isothermally and dynamically.

Results from the isothermal tests were used to give initial temperatures for each run of the HFC Experiment; and the results of the dynamic tests were used for the data obtained during each run.

D. Different Observers' Sensitivity and Observation Techniques

A human observer was used rather than an instrument, such as an optical densitometer, to determine colors in the liquid crystals because such instrumentation is costly and time consuming to operate considering the number of data points to be observed. However, response to color changes is not necessarily the same from individual to individual. What one person calls green, another might call yellow-green. Therefore, the individual who determines color position must either be the same for all tests or another person must be "calibrated" against the first. Since the person who read the data (color position versus time) from the flight film was not available for the entire liquid crystal calibration procedures, a method to correlate other readers' results was developed. Additionally, this technique assured that there was no color bias because of filmed versus direct (observed in the laboratory) data.

A series of 16-mm movie films was made showing temperature versus color response of the seven liquid crystals used for the dynamic flight data. The apparatus shown in Figure A-3b (Apollo 17 apparatus) was used for making these films. The general procedure was basically as follows. Heat was applied to one end of the crystal strip and 16-mm movies were made as the color bands moved across the strip. The temperature was recorded as each color band crossed each of seven thermocouples. Thus, a temperature for the leading edge of each color was determined. These data were obtained from the films by Reader I (the individual who read the flight data film). The same test apparatus and procedure was used and read directly by Reader II in the laboratory. Thus, a baseline for comparison of the data as obtained by the two readers was established. Any further tests read by Reader II could then be correlated to what Reader I would have observed.

E. Initial Temperature and Heating Rates

It was found that initial temperature has a slight effect on the color response of the liquid crystals. A crystal tape which was heated from room temperature through its temperature range gave the following results: amber = 40.2° C; green = 41.6° C; and blue = 44.5° C. The same crystal heated from 38° C gave: amber = 39.5° C; green = 40.5° C; and blue = 43.9° C. This effect appears to be most pronounced when results of tests which start well below the response range are compared with ones starting approximately 1 to 2° C below the response range. This is illustrated in Figure A-7. When the color bands are allowed to come to equilibrium (as in the equilibrium gradient tests), this effect is not noticeable.

In the dynamic tests the rate of heating (or more correctly the rate of color band movement) has an effect on the observed temperature response.

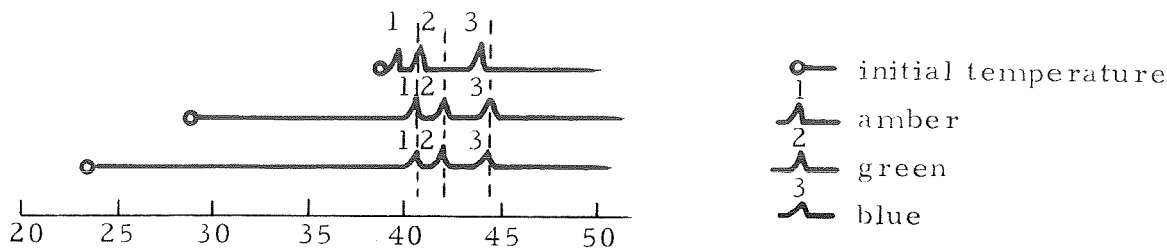


Figure A-7. Illustration of effect of initial temperature.

Whether this is the result of the thermal response of the thermocouples, the apparatus, or the liquid crystals themselves was not determined. However, a higher heating rate gives an apparent lower temperature for any color. Tests were made using a high heating rate (5.4 W), a low heating rate (1.9 W), and an equilibrium gradient (in other words, the color bands were stationary, or there was a "zero-velocity gradient").

Both the high and low heating rate tests were performed using the Apollo 17 apparatus shown in Figure A-3b. The liquid crystal tapes were attached to a 0.08-cm stainless steel plate which was heated by a thermofoil heater. The plate was instrumented with thermocouples which were along the axis and to the side of the crystal tape. The entire apparatus was completely insulated with a small cutout so that the liquid crystal and thermocouples were visible. A piece of plexiglas was clamped over this cutout to reduce heat losses. The temperature at the thermocouple was recorded as the color bands were observed to pass the thermocouple position. The average of as many as 16 data points was used for each color on each crystal. Values were obtained for the two heating rates (which gave different color band velocities).

It was necessary to obtain a set of equilibrium gradient calibrations for the liquid crystal tapes used in space, since the velocity of the color bands was considerably faster in the dynamic calibrations than in the flight test unit. The calibration technique used in this study consisted of recording, by means of color photographs, the color changes of liquid crystal tapes attached to an instrumented metal plate heated at one end. The schematic shown in Figure A-3a gives the general features of the calibration apparatus. (Equilibrium gradient tests made using the apparatus in Figure A-3b were for investigating instrument errors only. Any results reported as "Equilibrium Gradient" were made using the Apollo 14 apparatus.) The metal plate to which the liquid crystals were attached was a strip of 0.08-cm thick stainless steel with 10 thermocouples welded at the indicated locations. A small thermofoil heater was

attached to supply heat to the left edge of the liquid crystal tapes which were taken from the same lot as the flight tapes. The metal plate was then completely insulated to minimize heat losses. The area where the liquid crystals and thermocouples were located was cut away, and a transparent plastic viewing port was installed permitting both visual and photographic observation.

Photography of the color changes was accomplished using a 35-mm camera under lighting conditions which simulated the lighting during flight. With the described calibration apparatus, temperature profiles along the plate were plotted for each photograph (set of data points). As many as 12 sets of data points were taken at 6 different power settings for tapes C, D, E, and F; and as many as 8 sets of data points were taken at 5 different power settings for tapes G, H, I, and J.

The final values given for each crystal take these results into account and are given for a color band velocity approaching that experienced by the tapes in the flight experiment.

The following table shows the results of these tests for Crystal H.

Conditions	Amber	Green	Blue
High Heating	32.7	33.6	35.2
Low Heating	34.1	34.8	36.0
Equilibrium Gradient	36.1	37.4	38.9

F. Heating versus Cooling

This effect is similar to that of initial temperature. On heating, the temperature values of amber, green, and blue do not always agree with those observed on cooling. Although this effect is not a factor in the Apollo 17 flight data since only heating data were used in the analysis, results of the equilibrium gradient tests performed for both heating and cooling indicate that no apparent hysteresis is involved when equilibrium is reached.

G. Previous Thermal History

Although this effect has been reported by some investigators, no evidence was found in these calibration studies to indicate that this factor influenced the crystals used. The tapes appeared to give consistent results after as many as 10 heating and cooling cycles.

H. Lighting

Because the color observed is a result of scattering of incident light, lighting can be a strong influence. For instance, as an extreme case, if no green light were present in the incident light, no green would be seen in the liquid crystals. However, the same type lighting (a known combination of incandescent plus fluorescent) was used for all tests so that this effect was greatly minimized, if not eliminated.

I. Angle of Viewing

Again, in the extreme, this effect can be an influence on the observed colors. However, an angle of approximately 30 deg is needed before any noticeable difference in color is observed [36]. All tests were conducted at a maximum 15-deg viewing angle, and generally it was much less. Thus, this source of error was eliminated.

J. Pressure and Gravity Effects

Although there are liquid crystals which are pressure sensitive (nematic liquid crystals), the cholesteric type used for these experiments are not sensitive to pressure changes. The possibility of a direct gravity effect on the color/temperature response was investigated. The tapes were tested in a KC-135 aircraft flight, and no effects of the varying g-levels experienced were observable.

K. Assignment of Error Bands

The standard deviation was calculated for each series of tests. As many as 70 points were used to obtain this measure of precision of the data. Thus, each data point is the average of several, and an error band, associated with reader error and other random errors, is calculated for each as follows:

$$\Sigma = \pm \sqrt{\frac{\epsilon (x - x_{avg})^2}{n - 1}} .$$

The error bands assigned to each value in the tables are a measure of the precision for the data. Because of the influences of possible unaccountable effects such as initial temperature, instrument errors, resolution of the film used for the flight data, and other parameters as have been discussed previously, it was not possible to assign a final error band for the accuracy.

However, since an average of two separate tests was used for the final values, these are more accurate than any individual test.

L. Final Values of Color versus Temperature

The following table gives the temperature values and precision values for a given color for each crystal used dynamically for the flight data. The first column gives data, corrected for reader differences, for heating rates higher than those on flight and a different initial temperature. The second column gives similar data for the equilibrium gradient tests which are not dependent on initial temperature or heating rate. The third column is an average of the two and represents the final values of temperature and precision assigned to the colors of the crystals.

Crystal	Color	1	2	3 (Final Values)
D	Amber	24.7 ±0.2° C	24.7 ±0.2° C	24.7 ±0.2° C
	Green	26.0 ±0.3° C	26.9 ±0.3° C	26.5 ±0.3° C
	Blue	28.6 ±0.6° C	29.0 ±0.3° C	28.8 ±0.6° C
E	Amber	26.8 ±0.8° C	27.0 ±0.4° C	26.9 ±0.8° C
	Green	28.5 ±0.5° C	28.6 ±0.2° C	28.6 ±0.5° C
	Blue	30.7 ±0.6° C	30.6 ±0.3° C	30.7 ±0.6° C
F	Amber	29.5 ±0.4° C	30.6 ±0.3° C	30.0 ±0.4° C
	Green	30.6 ±0.5° C	33.0 ±0.6° C	31.8 ±0.5° C
	Blue	33.3 ±0.8° C	35.7 ±0.3° C	34.5 ±0.8° C
G	Amber	31.4 ±0.9° C	32.5 ±0.2° C	32.0 ±0.9° C
	Green	33.0 ±0.6° C	33.9 ±0.4° C	33.5 ±0.6° C
	Blue	34.7 ±0.8° C	35.4 ±0.7° C	35.1 ±0.8° C
H	Amber	36.5 ±0.3° C	36.1 ±0.2° C	36.3 ±0.3° C
	Green	37.4 ±0.4° C	37.4 ±0.2° C	37.4 ±0.4° C
	Blue	39.1 ±0.7° C	38.9 ±0.4° C	39.0 ±0.7° C
I	Amber	35.4 ±0.2° C	36.0 ±0.2° C	35.7 ±0.2° C
	Green	37.2 ±0.2° C	38.4 ±0.2° C	37.8 ±0.2° C
	Blue	39.8 ±0.4° C	42.2 ±0.6° C	41.0 ±0.4° C
J	Amber	42.5 ±0.4° C	42.7 ±0.4° C	42.6 ±0.4° C
	Green	44.3 ±0.4° C	45.0 ±0.8° C	44.7 ±0.4° C
	Blue	46.4 ±0.9° C	48.1 ±0.7° C	47.3 ±0.9° C

APPENDIX B

UTILITY AND DEFINITION OF PERTINENT DIMENSIONLESS NUMBERS

In the context of this report, dimensionless parameters, such as the Rayleigh and Marangoni numbers, may be thought of as ratios of physical forces. Thus when a particular ratio is $\gg 1$, the force associated with the numerator dominates that of the denominator, and vice versa when the ratio is $\ll 1$. In certain well studied problems, critical values exist for these dimensionless parameters (ratios) such that a change of state occurs as the critical value is exceeded and one force overcomes the other.

The likelihood of natural convection arising in a fluid and its order of magnitude if it does occur can be estimated for buoyancy (gravity) induced conditions by examining a dimensionless parameter called the Rayleigh number (Ra). A similar analysis can be applied for surface tension-induced motion in fluids with free surfaces by examining a dimensionless parameter termed the Marangoni number (Ma). These numbers are defined by

$$\text{Ra} = \frac{-g\beta\Delta TL^3}{\nu\alpha}$$

$$\text{Ma} = \frac{\left(\frac{d\sigma}{dT}\right)\Delta TL}{\mu\alpha},$$

where

- g = gravity
- β = thermal expansion coefficient
- ΔT = temperature difference across the fluid
- L = depth or width of the fluid
- σ = surface tension
- μ = absolute viscosity
- ν = kinematic viscosity
- α = thermal diffusivity .

The Rayleigh number is, therefore, the weighted ratio of the buoyancy force to the viscous force, whereas the Marangoni number is the corresponding ratio of surface tension to viscous force. In each number, the numerator contains the driving force with the denominator representing the restraining force. Thus the tendency for achieving sustained convective motion is greater as the numbers increase. As they surpass their critical values, the driving forces overcome viscous restraining forces and a change in flow occurs; i. e., a transition from no-flow to laminar convection or from laminar to turbulent convection occurs.

The ratio of Ra and Ma to their respective critical values (Ra_c and Ma_c), which are determined by geometry, type of containment and direction of heating, determines the onset and magnitude of fluid flow. If either Ra/Ra_c or Ma/Ma_c exceed unity, flow will occur and heat transfer through the fluid increases because the convective heating is superposed to the conductive and radiative modes existing before flow initiates. As these ratios increase, the magnitude (velocity) of flow increases until turbulence finally occurs and the amount of convective heat transfer also increases. Normally this relation is linear on a log-log plot in a given regime. When heating from the side in a gravity field, for example, the critical Rayleigh number is shown to be zero from theoretical considerations [31]. Experimental results have shown, however, that a certain finite critical condition must be exceeded before heat transfer is increased over that of conduction and radiation [32]. Upon heating from below, the liquid layer remains stable to fluid flow as well as convective heat transfer until a relatively large critical condition is exceeded. For a liquid layer bounded on bottom with a solid wall (heating element) and on top with a free surface, Ra_c is approximately 1100 [20].

The preceding quantities, Ma_c and Ra_c , are dependent on such properties of the fluid and container as the Prandtl number, Biot number, aspect ratio, heater versus fluid thermal conductivity, sidewall thermal conditions, and surface deformability (crispation and Bond numbers). The Prandtl, Biot, and Bond numbers are dimensionless ratios which often appear in many other engineering problems. The aspect ratio is a measure of the geometrical symmetry of the fluid container, and as such it also appears frequently in many engineering problems. The crispation group appears less frequently and is utilized in the study of capillary waves. The definition and utility of each of these dimensionless numbers are discussed below.

The Prandtl number represents the ratio of a fluid's momentum diffusivity to its thermal diffusivity and is defined by

$$\text{Pr} = \frac{C_p \mu}{k} ,$$

where

k = thermal conductivity

Pr = Prandtl number

C_p = heat capacity at constant pressure.

Thus, fluids with a very large Prandtl number ($\text{Pr} \gg 1$), such as Krytox oils, dissipate heat much slower than momentum. In determining the value of the critical Rayleigh number, the Prandtl number has little or no effect unless $\text{Pr} \leq 1$ in which case Ra_c increases as Pr decreases [37].

The Bond number is utilized often in such problems as capillary flow, sloshing, and rippling. It compares the relative magnitudes of gravitational and capillary forces and is defined as

$$\text{Bo} = \frac{(\rho_L - \rho_G) V^2 L}{\sigma} ,$$

where

Bo = Bond number

ρ_L = liquid density

ρ_G = vapor density

V = liquid velocity.

It is the pertinent parameter delineating capillary-dominated and gravity-dominated surface waves. At very low Bond numbers, "gravity" waves are relatively unimportant. The presence of such "gravity" waves at a free surface tends to stabilize surface tension-driven convection [17]. For the Apollo 17 Flow Pattern Experiment, $\text{Bo} < 10^{-4}$, and one can safely neglect the effect of gravity waves on convection onset.

The Biot number can be considered as the ratio of the heat transferred to the surroundings at the vapor-liquid interface over the heat transported by conduction within the liquid. It is given by the following relation,

$$\text{Bi} = \frac{hL}{k} \quad ,$$

where

$$\begin{aligned} \text{Bi} &= \text{Biot number} \\ h &= \text{convective heat transfer coefficient.} \end{aligned}$$

In natural convection studies involving a free surface, the Biot number indicates whether the vapor surrounding the liquid of interest is thermally insulating or conducting. An insulating vapor decreases stability; i. e., Ra_c and Ma_c are lower for smaller Biot numbers [20, 14, 15, 38].

The crispation number was introduced by Scriven and Sternling [16] in their study of surface tension-driven convection of liquid layers and is given by

$$\text{Cr} = \frac{\mu\alpha}{\sigma L} \quad ,$$

where

$$\begin{aligned} \text{Cr} &= \text{Crispation number} \\ \mu &= \text{absolute viscosity.} \end{aligned}$$

Using linear theory, Smith [17] showed that surface deformations due to flow perturbations have negligible effects on convection onset and cell size if $\text{Cr} < 10^{-3}$. This condition was satisfied for Apollo 17 as $\text{Cr} \cong 4 \times 10^{-5}$.

Although not formally considered to be a "nondimensional number," the aspect ratio is certainly dimensionless and arises often in studies in which geometrical similitude is important. It is also an important parameter in natural convection studies, both gravity and surface tension driven. The aspect ratio can be defined as the container width divided by the container height [19]. The critical Marangoni and Rayleigh numbers usually increase as the aspect ratio decreases (narrower containers).

As mentioned earlier, the dimensionless ratios of thermal conductivities (sidewall to fluid and heater to fluid) are also important parameters in convection problems. Insulating container walls (and heaters) are more unstable than conducting ones. In other words, sidewalls and/or heaters which are better conductors than the fluid layer enhance stability (they raise Ra_c), while materials of lower conductivity lower the criticality conditions [20, 38].

The preceding discussions have demonstrated the utility of dimensionless numbers for describing certain fluid flow phenomena. It was noted that these numbers are extremely useful in well studied problems where ranges in their values have been identified with flow regimes. In other less studied problems, the state of the art of nondimensional numbers is at a very primitive stage and their use is of limited value. Such a case is well represented by thermoacoustic convection. This problem will not yield a pertinent dimensionless parameter from inspection of the equations as in other problems [39, 40]. Thus, the pertinent dimensionless parameter can only be determined by mathematical modeling (numerical solution) or experimental studies. Furthermore a criticality condition will be even more difficult to define since the wavelike phenomena are present, although negligible, at even the slightest heating rates.³

In conclusion, nondimensional numbers can be used as a powerful tool in the scientific analysis of most buoyancy-driven, natural convection problems (with constant g -levels) and in simple cases of surface tension-driven natural convection. It is also very helpful when these two forces are coupled. Their use in such problems as thermoacoustic, g -jitter, vibrational, electrohydrodynamic, and solidification-induced natural convection is very limited even when one of these is coupled with gravity or Marangoni convection. Only more basic research and experimental studies made without the encumbrance of terrestrial gravity can alleviate this situation.

3. Private Communication with S. W. Churchill on April 26, 1973.

APPENDIX C

ERROR ANALYSES FOR RADIAL AND LINEAL EXPERIMENTS

A. Liquid Crystal Calibration Errors

The technique of thermally mapping convective heat flow with liquid crystals was first explored in the Apollo 14 Heat Flow and Convection Demonstration Experiments [9]. Because the technique is new, however, the question is raised in the present study of whether all sources of systematic error were truly eliminated in the calibration runs of both the Apollo 14 and Apollo 17 liquid crystals. To account for the differences observed in the data of Apollo 14 and Apollo 17 on the basis of calibration error, four possibilities need to be considered:

1. Calibration errors were insignificant for the Apollo 14 data.
2. Calibration errors were significant for the Apollo 14 data.
3. Calibration errors were insignificant for the Apollo 17 data.
4. Calibration errors were significant for the Apollo 17 data.

Combining these possibilities leads to four further possibilities: 1-3, 1-4, 2-3, and 2-4, of which only 1-4 and 2-3 should concern us here. The condition 1-3 means, of course, that the data presented in Figures 16 and 17 and 19 and 20 are accurate to within the precision limits indicated. The condition 2-4 could only mean that convection did not occur during the Apollo 14 flight test and did occur during the Apollo 17 flight test. Such a situation would mean that the calibration errors made in the Apollo 14 study were opposite in direction to those made during the Apollo 17 study, a very unlikely situation.

If the case 1-4 obtains, then convection must have occurred during the Apollo 17 flight test as well as during the Apollo 14 flight test. The calibration data for the Apollo 17 crystals, therefore, must have been in error in such a manner as to make the temperatures obtained from the lower temperature tapes appear lower than they actually were and the temperatures obtained from the higher temperature tapes appear higher than they actually were. In the event that case 2-3 obtains, then convection was not present during either the Apollo 14 or 17 flight tests. In such a case the Apollo 14 calibration errors must

have been such as to make the temperatures obtained from the lower temperature tapes higher than they actually were and those obtained from the higher temperature tapes lower than they actually were. Thus, if either of the latter two cases (i. e. , 1-4 or 2-3) obtains, then the calibration errors had opposite directions in the lower and higher temperature ranges.

Rather extensive calibration studies were conducted during the Apollo 17 data analyses, and these are detailed in Appendix A. In these more extensive studies, no source of error could be located that raised or lowered the temperatures from the low temperature tapes while lowering or raising at the same time the temperatures from the higher temperature tapes. All the errors that were located had the effect of lowering or raising the temperatures on all of the tapes. It is concluded, therefore, that the form of the Apollo 14 and 17 data cannot be accounted for in terms of calibration errors.

B. Power Fluctuations

The possibility that power fluctuations account for the form of the observed data was considered previously in the Apollo 14 data analyses and found unlikely [9]. In the case of the Apollo 17 data, power fluctuations as an explanation for the form of the observed data are even less likely. Figures C-1 and C-2 show the voltage values obtained from Mission Control for the Radial/Lineal Experiment, runs 1 and 2. Figures C-1 and C-2 show very different patterns of voltage variation. The curves of distance versus time for runs 1 and 2, however, duplicate each other quite well. It can be concluded, therefore, that the magnitudes of the power fluctuations were insufficient to have expected any sizeable influence on the form of the color distance versus time curves. Incidentally, the increase of 0.7 V observed at the time interval between about 170 and 230 sec in Figure C-1 did not result in any sharp increase in distance on any of the color versus time curves for that period of time. This latter observation reinforces the conclusion arrived at in the Apollo 14 data analyses that the second-order oscillations observed in the Apollo 14 data for the Radial and Zone cells were not the result of power fluctuations.

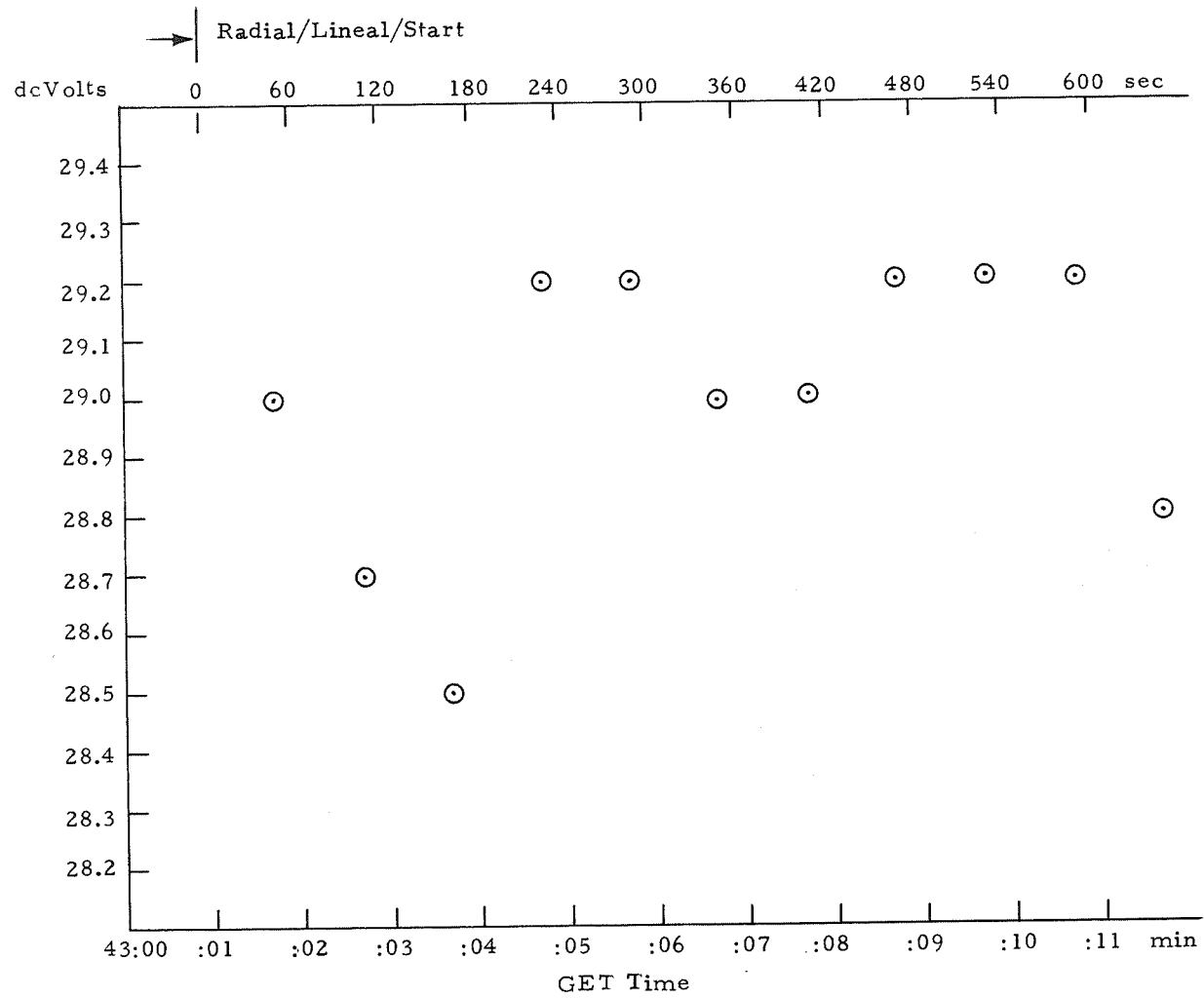


Figure C-1. Voltages at the time of Radial/Lineal run 1.

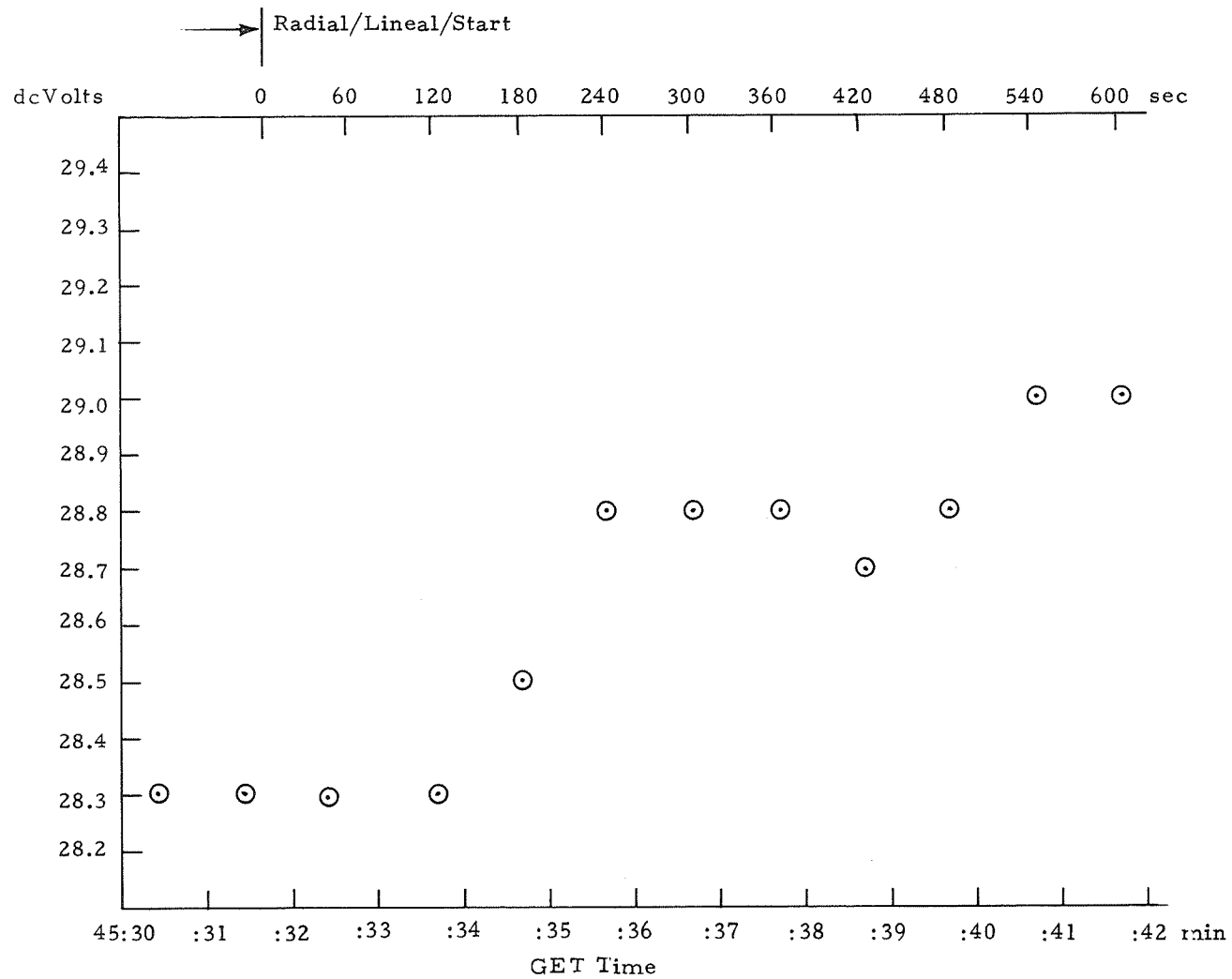


Figure C-2. Voltages at the time of Radial/Lineal run 2.

APPENDIX D

CONDUCTION-RADIATION THERMAL MODELS

A conduction-radiation model of the heat transfer processes in a fluid is constructed by neglecting the effects of fluid motion on the heat transfer. This assumption uncouples the conservation equations and allows an analysis of only the conduction and radiation portion of the energy equation:

$$\rho C_v \frac{\partial T}{\partial t} = \nabla \cdot (k \nabla T) - \nabla \cdot \vec{q}_r + q_E \quad (D-1)$$

This type model is useful because:

- Solutions are easily obtained using existing computer programs.
- Convection solutions can be compared to conduction-only solutions to determine the impact of convection on the fluid behavior.

The conduction-radiation model computer programs which were used to analyze the HFC are (1) VUFACT [41] (calculates radiation view factors) and (2) Thermal analyzer [42] (uses VUFACT inputs and calculates temperatures). The VUFACT program calculates the radiation interchange factors f necessary to compute the radiation heat flux term:

$$q_r = \sigma f (T_i^4 - T_j^4) \quad (D-2)$$

These coefficients f are calculated for arbitrary geometries using the material surface properties, emissivity, absorbtivity, and reflectivity.

The Thermal Analyzer program utilizes a numerical finite-difference method to solve equation (D-1). Both steady-state and transient temperature histories are plotted at user specified node points in the fluid and/or solid boundaries. Temperature-dependent thermal properties and time-varying boundary conditions are easily implemented.

A. Thermal Analysis

Thermal analyses were performed on the Radial, Lineal and Flow Pattern heating units for accurately predicting temperature profiles for comparison with flight data. In the thermal analyses, each heating unit was divided into incremental volumes and a set of generalized differential energy transfer equations was established. Considering an incremental volume in terms of its heat capacity and its radiative, conductive, and convective energy transfer gives the following total energy balance for an arbitrary volume j :

$$\begin{aligned} \rho_j V_j C_{P_j} dT_j/d\theta &= \sum \sigma A_j \mathcal{F}_{j-i} (T_j^4 - T_i^4) + h_{c_j} A_{c_j} (T_f - T_j) \\ &- h'_{c_j} A'_{c_j} (T_j - T_f) - \sum \sigma A'_j \mathcal{F}_{j-a} (T_j^4 - T_a^4) \\ &- \sum_{n=1}^N K_n A_n dT_{j-n}/dX_{j-n} + Q_j \quad , \end{aligned}$$

where

$\rho_j V_j C_{P_j} dT_j/d\theta$	is the rate of change of sensible heat due to energy transfer to or from element j
$h_{c_j} A_{c_j} (T_f - T_j)$	is the energy rate gained or lost because of convective exchange between element j and the internal fluid
$h'_{c_j} A'_{c_j} (T_j - T_f)$	is the energy rate gained or lost because of convective exchange between element j and the external fluid
$\sigma A_j \mathcal{F}_{j-i} (T_j^4 - T_i^4)$	is the energy rate gained or lost because of radiant exchange between element j and element i

$\sigma A_j F_{j-a} (T_j^4 - T_a^4)$ is the energy rate gained or lost because of radiant exchange between element j and the ambient "air"

$K_n A_n dT_{j-n} / dX_{j-n}$ is the energy rate conducted to or from j along path n due to adjoining elements

Q_j is the internal heat generation.

In the above equation, it is assumed that the element under consideration has a uniform temperature $T = T_j$ over its volume.

The generalized differential energy transfer equations were solved mathematically by the Lockheed-Huntsville Thermal Analyzer Computer Program [42] using the following finite difference form of the equation:

$$T_{i, \theta + \Delta\theta} = T_{i, \theta} + \left(\sum_j \frac{T_{j, \theta}}{R_{ij}} - T_{i, \theta} \sum_j \frac{1}{R_{ij}} + Q_{i, \theta} \right) \frac{\Delta\theta}{c_i},$$

where

- θ and $\theta + \Delta\theta$ = times
- R_{ij} = the thermal resistance from node i to node j
- C_i = the thermal capacitance of node i
- Q_i = an arbitrary heat input to node i
- T_i and T_j = temperatures of the subscripted nodes.

B. Thermal Models

Thermal models for the Radial, Lineal and Flow Pattern heating units were developed to calculate the transient temperature distributions for comparison with the Apollo 17 flight data. Heat transfer paths were defined including all important locations at which changes occur affecting the thermal parameters (such as material, area, mode of heat transfer, joints, etc.). Locations at which the temperatures were calculated (referred to as nodes) were selected along the various heat paths based on the symmetry of the structure and the areas of major interest.

The nodal networks for the thermal models which were used are shown in Figures D-1, D-2, and D-3. The Radial heating unit thermal model (Fig. D-1)

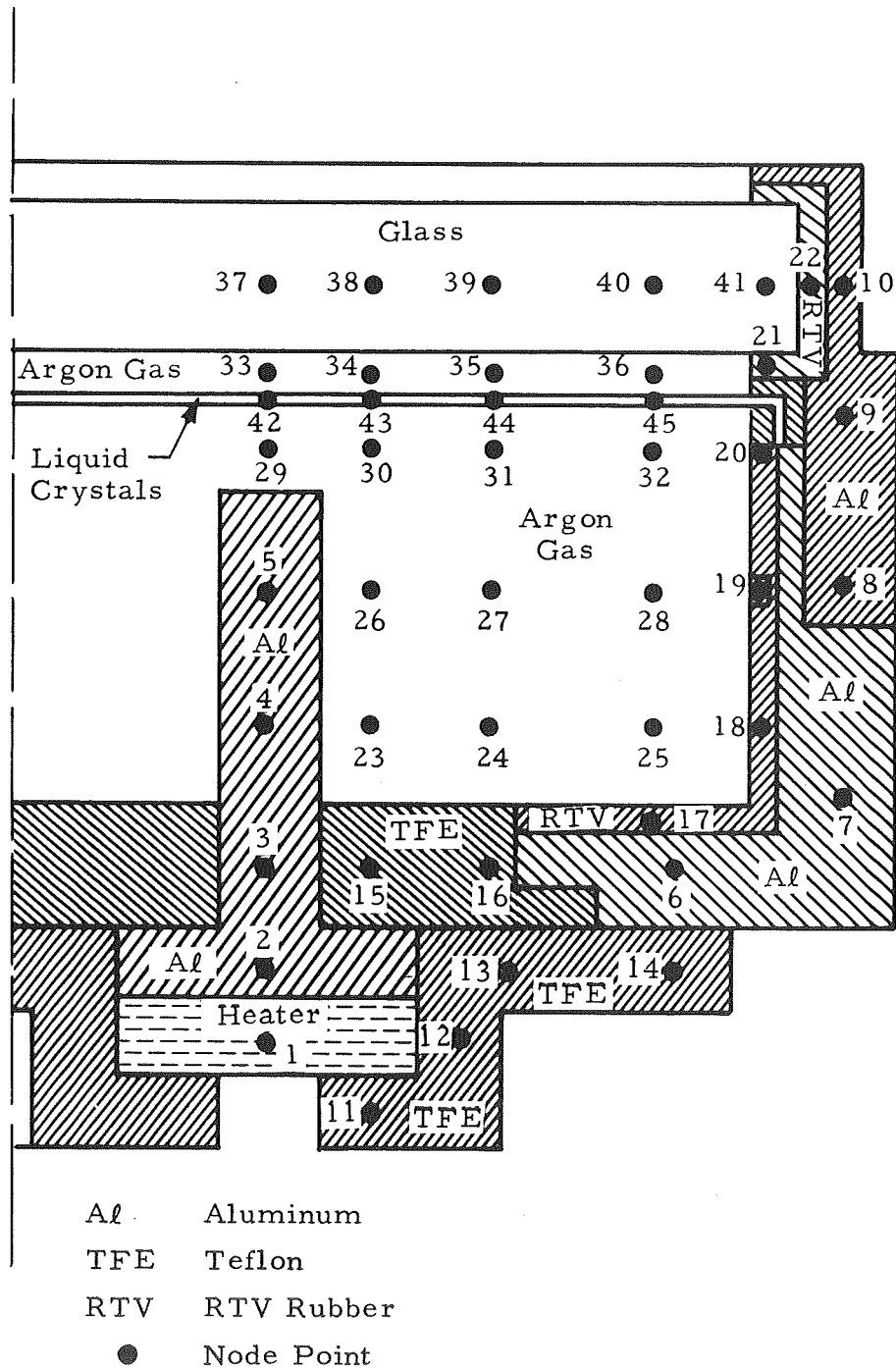


Figure D-1. Nodal network for conduction/radiation thermal model of Apollo 17 HFC Radial cell.

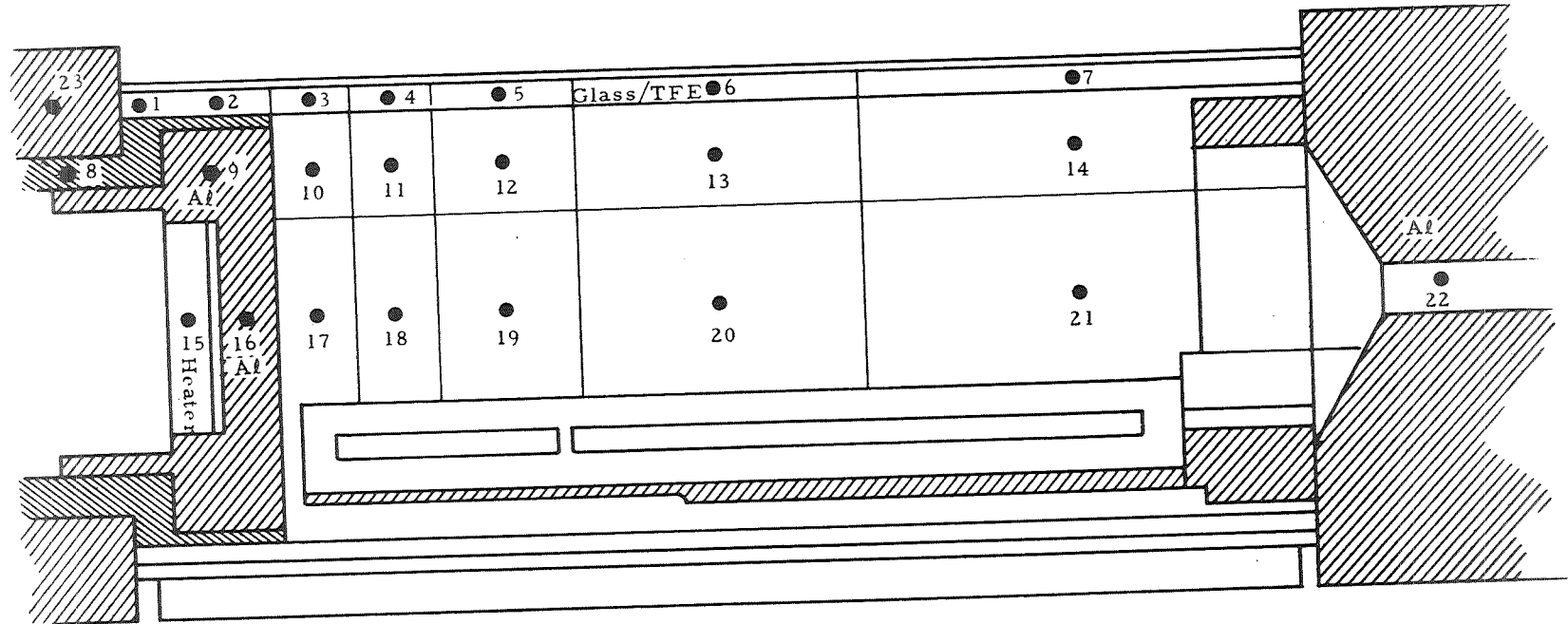


Figure D-2. Nodal network for conduction thermal model of Apollo 17 HFC Lineal cell.

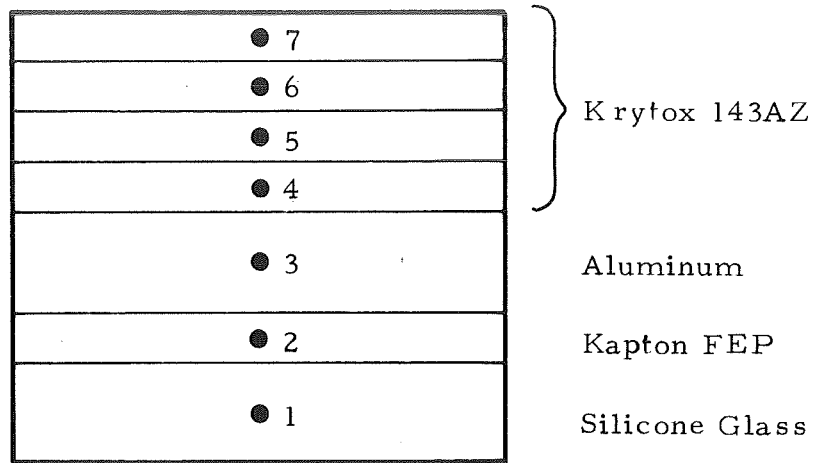


Figure D-3. One-dimensional nodal network for conduction/radiation thermal model of Apollo 17 HFC Flow Pattern cell.

includes conduction, radiation, and external convection. The Linear and Flow Pattern heating unit thermal models (Figs. D-2 and D-3, respectively) include conduction and external convection. A list of the thermal properties used in the development of the thermal models is given in Table D-1.

The computational error associated with thermal modeling and the finite difference method of solution depends on the construction of the thermal model (i. e., how the physical geometry is divided into nodes) and the thermal properties of the material. Past experience with the thermal analyzer program indicates that the accuracy is well within the limits of the properties data. Therefore, the properties data become the controlling factor in determining the accuracy of the thermal model. A summary of the errors expected in the Radial heating unit model is presented in the following.

TABLE D-1. THERMAL AND FLUID PROPERTIES

Fluid	Temperature	Density	Dynamic Viscosity	Kinematic Viscosity	Thermal Conductivity	Thermal Diffusivity	Coefficient of Expansion	Specific Heat	Prandtl Number
	T, °F (°C)	ρ , lbm/ft ³ (gm/cm ³)	μ , lbm/ft-sec (poise)	ν , ft ² /sec (stoke)	k, Btu/hr-ft-°F (cal/sec-cm-°C)	α , ft ² /sec (cm ² /sec)	β , 1/°F (1/°C)	C_p , Btu/lbm-°F (cal/gm-°C)	Pr
CO ₂	150	0.1	1.14×10^{-5}	1.14×10^{-4}	1.12×10^{-2}	1.50×10^{-4}	2.07×10^{-3}	0.21	0.76
	(65.5)	(1.0×10^{-3})	(1.70×10^{-4})	(0.106)	(4.63×10^{-5})	(0.140)	(3.72×10^{-3})	(0.21)	0.72
	300	0.082	1.37×10^{-5}	1.67×10^{-4}	1.49×10^{-2}	2.32×10^{-4}	2.07×10^{-3}	0.23	
	(149)	(1.31×10^{-3})	(2.04×10^{-4})	(0.155)	(6.16×10^{-5})	(0.216)	(3.72×10^{-3})	(0.23)	
Water	150	61.2	0.292×10^{-3}	4.77×10^{-6}	0.384	1.74×10^{-6}	1.15×10^{-4}	1.0	2.74
	(65.5)	(0.98)	(4.35×10^{-3})	(4.43×10^{-3})	(1.59×10^{-3})	(1.62×10^{-3})	(2.07×10^{-4})	(1.0)	
Sucrose, 20%	150	67.4	0.498×10^{-3}	0.739×10^{-5}	0.301	1.43×10^{-6}	1.15×10^{-4}	0.87	5.0
	(65.5)	(1.08)	(0.742×10^{-2})	(0.687×10^{-2})	(1.24×10^{-3})	(1.37×10^{-3})	(2.07×10^{-4})	(0.87)	
Argon	300	0.102	1.95×10^{-5}	1.91×10^{-4}	1.35×10^{-2}	2.82×10^{-4}	2.06×10^{-3}	0.13	0.68
	(149)	(1.64×10^{-3})	(2.9×10^{-4})	(0.177)	(5.57×10^{-5})	(0.262)	(3.70×10^{-3})	(0.13)	
Krytox 143AA	275	103	3.05×10^{-3}	2.96×10^{-5}	4.5×10^{-2}	4.5×10^{-7}	5.8×10^{-4}	0.27	65.7
	(135)	(1.65)	(4.54×10^{-4})	(2.75×10^{-2})	(1.86×10^{-4})	(4.18×10^{-4})	(10.4×10^{-4})	(0.27)	
Krytox 143AZ	100	114.2	2.204×10^{-2}	1.93×10^{-4}	—	—	6.1×10^{-4}	—	
	(37.8)	(1.83)	(0.329)	(0.18)	—	—	(1.1×10^{-3})	—	

Source of Error	Error
Thermal Conductivity (Argon)	±5% min.
Radiation	±7%
Heater Power	±4%
Density (Argon)	<< ±1%
Finite Difference	<< ±1%
Dimensions	<< ±1%

A weighted average of these errors gives an accumulated error of approximately ±10 percent of the temperature difference ($T_{x,t} - T_{initial}$) for the Radial heating unit model. Since the thermal properties of the Linear and Flow Pattern heating units are better known and no significant internal radiation exists, it is expected that the error for these models will be approximately half of the Radial model error.

As an example of this error, consider a typical point on the Radial cell curves. The temperature rise is from 25°C to 35°C, resulting in $\Delta T = 10^\circ$, which gives an error of 1°C.

**C. Radial Heating Temperature-Time Curves
(Precision and Error Bands Indicated
by Vertical and Dashed Lines)**

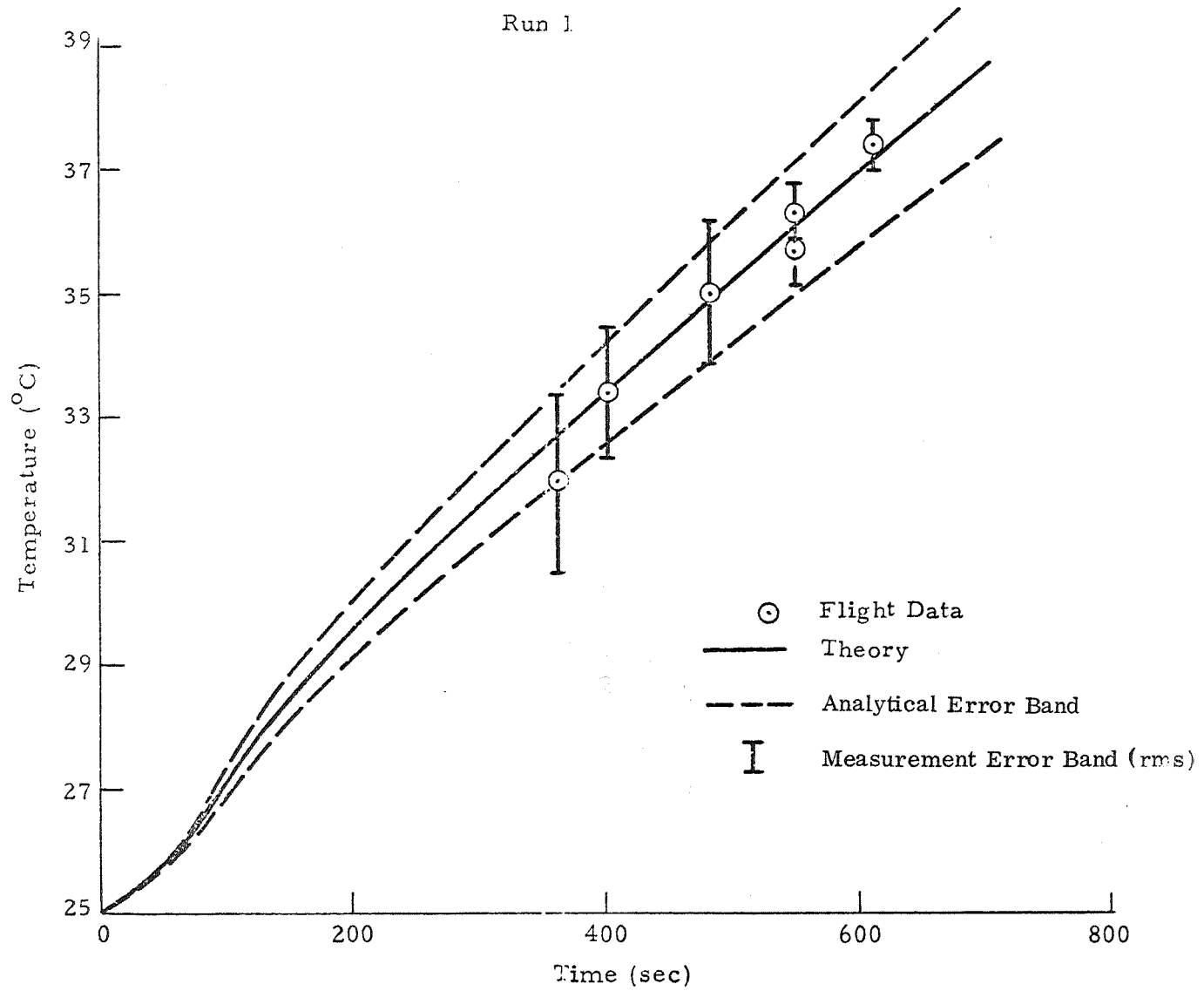


Figure D-4. Radial heating temperature-time curve ($r = 0.5$, run 1).

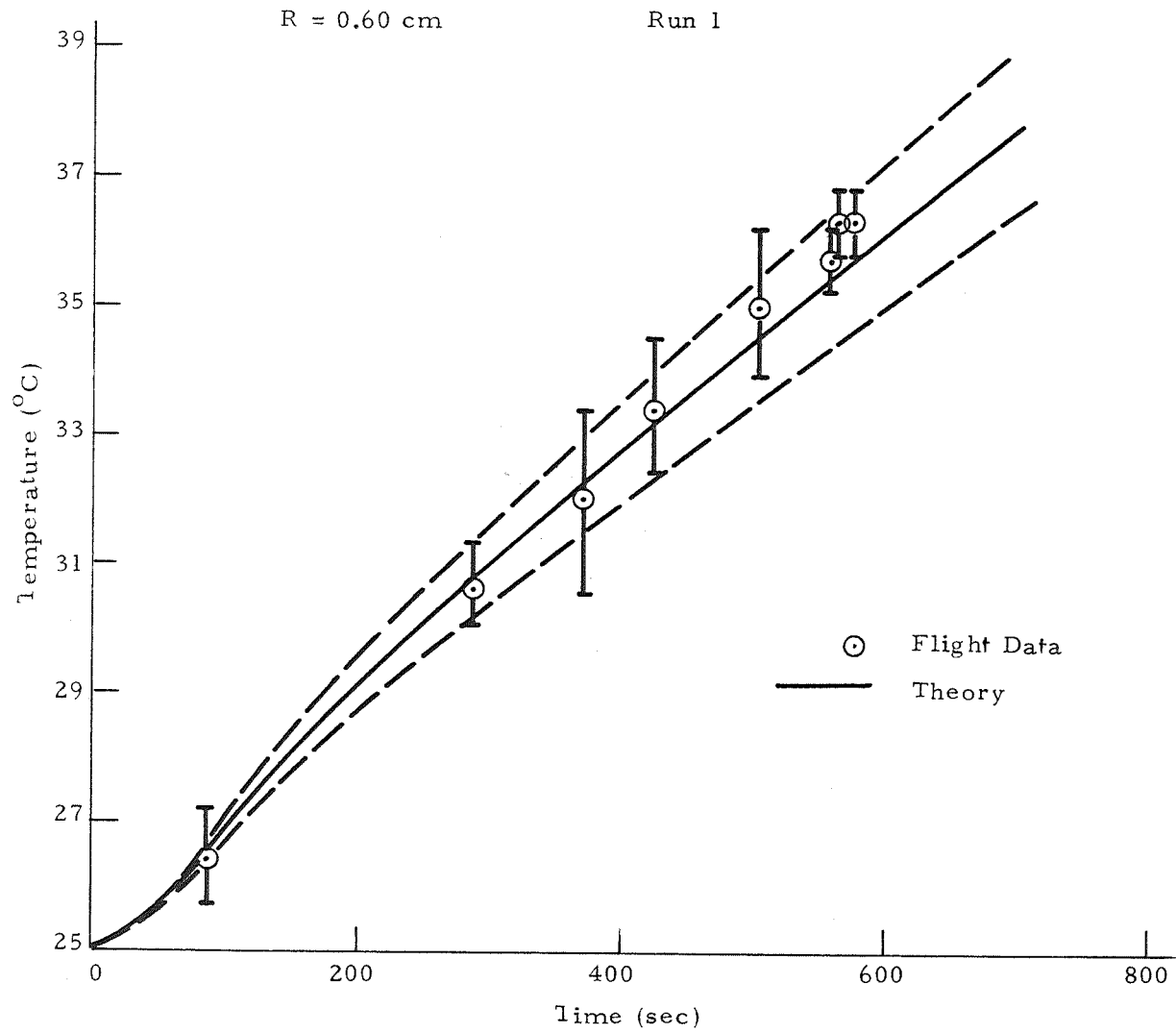


Figure D-5. Radial heating temperature-time curve ($r = 0.6$, run 1).

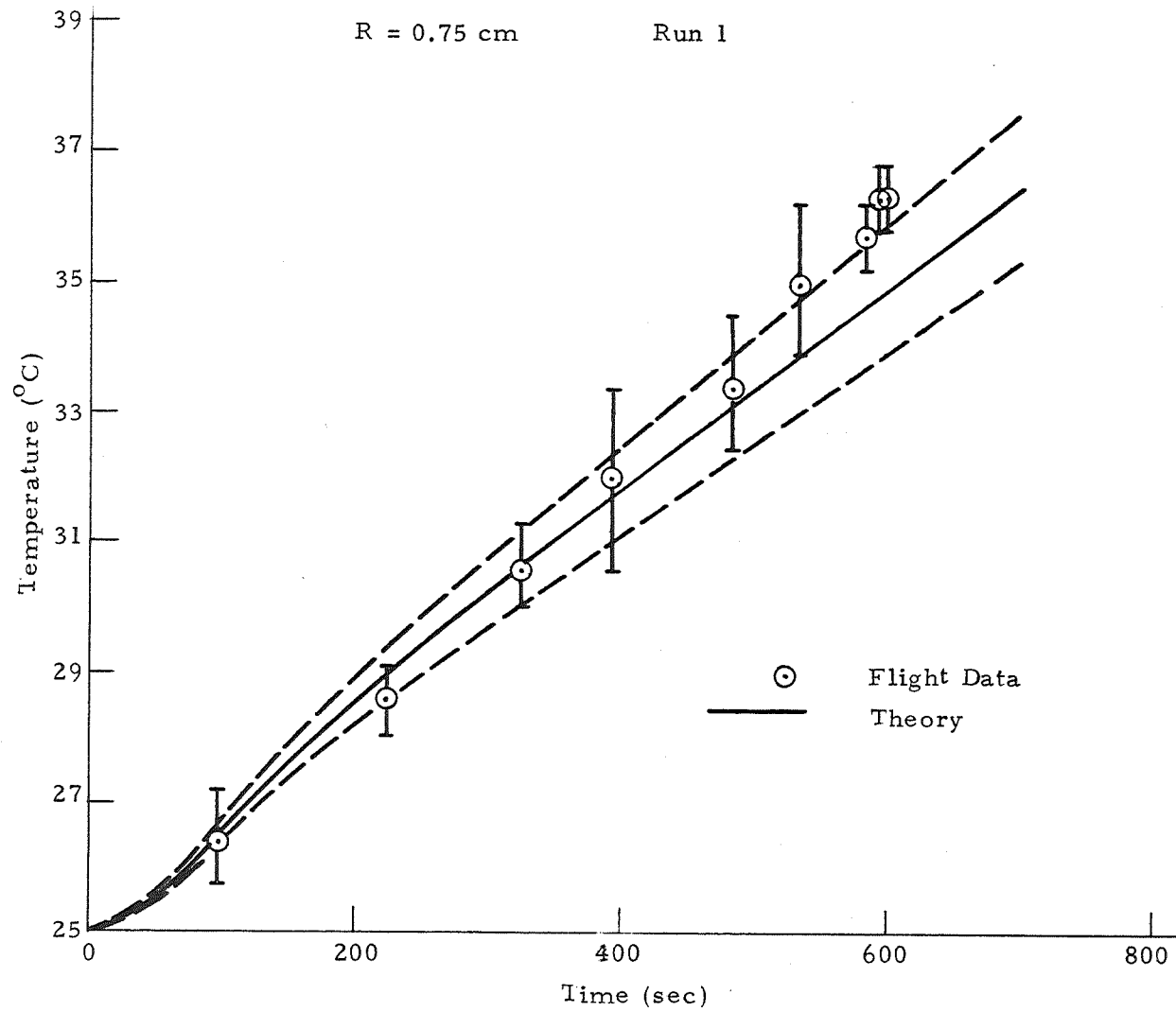


Figure D-6. Radial heating temperature-time curve ($r = 0.75$, run 1).

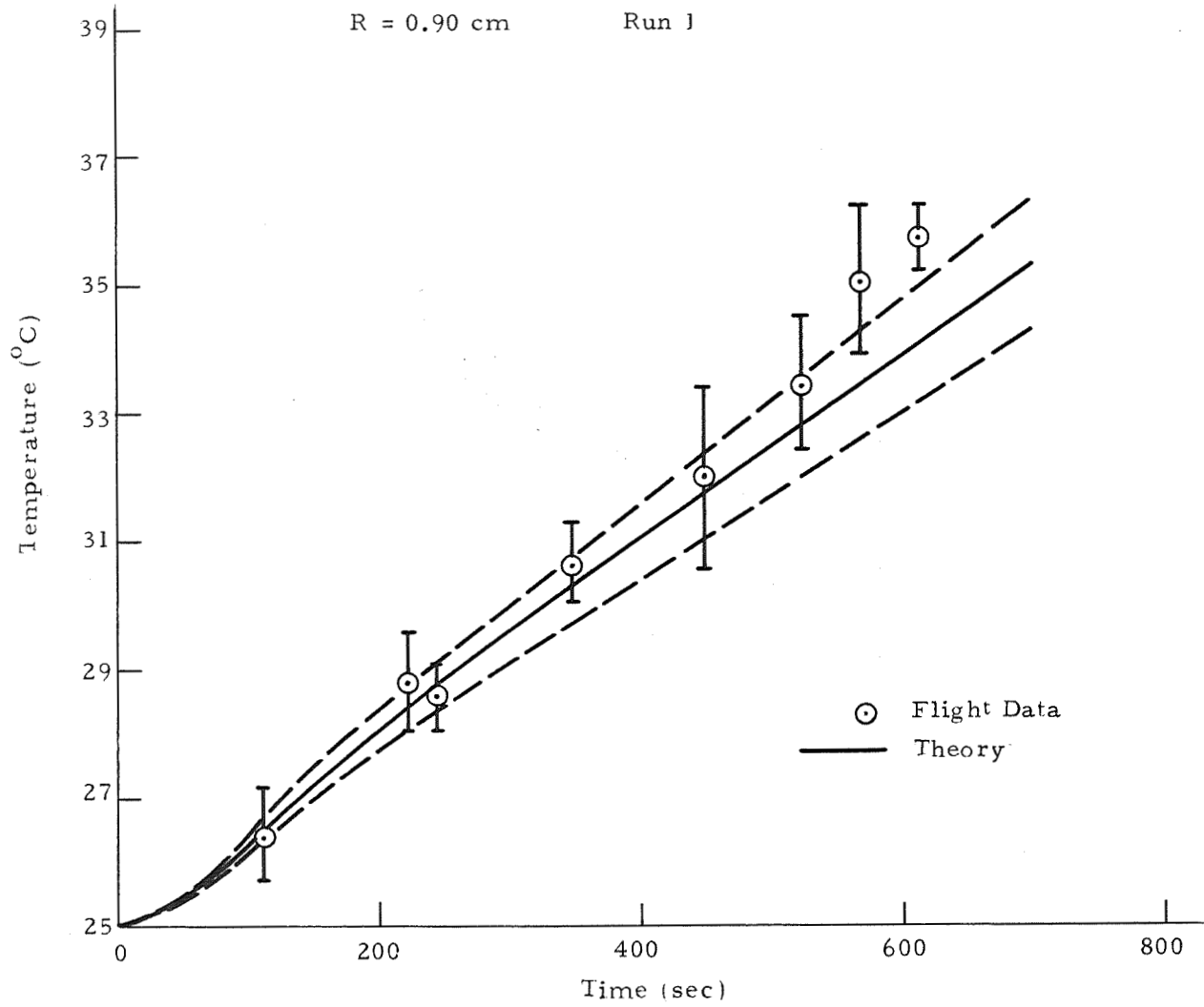


Figure D-7. Radial heating temperature-time curve ($r = 0.9$, run 1).

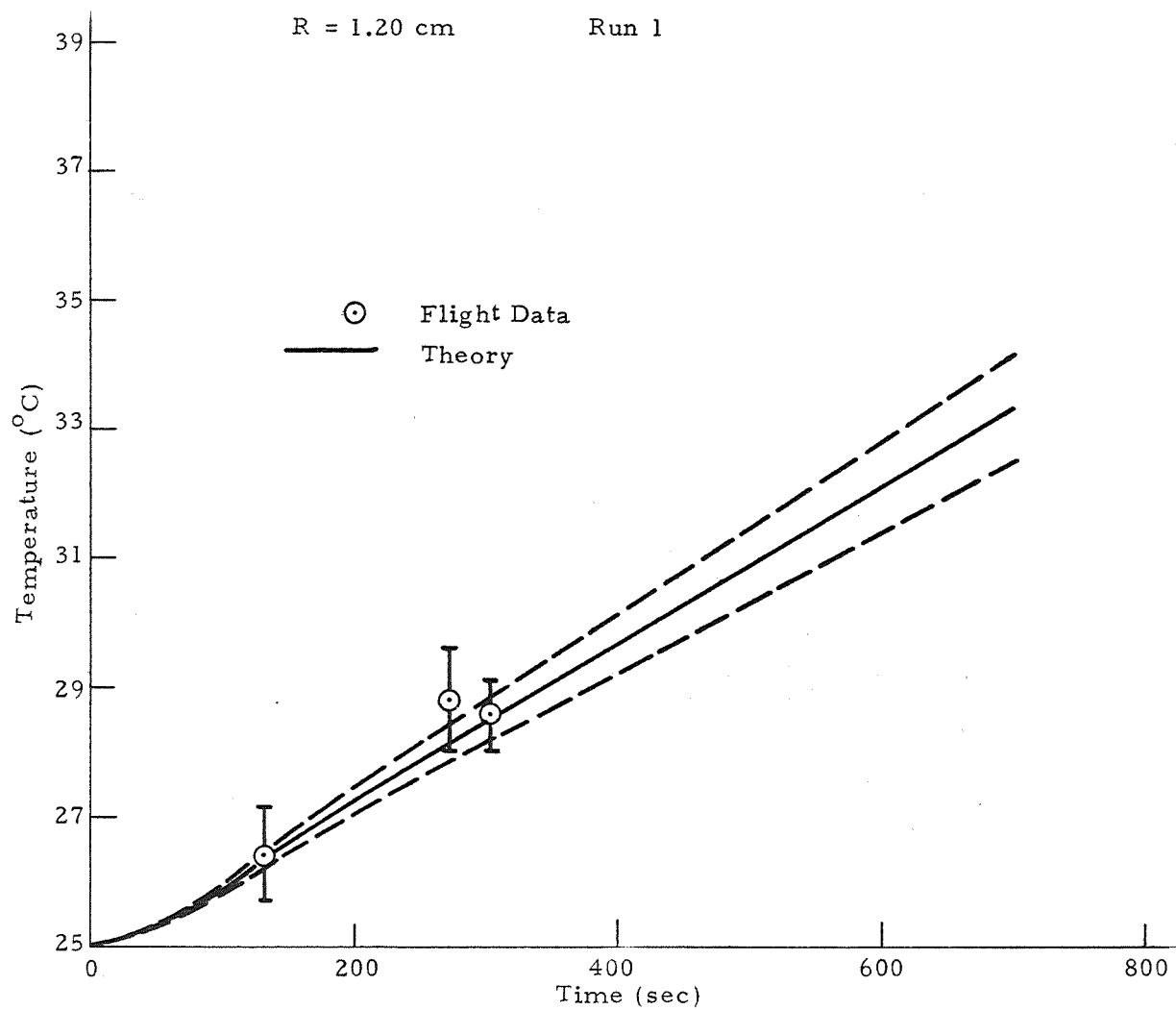


Figure D-8. Radial heating temperature-time curve ($r = 1.2$, run 1).

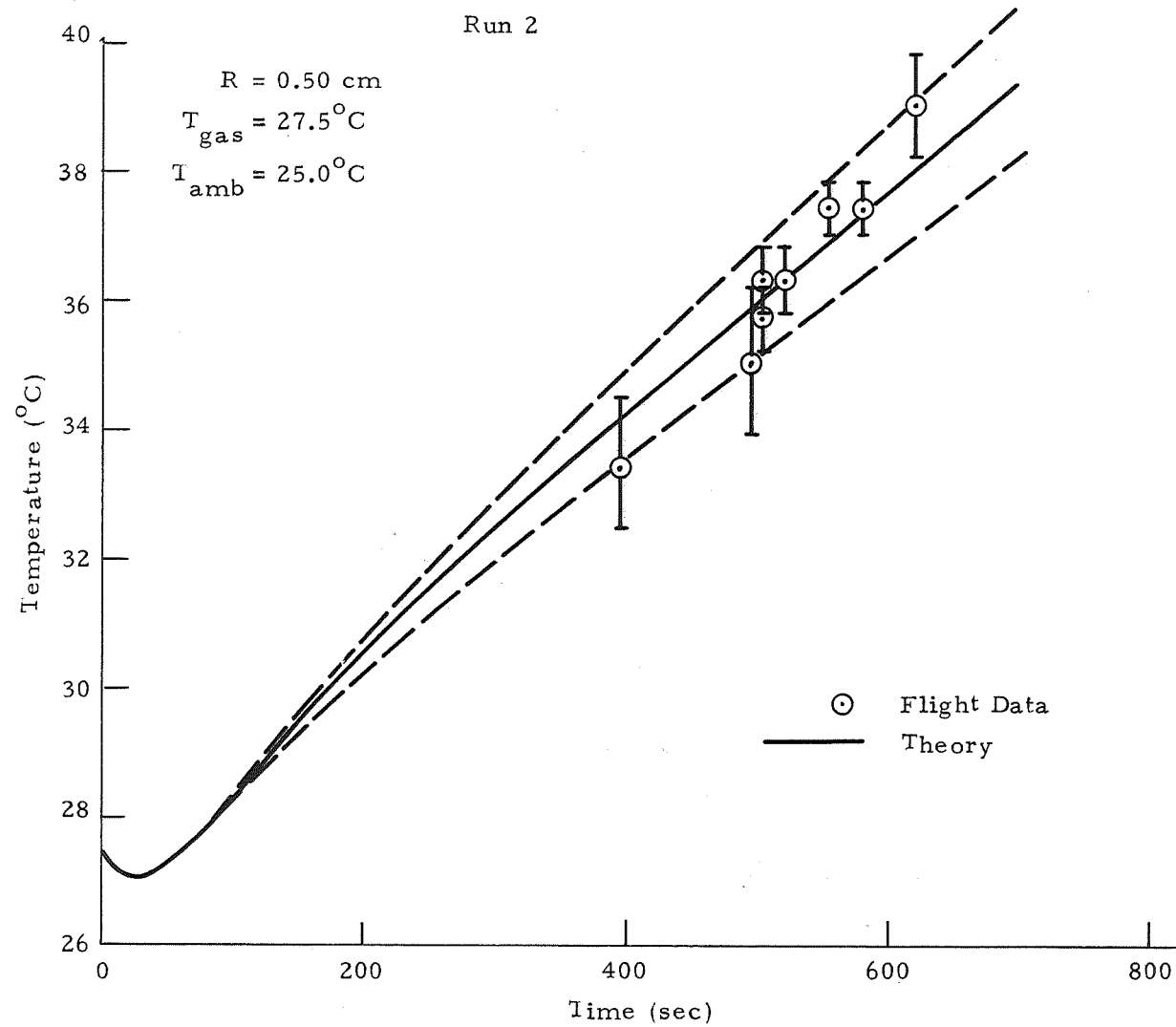


Figure D-9. Radial heating temperature-time curve ($r = 0.5$, run 2).

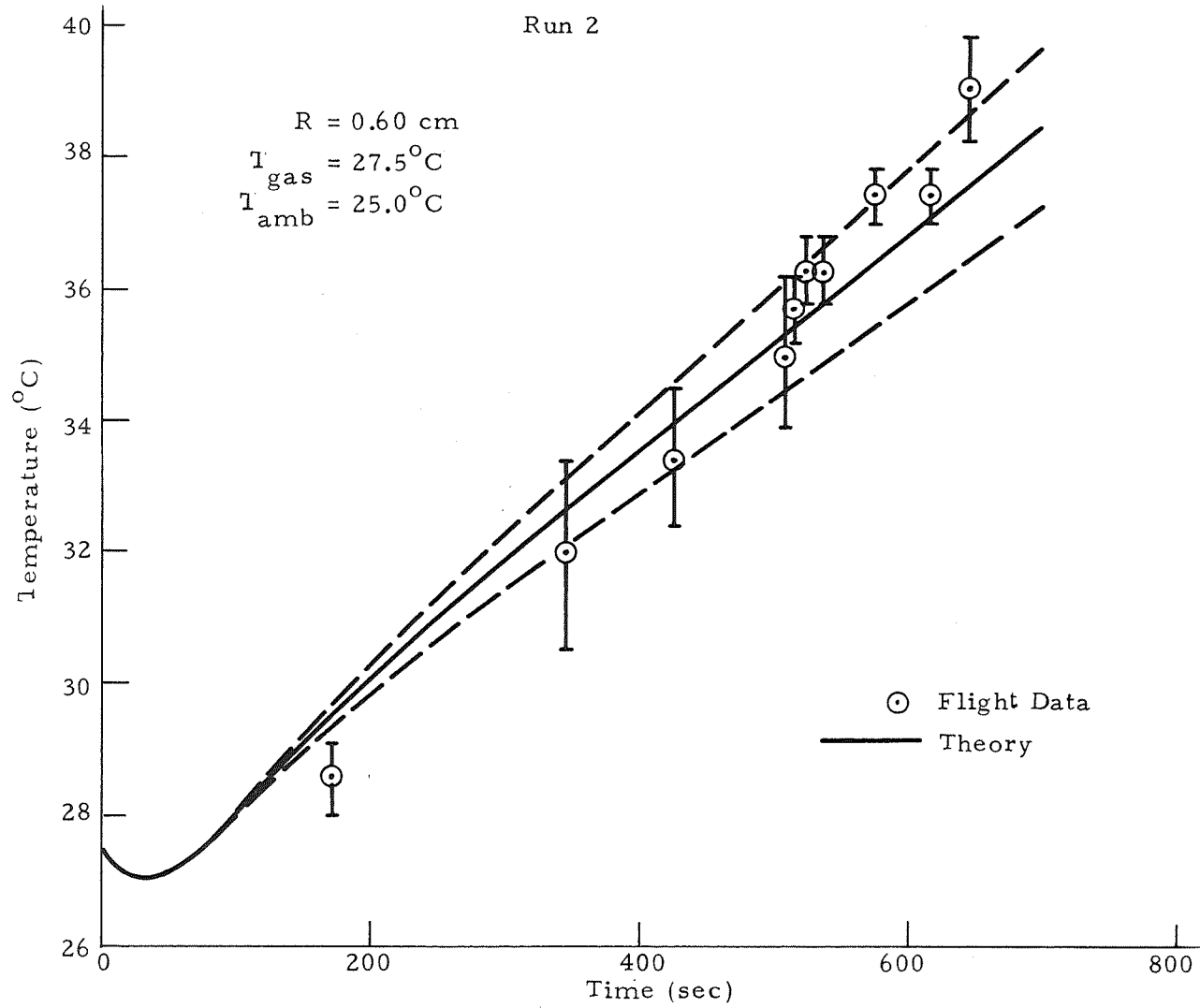


Figure D-10. Radial heating temperature-time curve ($r = 0.6$, run 2).

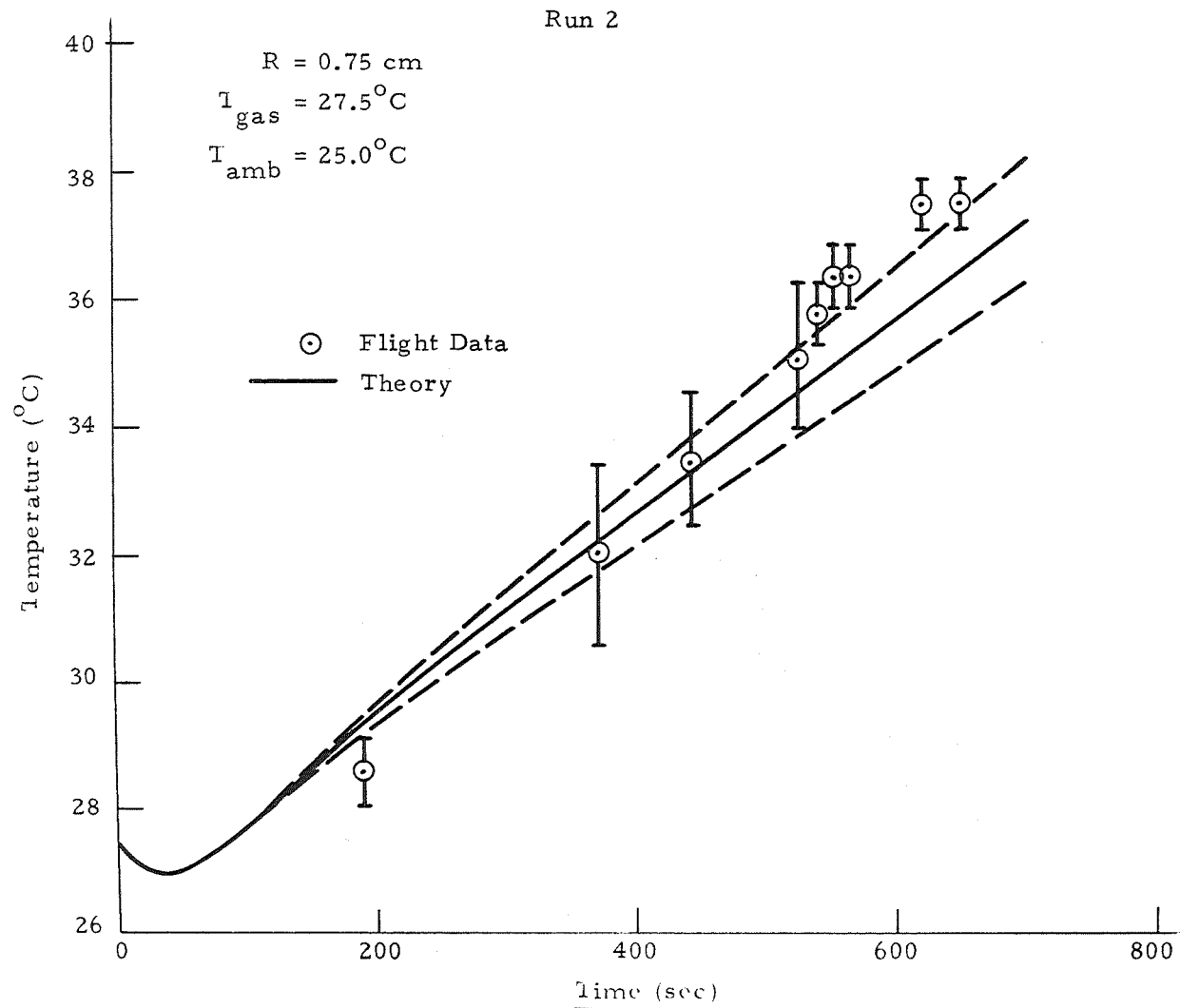


Figure D-11. Radial heating temperature-time curve ($r = 0.75$, run 2).

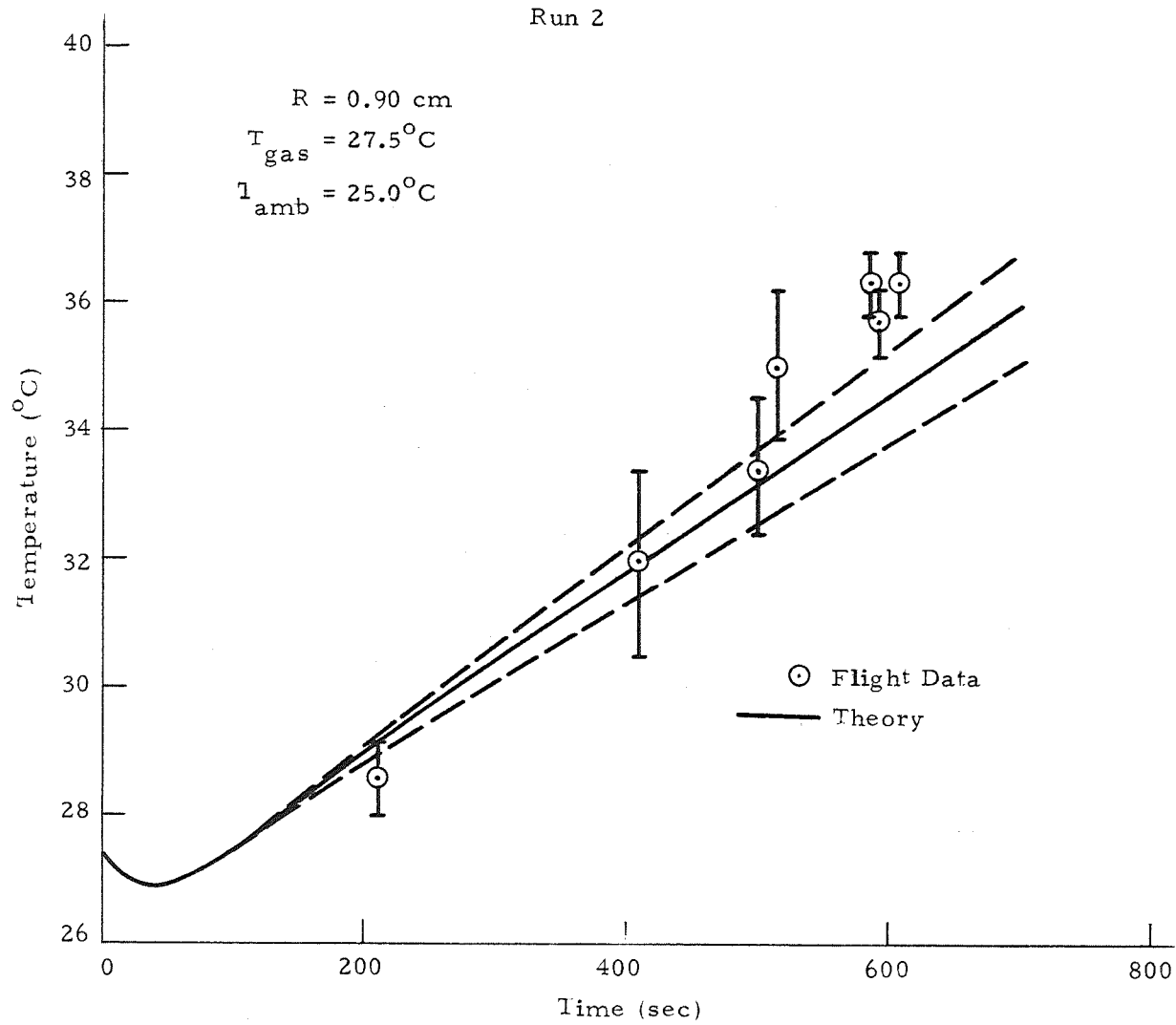


Figure D-12. Radial heating temperature-time curve ($r = 0.9$, run 2).

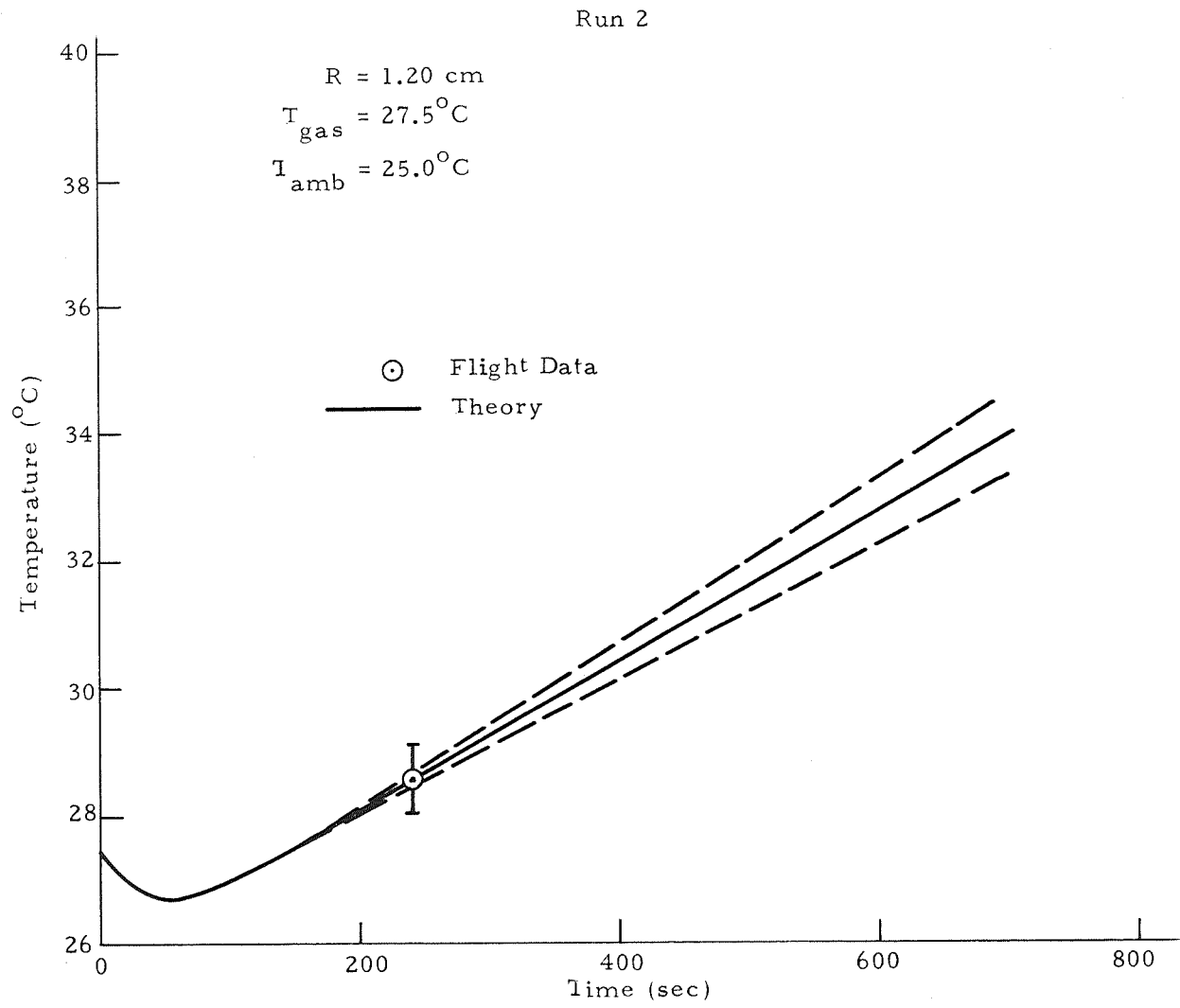
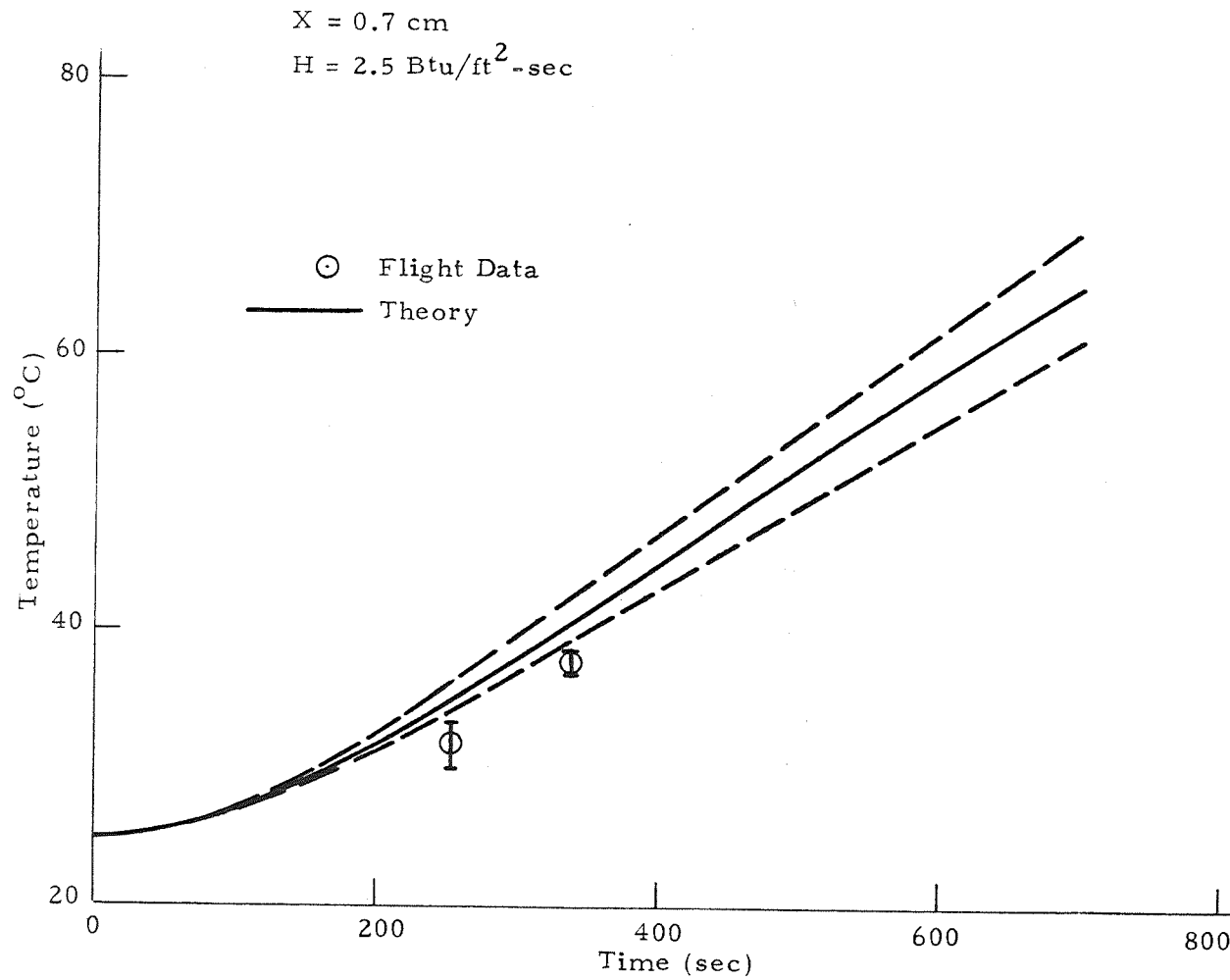


Figure D-13. Radial heating temperature-time curve ($r = 1.2$, run 2).

**D. Lineal Heating Temperature-Time Curves
(Precision and Error Bands Indicated
by Vertical and Dashed Lines)**

Run 1

Figure D-14. Lineal heating temperature-time curve ($X = 0.7$, run 1).

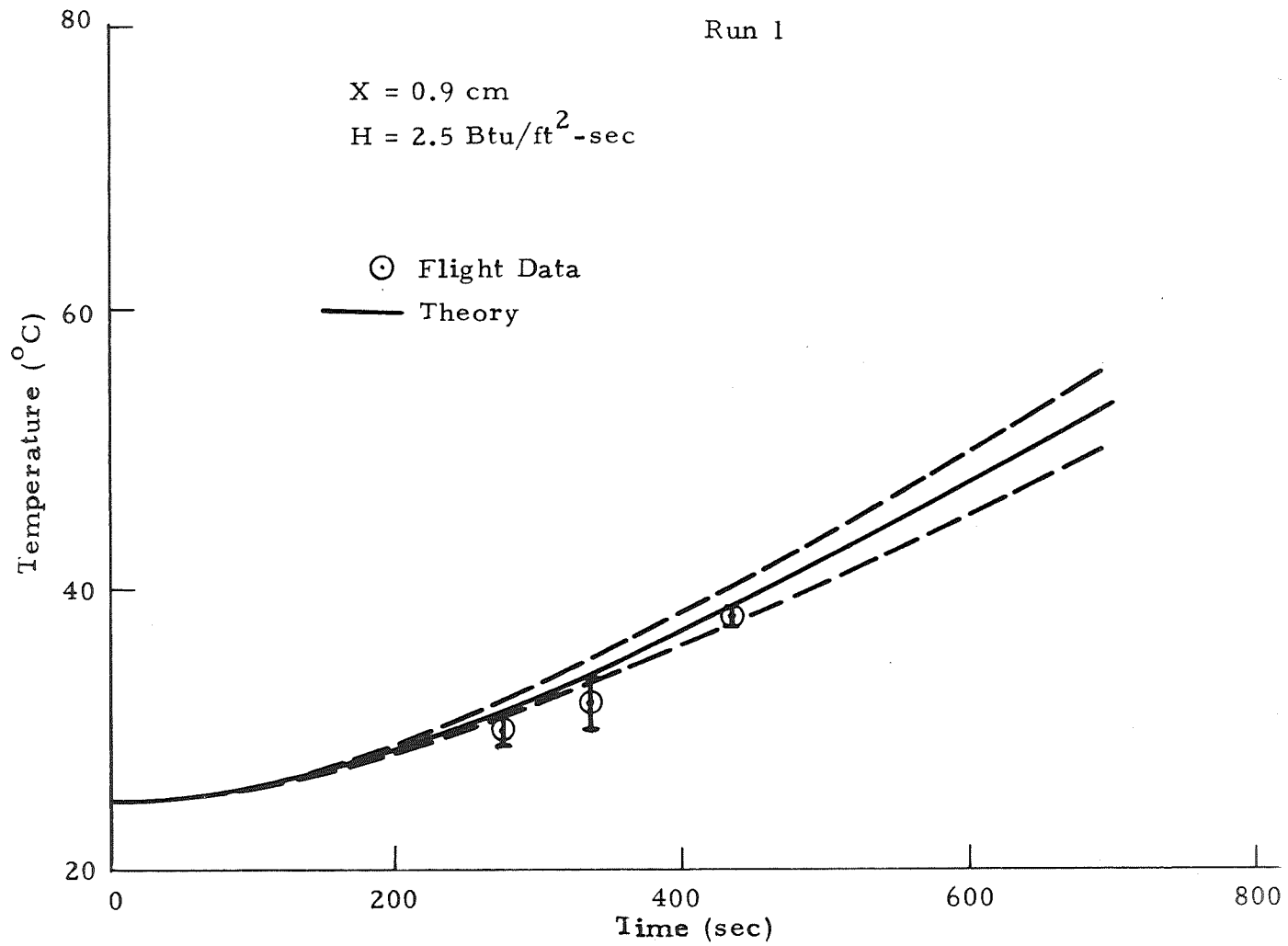


Figure D-15. Lineal heating temperature-time curve ($X = 0.9$, run 1).

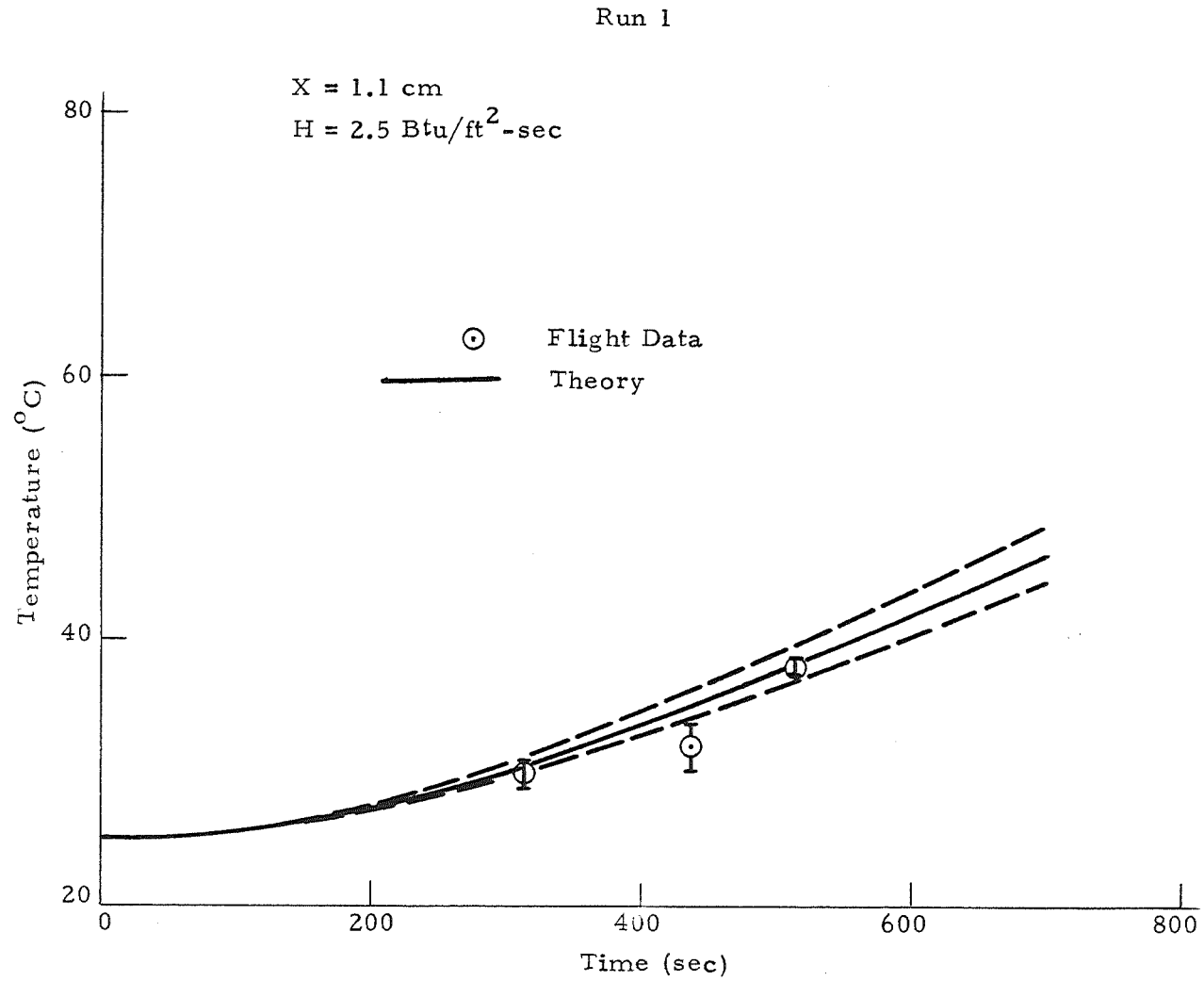


Figure D-16. Lineal heating temperature-time curve ($X = 1.1$, run 1).

Run 1

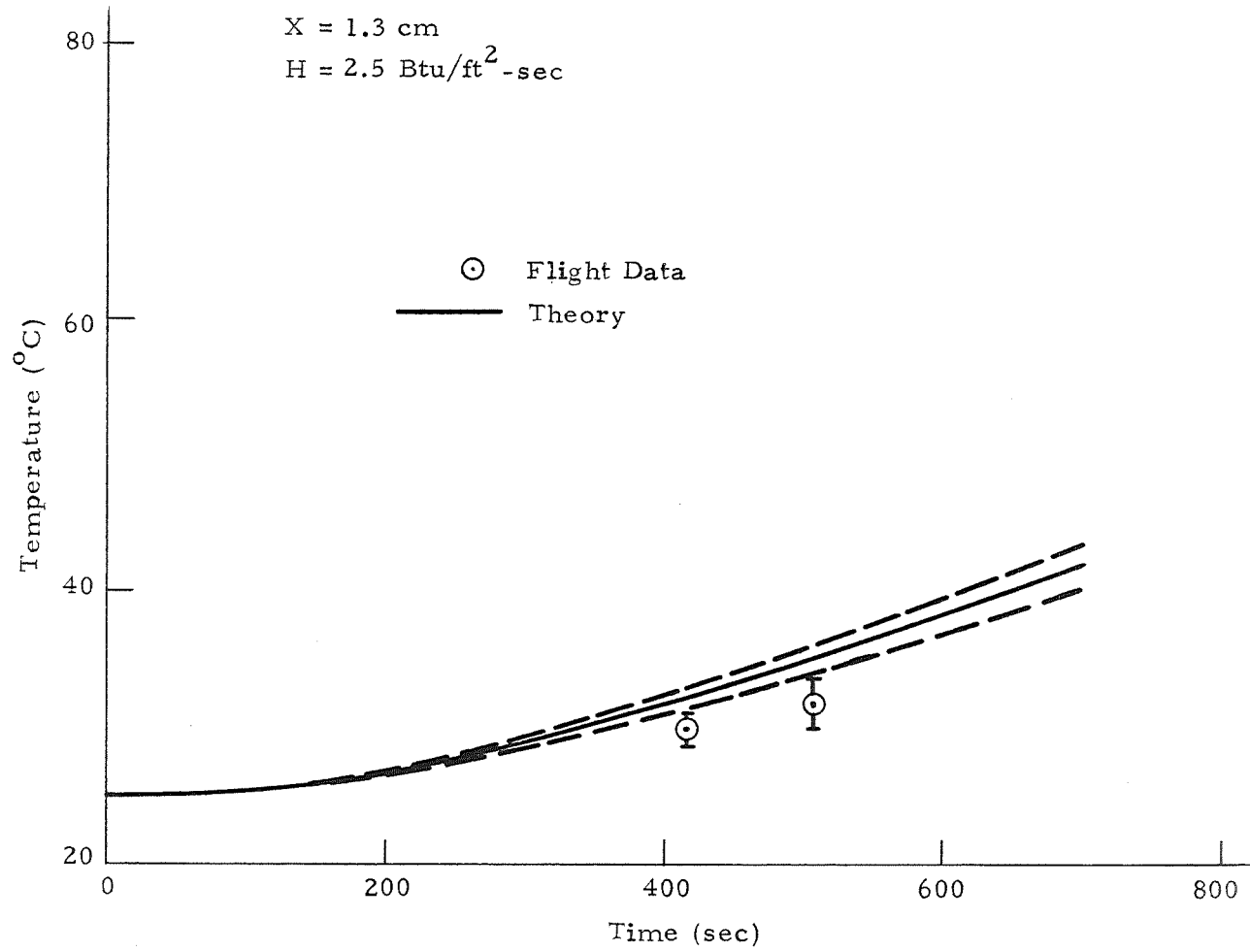


Figure D-17. Lineal heating temperature-time curve ($X = 1.2$, run 1).

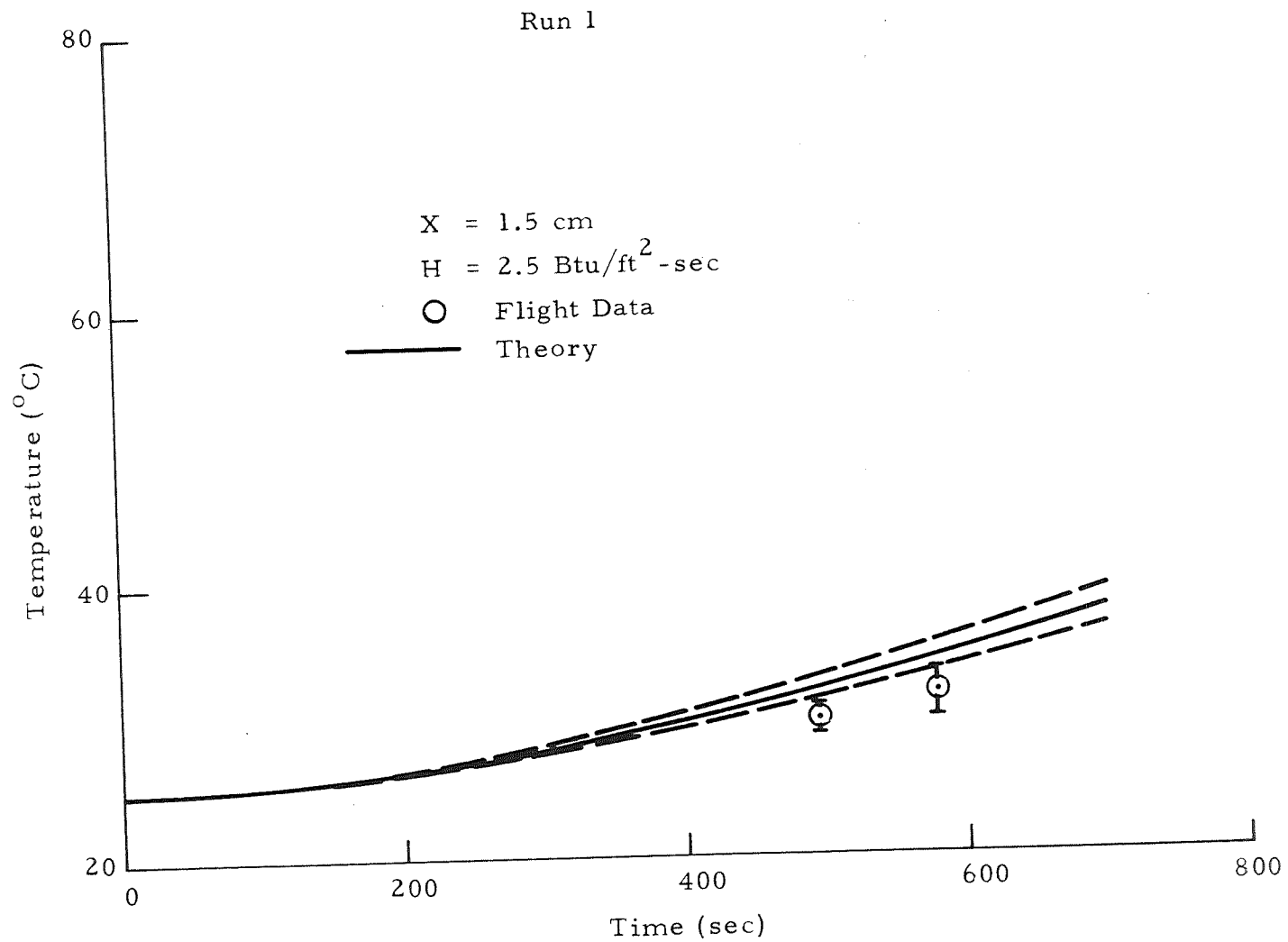


Figure D-18. Lineal heating temperature-time curve ($X = 1.5$, run 1).

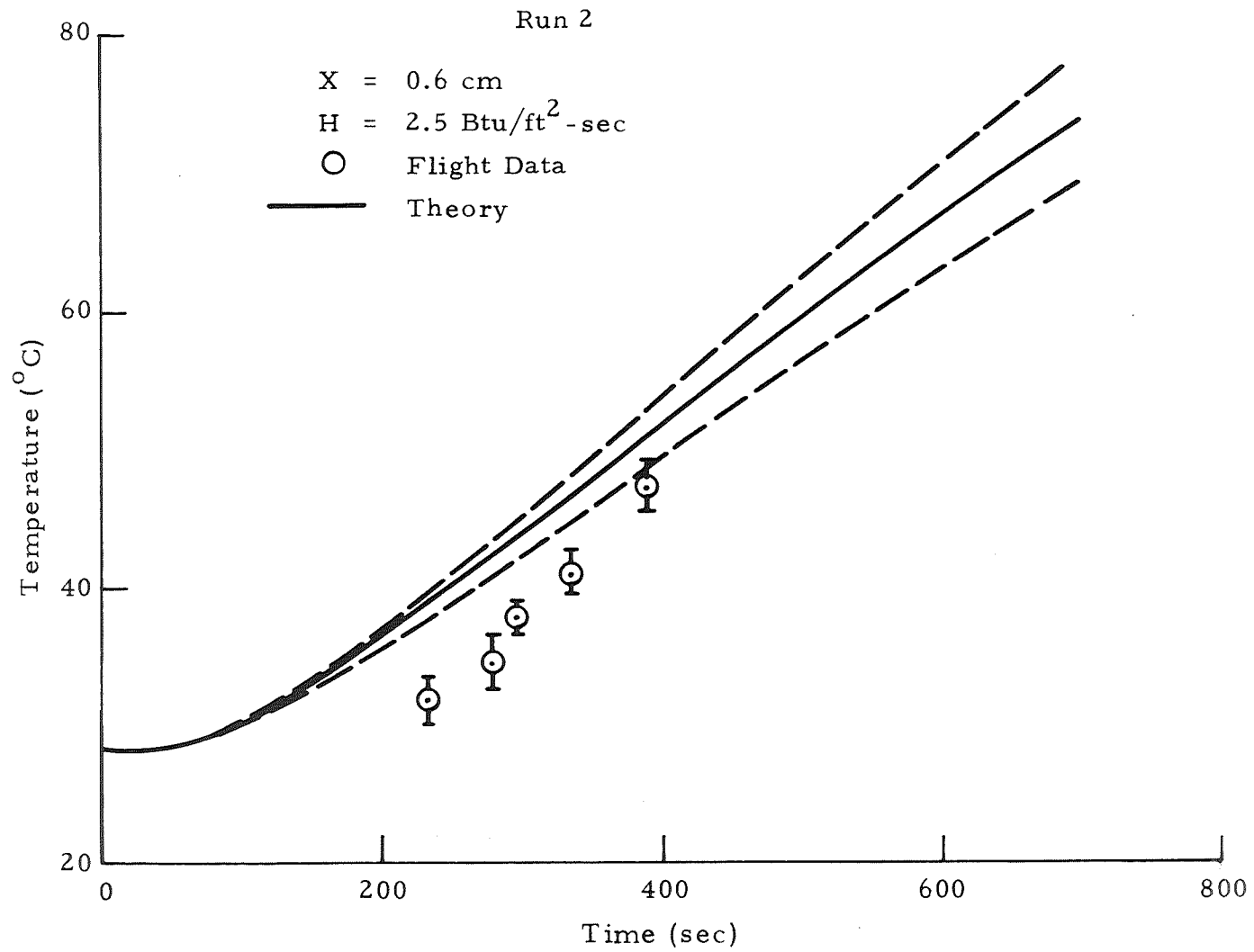


Figure D-19. Lineal heating temperature-time curve ($X = 0.6$, run 2).

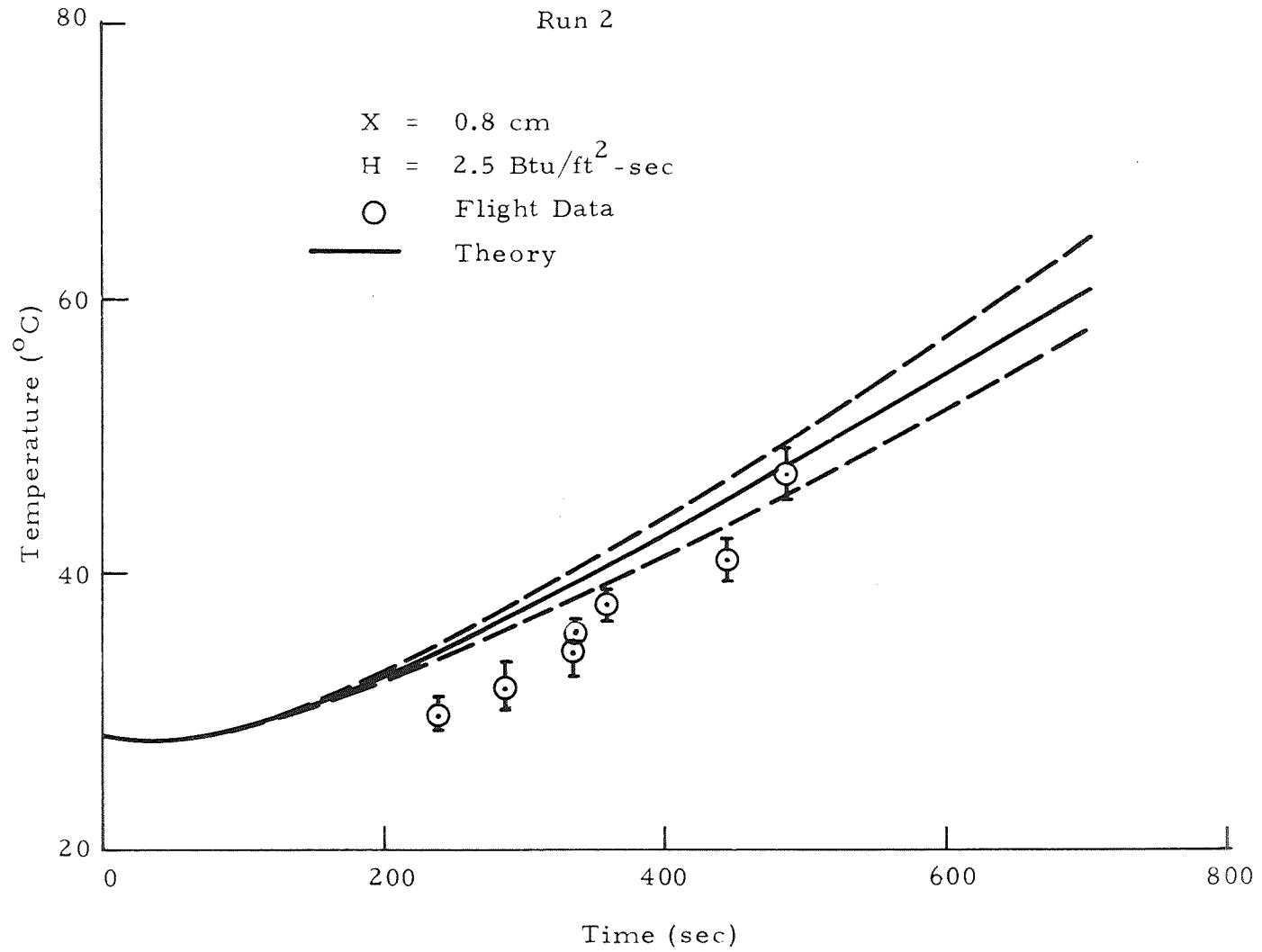


Figure D-20. Lineal heating temperature-time curve ($X = 0.8$, run 2).

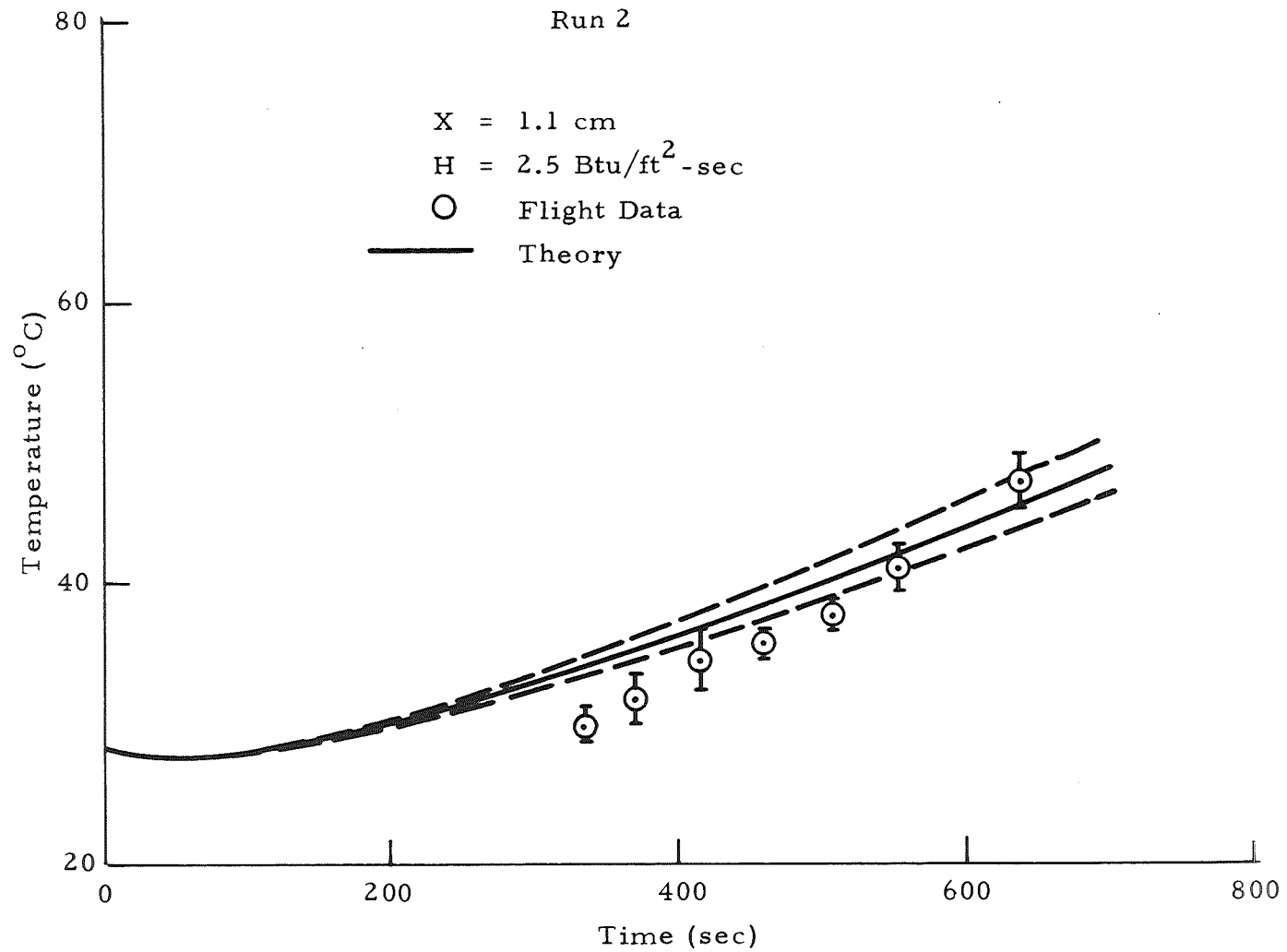


Figure D-21. Lineal heating temperature-time curve ($X = 1.1$, run 2).

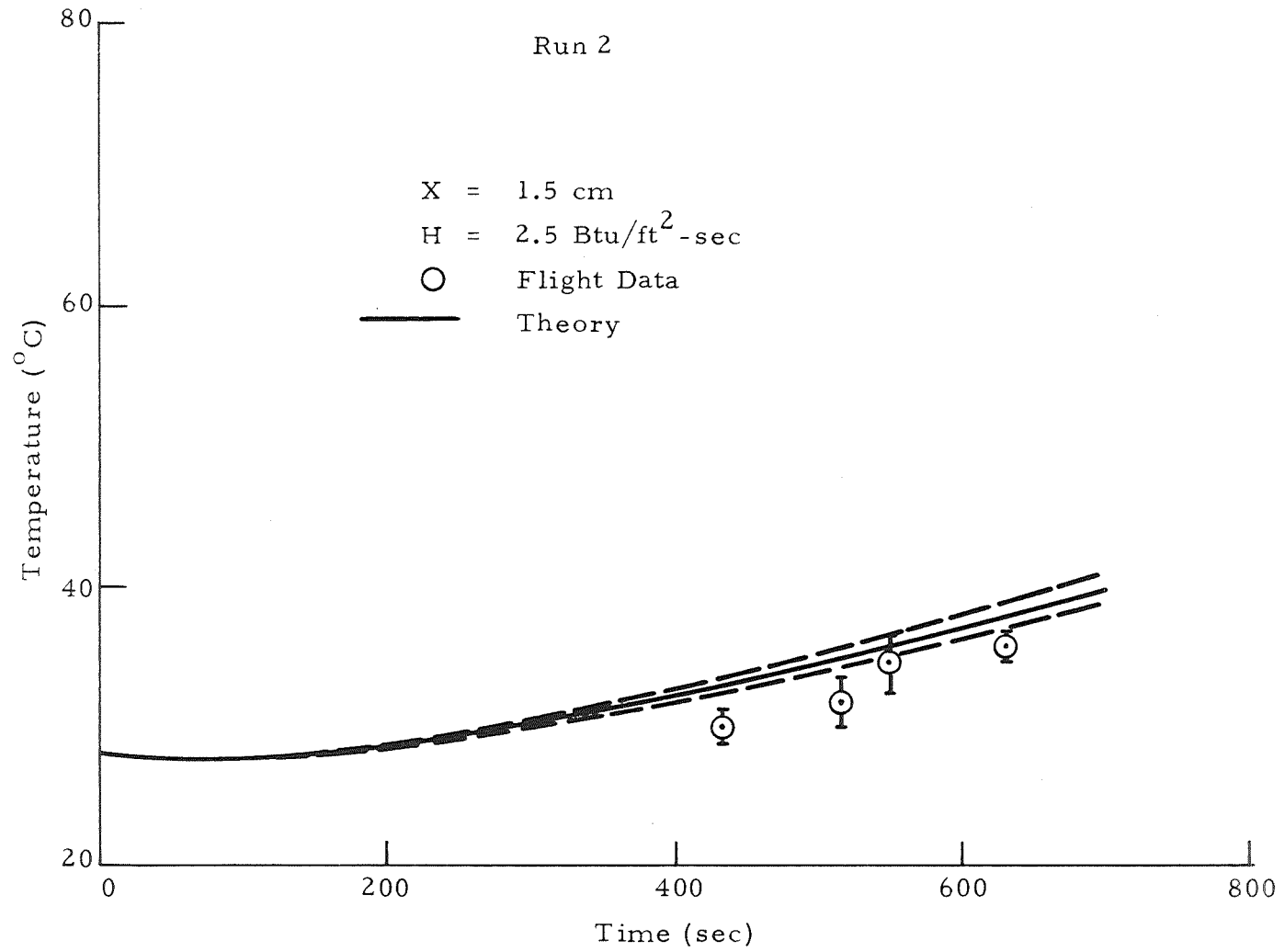


Figure D-22. Lineal heating temperature-time curve (X = 1.5, run 2).

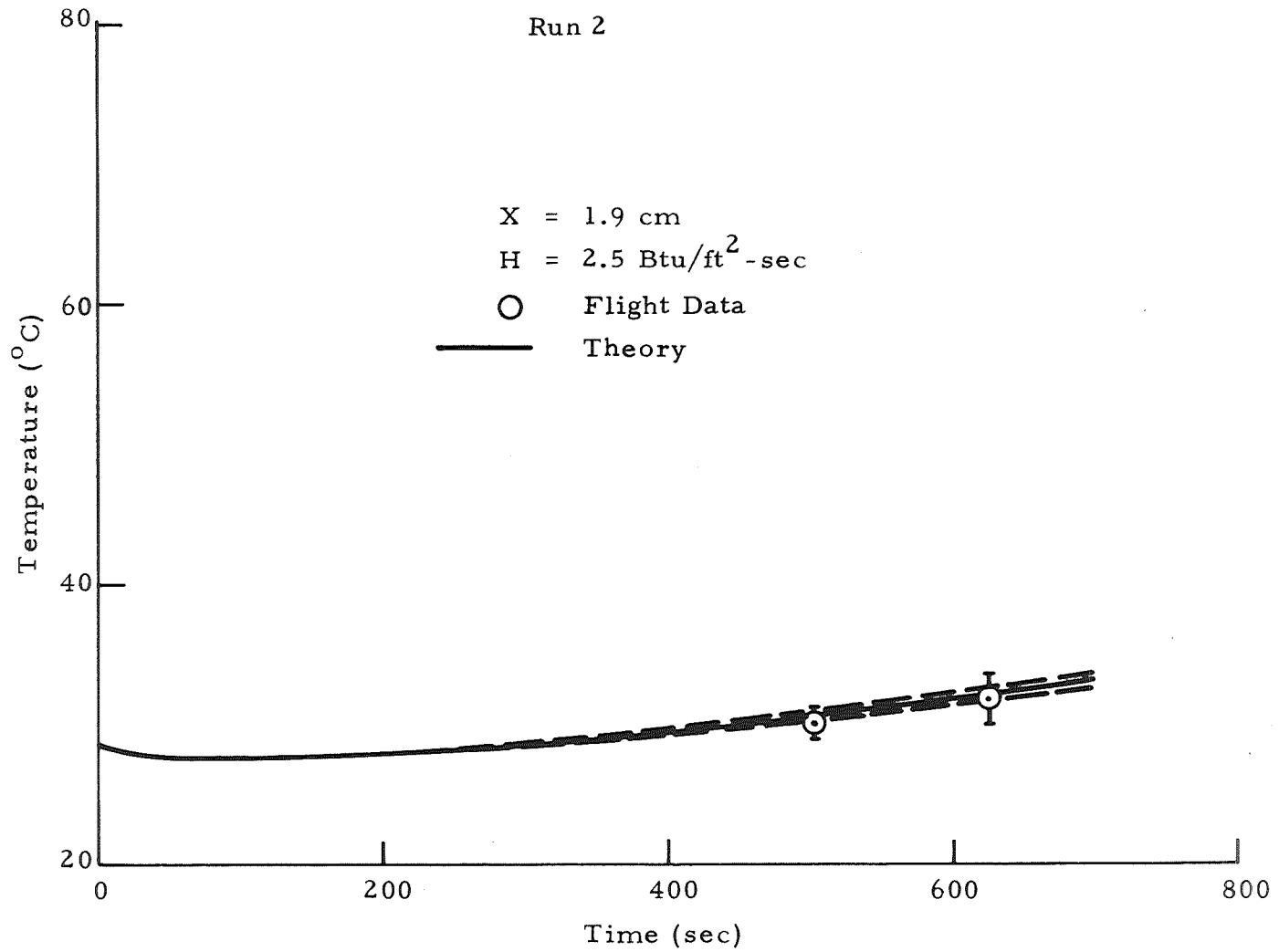
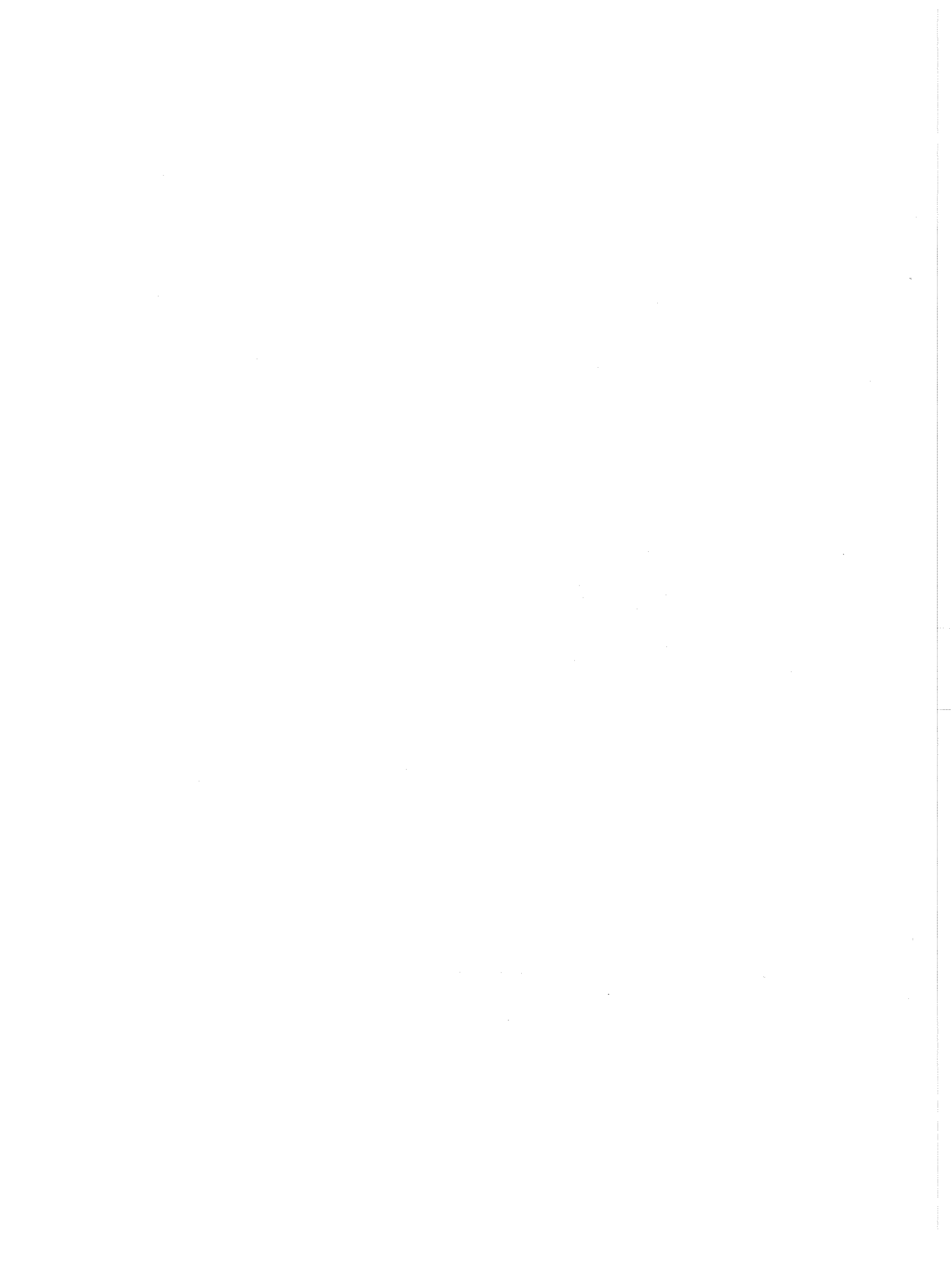


Figure D-23. Lineal heating temperature-time curve ($X = 1.9$, run 2).



E. Flow Pattern Temperature Profile Curves

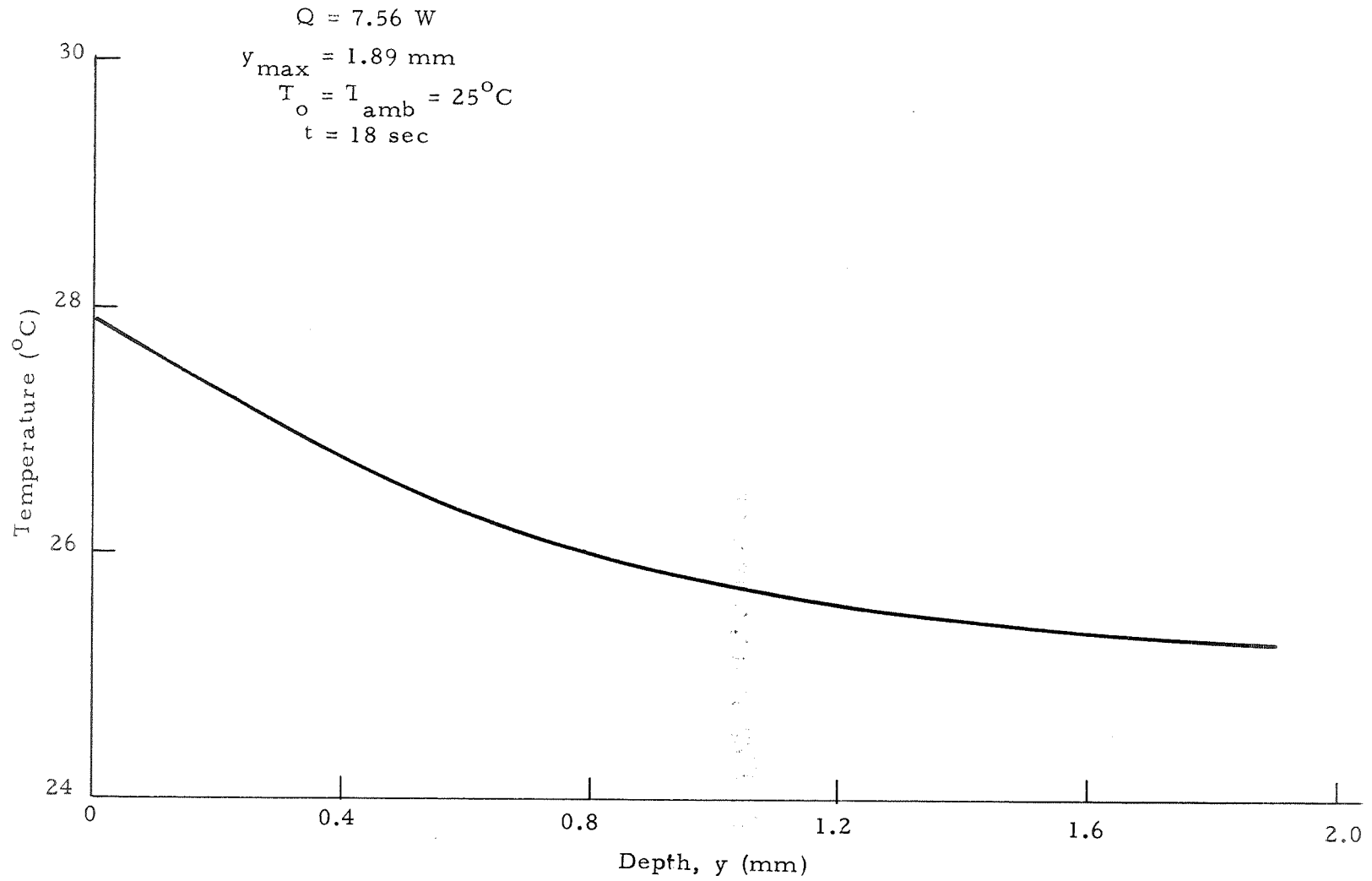


Figure D-24. Flow pattern temperature profile curve ($Q = 7.56$, $t = 18$, $T_a = 25^\circ$, $y_m = 1.89$).

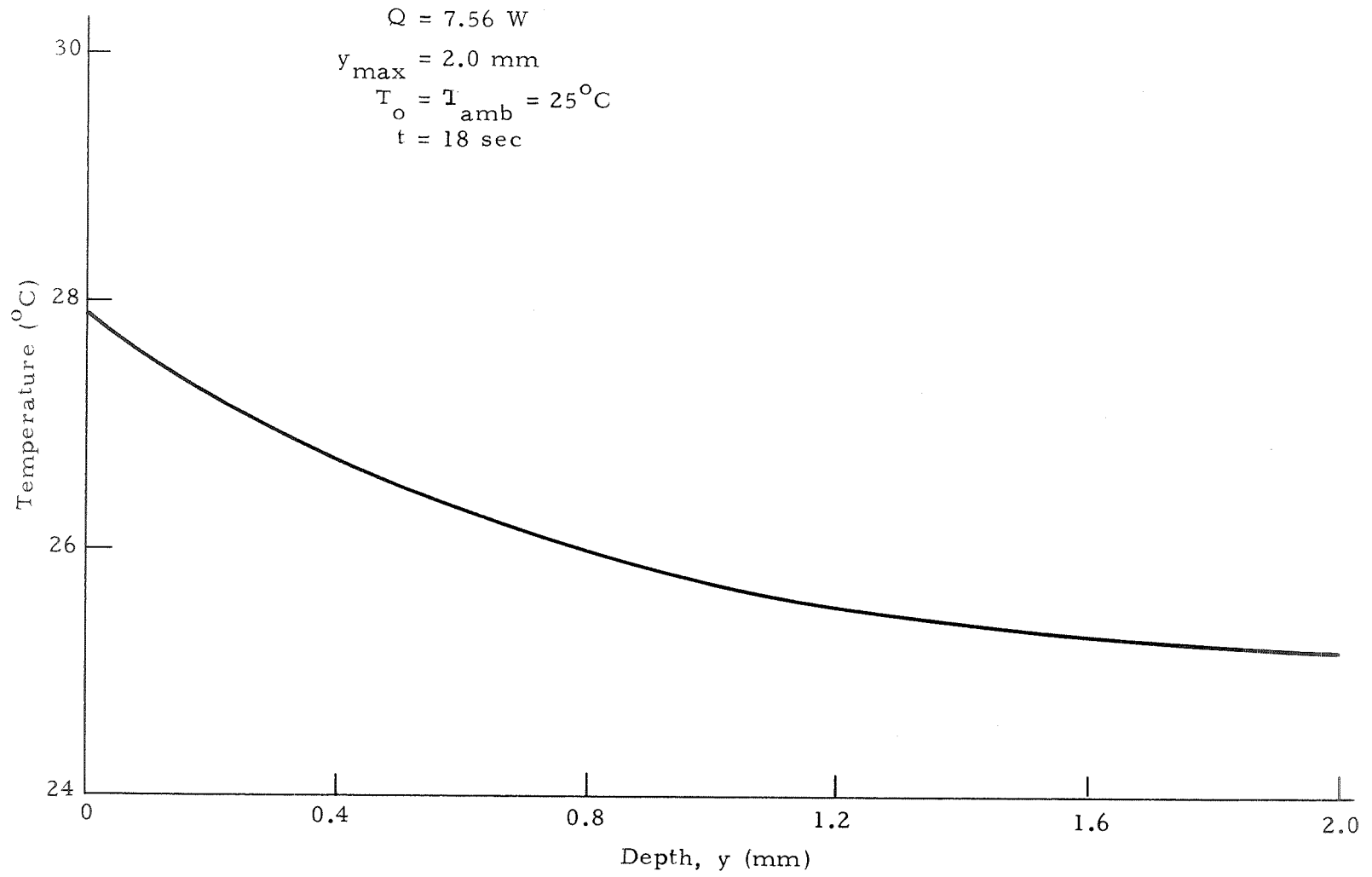


Figure D-25. Flow pattern temperature profile curve ($Q = 7.56$, $t = 18$, $T_a = 25^\circ$, $y_m = 2.0$).

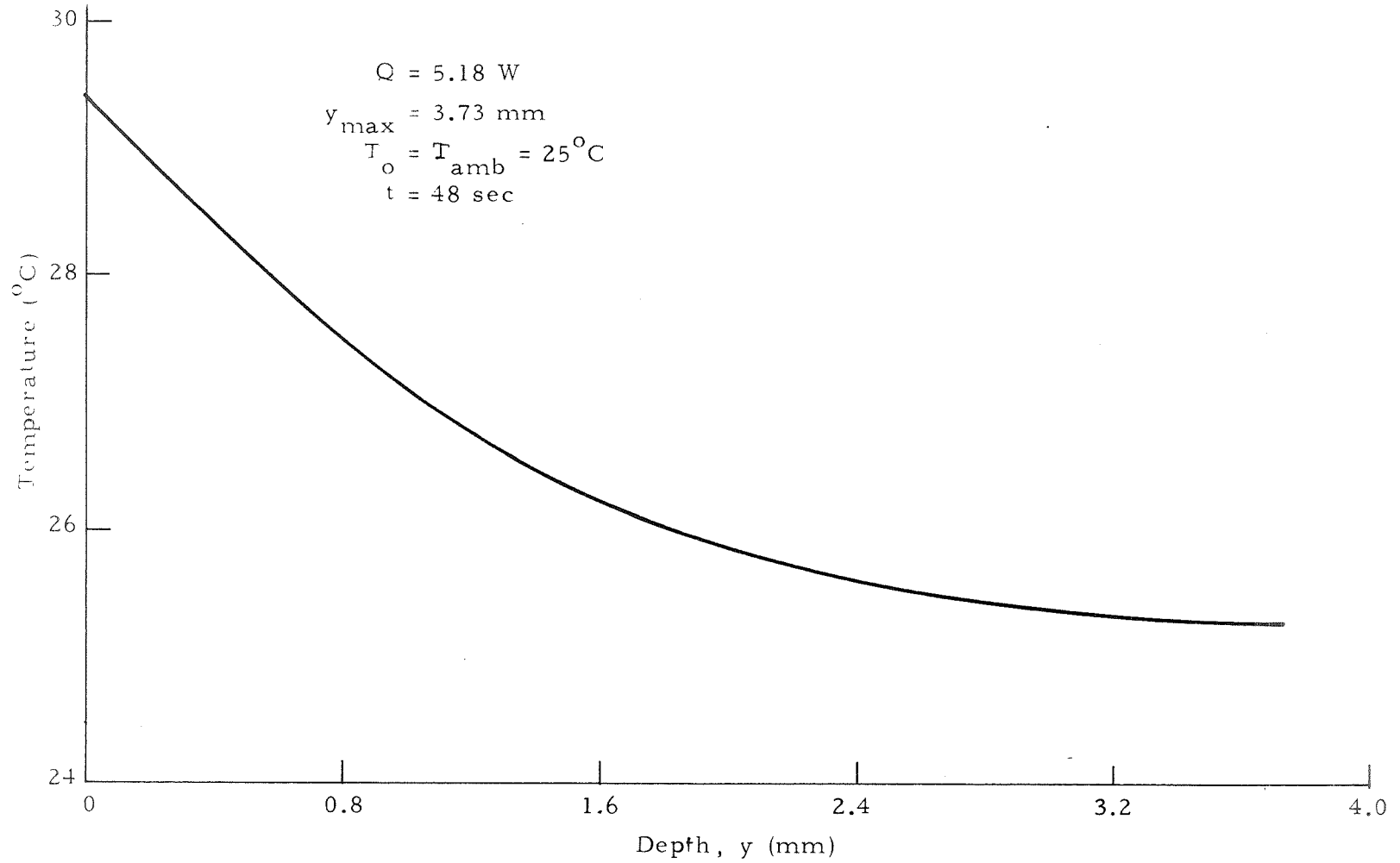


Figure D-26. Flow pattern temperature profile curve ($Q = 5.18$, $t = 48$, $T_a = 25^{\circ}$, $y_m = 3.73$).

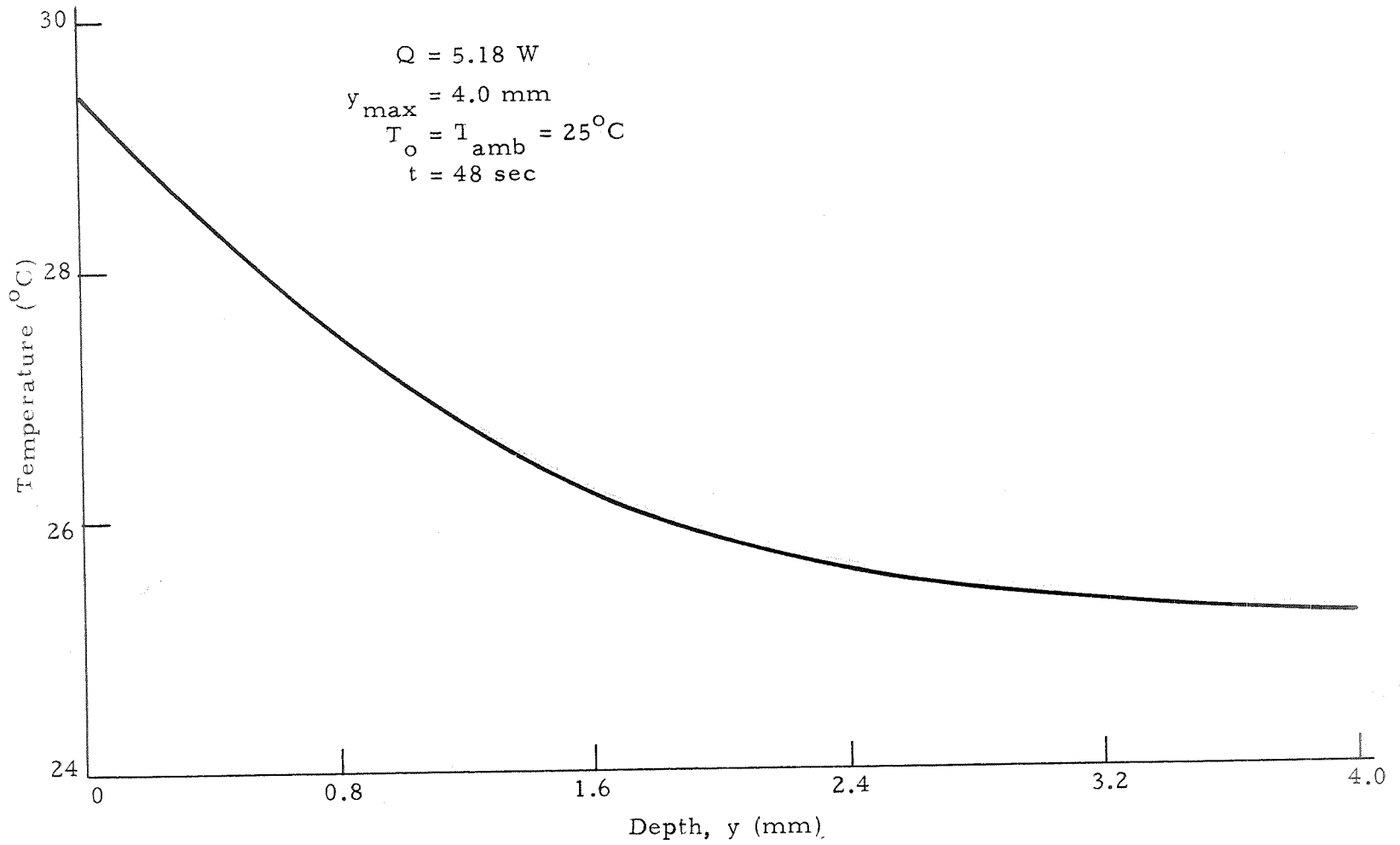


Figure D-27. Flow pattern temperature profile curve ($Q = 5.18$, $t = 48$, $T_a = 25^\circ$, $y_m = 4.0$).

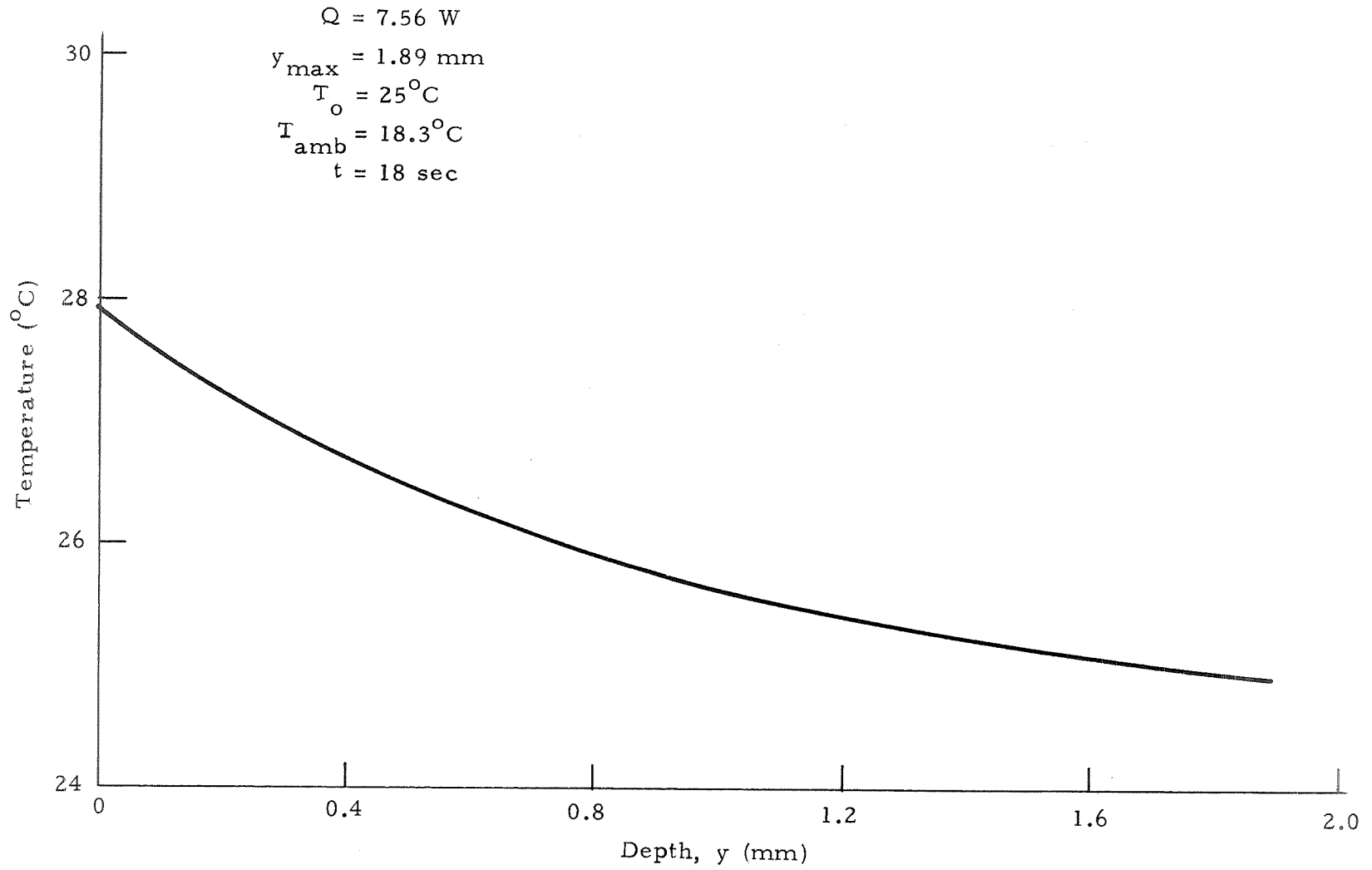


Figure D-28. Flow pattern temperature profile curve ($Q = 7.56$, $t = 18$, $T_a = 18.3^\circ$, $y_m = 1.89$).

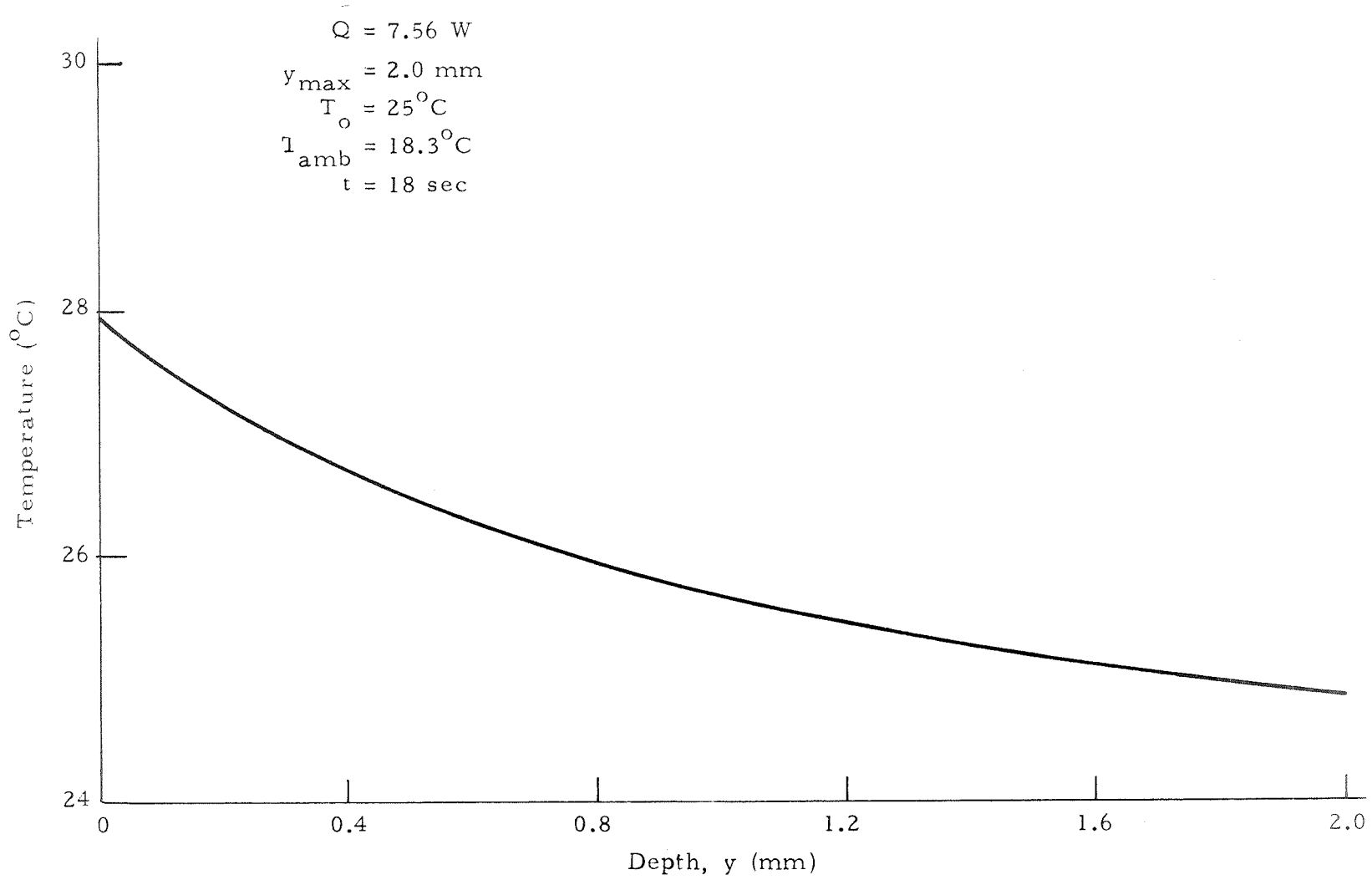


Figure D-29. Flow pattern temperature profile curve ($\bar{Q} = 7.56$, $t = 18$, $T_a = 18.3^\circ$, $y_m = 2.0$).

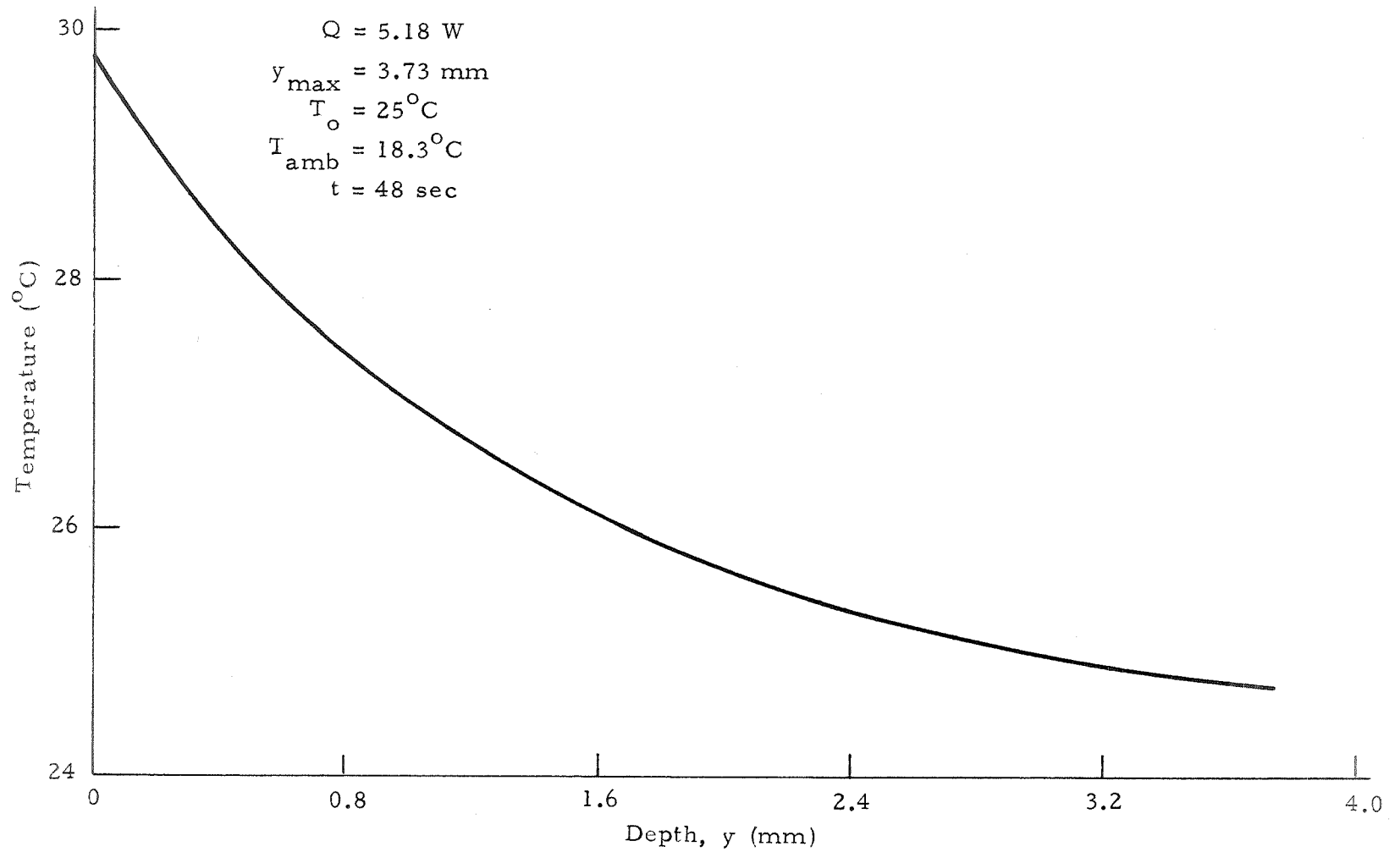


Figure D-30. Flow pattern temperature profile curve ($Q = 5.18$, $t = 48$, $T_a = 18.3^{\circ}$, $y_m = 3.73$).

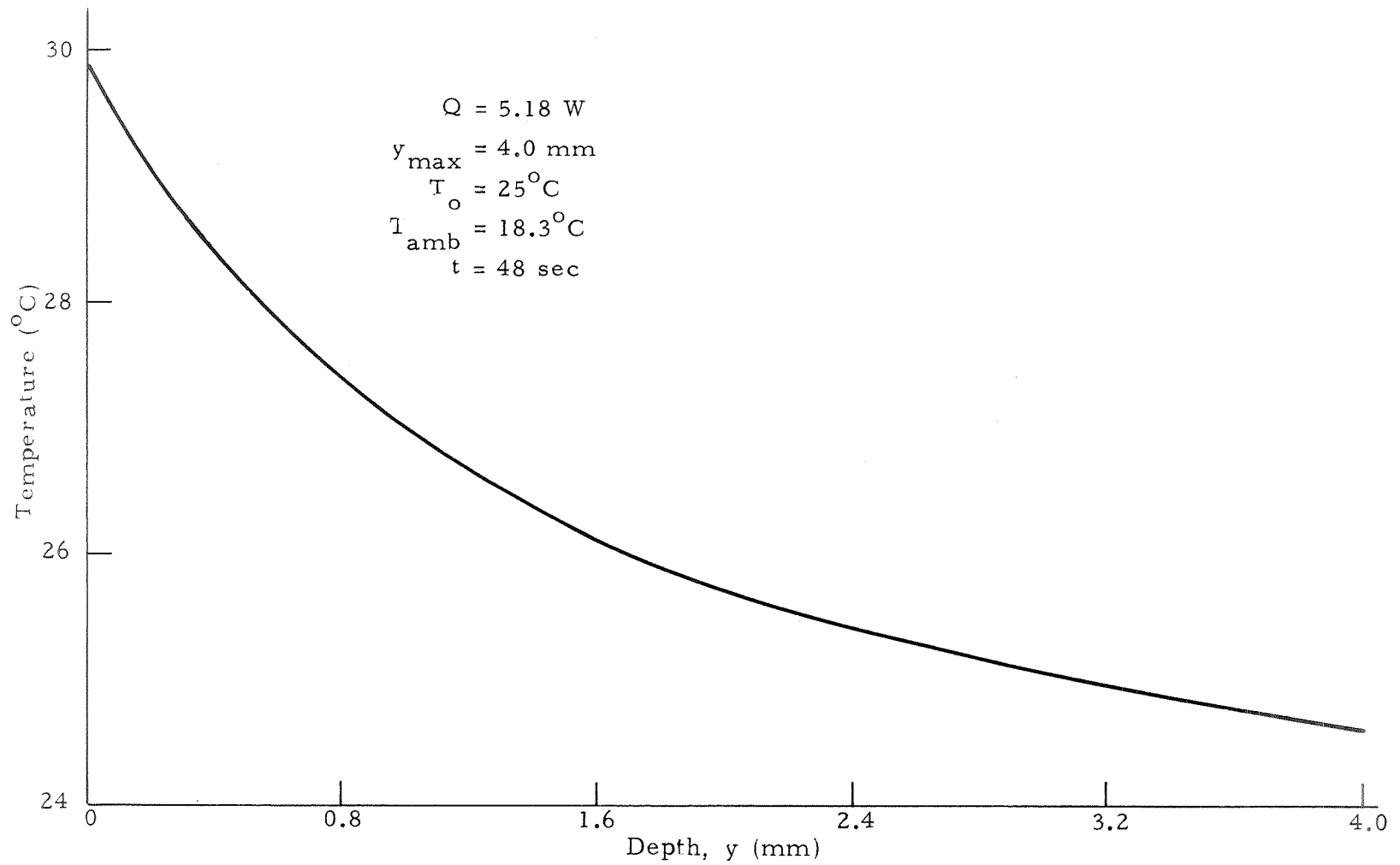


Figure D-31. Flow pattern temperature profile curve ($Q = 5.18$, $t = 48$, $T_a = 18.3^\circ$, $y_m = 4.0$).

APPENDIX E

LOCKHEED GENERAL CONVECTION PROGRAM (LGCP)

Convection modeling consists of analyzing the fluid flow and heat transfer simultaneously. These mechanisms are coupled since the heat transfer affects the flow velocity and likewise the fluid convection influences the heat transfer. This appendix briefly describes a computer model of convection phenomena which was applied to the Apollo 17 HFC demonstration requirements.

The convection model [33] consists of a numerical solution to the full Navier-Stokes equations for a compressible, viscous, heat conducting fluid. The computer program can currently solve problems for two-dimensional flow in a rectangle and axisymmetric flow between concentric cylinders. The HFC Radial cell configuration consists of the concentric cylinder arrangement.

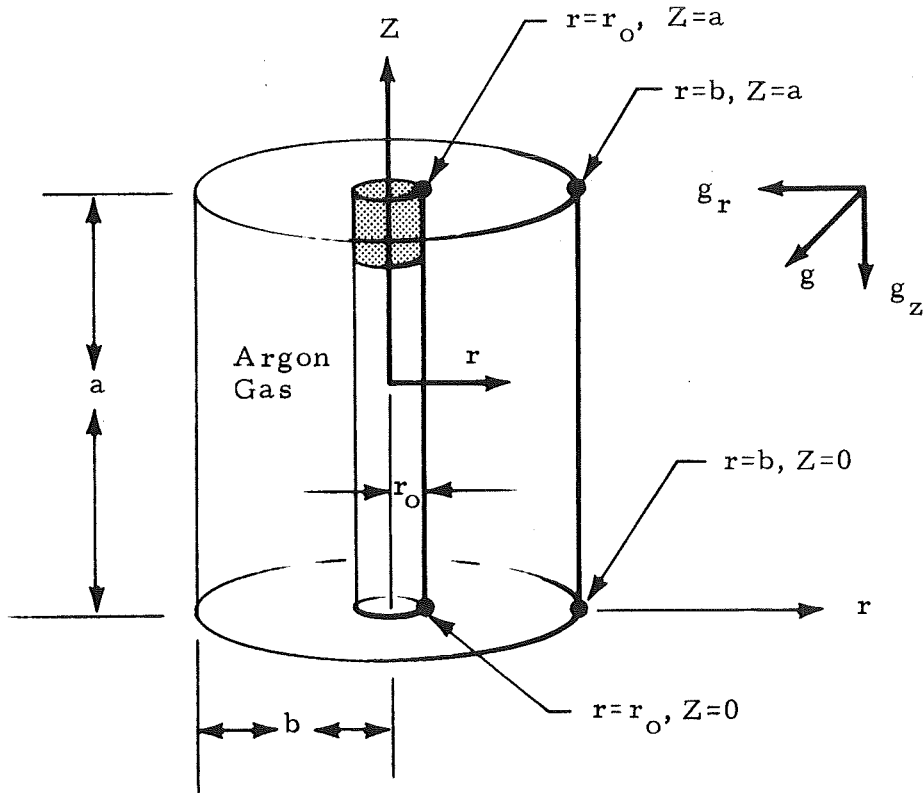
The model contains two possible driving forces for fluid convection. The gravity-induced convection caused by buoyant forces and the thermally-induced expansion convection are included with the gravity vector. The LGCP currently utilizes the following assumptions and simplifications to the Navier-Stokes equations.

- Newtonian fluid obeying Stokes viscosity law.
- Constant thermal properties k , C_v , μ , γ .
- No radiation or internal heat sources.
- No viscous dissipation of energy.
- Ideal gas equation of state ($P = \rho RT$).

The current convection model does not make the classical Boussinesq approximation which neglects the effects of pressure on the density profile. Most models reported in the literature make this assumption resulting in a quasi-incompressible approach. The model used here considers the equations of compressible flow with variable density in all terms.

The geometry and coordinate system used in the convection computer model are shown in the following schematic. This configuration allows the

radial cell experiment to be simulated analytically with both heat conduction and convection included.



The Navier-Stokes equations for the Radial cell are derived by invoking the conservation laws for mass, momentum, and energy. Written in axisymmetric cylindrical coordinates, these governing equations take the following form:

Mass

$$\frac{\partial \rho'}{\partial t'} + \frac{1}{r'} \frac{\partial}{\partial r'} (r' \rho' u') + \frac{\partial}{\partial z'} (\rho' v') = 0 \quad . \quad (E-1)$$

Radial Momentum

$$\begin{aligned} \frac{\partial}{\partial t'} (\rho' u') + \frac{1}{r'} \frac{\partial}{\partial r'} (r' \rho' u'^2) + \frac{\partial}{\partial z'} (\rho' u' v') = \\ - \rho' g_r' - \frac{\partial P'}{\partial r'} + \mu \left(\frac{\partial^2 u'}{\partial r'^2} + \frac{1}{r'} \frac{\partial u'}{\partial r'} - \frac{u'}{r'^2} + \frac{\partial^2 u'}{\partial z'^2} \right) \end{aligned} \quad (E-2)$$

Axial Momentum

$$\begin{aligned} \frac{\partial}{\partial t'} (\rho' v') + \frac{1}{r'} \frac{\partial}{\partial r'} (r' \rho' u' v') + \frac{\partial}{\partial z'} (\rho' v'^2) = \\ - \rho' g_z' - \frac{\partial P'}{\partial z'} + \mu \left(\frac{\partial^2 v'}{\partial r'^2} + \frac{1}{r'} \frac{\partial v'}{\partial r'} + \frac{\partial^2 v'}{\partial z'^2} \right) \end{aligned} \quad (E-3)$$

Energy

$$\begin{aligned} \rho' C_v \left(\frac{\partial T'}{\partial t'} + u' \frac{\partial T'}{\partial r'} + v' \frac{\partial T'}{\partial z'} \right) = \\ - P' \left[\frac{1}{r'} \frac{\partial}{\partial r'} (r' u') + \frac{\partial v'}{\partial z'} \right] + k \left[\frac{1}{r'} \frac{\partial}{\partial r'} \left(r' \frac{\partial T'}{\partial r'} \right) + \frac{\partial^2 T'}{\partial z'^2} \right] \end{aligned} \quad (E-4)$$

State Equation

$$P' = ZR\rho' T' \quad (E-5)$$

These equations, with properly prescribed boundary conditions, describe the flow and thermal behavior of the gas in the Radial cell.

The thermal boundary conditions consist of specified values of temperature or heat flux at the heater post, cylinder wall, base insulation layer, and liquid crystal strip. These velocity boundary values consist of a no-slip

($V = 0$) condition at the solid interface and a symmetric condition ($\partial V/\partial r = 0$) at the "top" of the heater post. The boundary values for the solid surfaces were calculated first using the pure conduction assumption and then corrected for convection heat transfer into the argon gas.

The thermal convection computer program utilizes a finite-difference numerical solution to the full Navier-Stokes equations. The program allows the direction and magnitude of the acceleration vector to be arbitrary. A unique capability of the program is the coupling of gravity convection and thermoacoustic convection. This capability is necessary for analyzing the HFC Radial cell since both types of convection could occur in this cell.

The same basic nodal breakdown used in the conduction model (Fig. D-1) was also used for the convection model. However, the number of node points was doubled to insure accuracy in the fluid-flow calculations. An error analysis of this type of model consists of essentially the same error bands as the thermal models discussed previously. The primary purpose of this type of modeling is to determine if convection occurred in the flight experiment and to estimate the magnitude of the increased heat transfer. In addition, this type of modeling allowed the Apollo 14 and Apollo 17 data to be compared to similarities and differences in convection aspects.

APPENDIX F

REVIEW OF GEBHART'S THEORY OF RANDOM CONVECTION

The paper by Gebhart [34] deals directly with convection caused by random disturbances likely to prevail in spacecraft. Sources for these bumps or impulses in the spacecraft include motion of the occupants, attitude control measures, particle impacts, and internal mechanical events. The effect of the fluctuations on a contained fluid were considered to be transferred to the fluid by normal and shear stresses. The former are associated with velocity fluctuations, whereas the latter are attributed to orientation changes caused by relative motion between boundary surfaces and the enclosed fluid. Assuming that shear stresses account for most of the convection, Gebhart obtained a relation between Nusselt number (comparison of random convection and pure conduction) and elapsed time between impulses. This relation is shown in Figure F-1 for various container geometries. Time intervals between bumps are proportional to F_m , which is a mean disturbance Fourier number. The disturbance Fourier number, F , is defined by the following relationship:

$$F = \frac{\alpha \tau_c}{s^2} ,$$

where

$$\begin{aligned} \alpha &= \text{thermal diffusivity} \\ \tau_c &= \text{time between disturbances} \\ s &= \text{significant dimension} \end{aligned} .$$

The equations which relate the average Nusselt number to the disturbance Fourier number are:

Plane, One-Dimensional Case

$$\overline{Nu} = \frac{C_n}{F_m^{1/2}} .$$

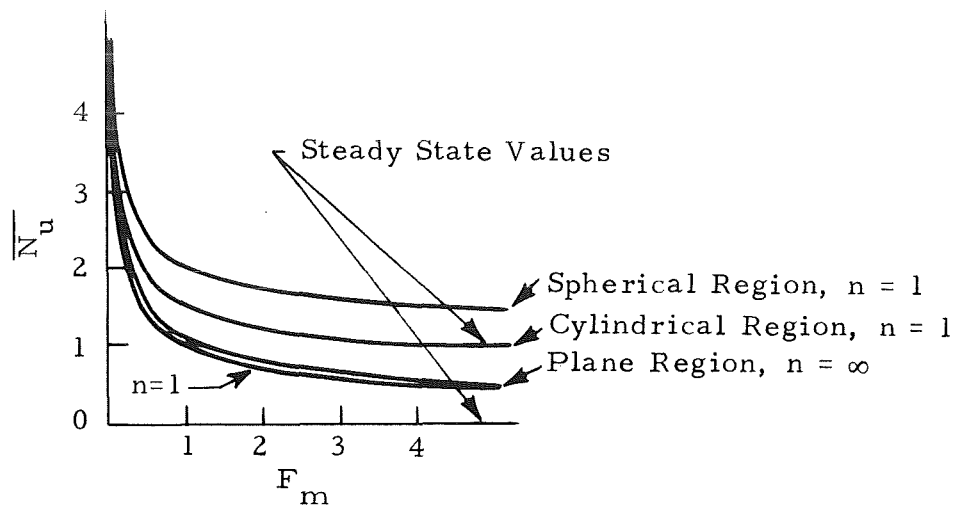


Figure F-1. Effect of disturbances on heat transfer [34].

Spherical Regions

$$\overline{Nu} = 1 + \frac{C_n}{F_m^{\frac{1}{2}}} .$$

Cylindrical Regions

$$\overline{Nu} = \frac{1}{2} + \frac{C_n}{F_m^{\frac{1}{2}}} .$$

The C_n term is an n -dependent constant where n is an integer in the probability distribution used and $(n + 1)$ corresponds to the number of independent variables causing the vibration. Values of C_n for various values of n are given as follows:

n	1	2	3	∞
C_n	1	1.061	1.083	1.128

The analysis treats only small amplitude vibrations. It does not take into account substantial fluid flow that would result from large amplitude disturbances. However, the analysis should give order of magnitude effects. An increase in heat transfer between 300 to 400 percent is predicted during frequent impulses of small amplitude.

REFERENCES

1. Von Braun, W.: Factories in Space. Popular Science, December 1969.
2. Yaffee, M. L.: Space Factory Planned for 1970s. Av. Week Space Tech., November 10, 1969, pp. 61-71.
3. Wuenscher, Hans F.: Exploiting Gravity Fields Less than 1G: Manufacturing in Space. Astronautics and Aeronautics, vol. 10, no. 9, September 1972, pp. 42-54.
4. Space Processing and Manufacturing Meeting. Oct. 21 and 22, 1969, Marshall Space Flight Center, Huntsville, Alabama; NASA TM X-53993, February 5, 1970.
5. Grodzka, P.G.: Types of Natural Convection in Space Manufacturing Processes: Summary Report. Lockheed Missiles and Space Co., Huntsville Research and Engineering Center, LMSC-HREC-TR D306350, January 1973.
6. Grodzka, P.G.; and Fan, C.: Natural Convection in Space Manufacturing Processes: Interim Report. Lockheed Missiles and Space Co., Huntsville Research and Engineering Center, LMSC-HREC D162926, July 1971.
7. Grodzka, P.G.: Zero-Gravity Solidification. Lockheed Missiles and Space Co., Huntsville Research and Engineering Center, LMSC-HREC D148619-A, March 1970.
8. Bannister, T.C.: Heat Flow and Convection Demonstration (Apollo 14). NASA TM X-64735, March 29, 1973.
9. Grodzka, P.G.; Fan, C.; and Hedden, R.O.: The Apollo 14 Heat Flow and Convection Demonstration Experiments: Final Results of Data Analyses. Lockheed Missiles and Space Company, Huntsville Research and Engineering Center, LMSC-HREC D225333, September 1971.
10. Grodzka, P.G.; and Bannister, T.C.: Heat Flow and Convection Demonstration Experiments Aboard Apollo 14. Science, vol. 176, May 1972, pp. 506-508.

REFERENCES (Continued)

11. Bannister, T.C.: Heat Flow and Convection Demonstration Experiments Aboard Apollo 17 (Early Results). Marshall Space Flight Center, MSFC Research and Technology Review, February 22-23, 1973. (Available from Author).
12. Johnson, P.T.: Apollo 17 Heat Flow and Convection Demonstration: Description and Experimental Operating Procedures. Lockheed Missiles and Space Co., Huntsville Research and Engineering Center, LMSC-HREC D225415-B, October 1971.
13. Gatewood, E.; Morris, M.G.; and Holland, R.L.: Acceleration Levels on the Heat Flow and Convection Demonstration. NASA TM X-64644, February 11, 1972.
14. Pearson, J.R.A.: On Convection Cells Induced by Surface Tension. *J. Fluid Mech.*, vol. 4, 1958, pp. 489-500.
15. Nield, D.A.: Surface Tension and Buoyancy Effects in Cellular Convection. *J. Fluid Mech.*, vol. 19, 1974, pp. 341-352.
16. Scriven, L.E.; and Sternling, C.V.: On Cellular Convection Driven by Surface-Tension Gradients: Effects of Mean Surface Tension and Surface Viscosity. *J. Fluid Mech.*, vol. 19, 1969, pp. 321-340.
17. Smith, K.A.: On Convective Instability Induced by Surface-Tension Gradients. *J. Fluid Mech.*, vol. 24, 1965, pp. 401-414.
18. Palmer, H.J.; and Berg, J.C.: Convective Instability in Liquid Pools Heated from Below. *J. Fluid Mech.*, vol. 47, 1971, pp. 779-787.
19. Bentwich, M.: Buoyancy and Surface-Tension Induced Instabilities of Fluid in Open and Closed Vertical Cylindrical Containers. *Appl. Sci. Res.*, vol. 24, July 1971, pp. 305-328.
20. Sparrow, E.M.; Goldstein, R.J.; and Jonsson, V.K.: Thermal Instability in a Horizontal Fluid Layer: Effect of Boundary Conditions and Non-Linear Temperature Profile. *J. Fluid Mech.*, vol. 18, 1963, p. 513.

REFERENCES (Continued)

21. Gershuni, G.Z.; Zhushovitskii, E.M.; and Iurkov, I.S.: On Convective Stability in the Presence of Periodically Varying Parameter. *PMM*, vol. 34, no. 3, 1970, pp. 470-480.
22. Gresho, P.M.; and Sani, R.L.: The Effect of Gravity Modulation on the Stability of Heated Fluid Layer. *J. Fluid Mech.*, vol. 40, 1970, pp. 783-806.
23. Vidal, A.; and Acrivos, A.: Effect of Nonlinear Temperature Profiles on the Onset of Convection Driven by Surface Tension Gradients. *I&EC Fundamentals*, vol. 7, February 1968, pp. 53-58.
24. Currie, I.G.: The Effect of Heating Rate on the Stability of Stationary Fluids. *J. Fluid Mech.*, vol. 29, 1967, pp. 337-347.
25. Berg, J.C.; Acrivos, A.; and Boudart, M.: Evaporative Convection. *Advanc. Chem. Eng.*, vol. 6, 1966, p. 102.
26. Debler, W.R.; and Wolf, L.W.: The Effects of Gravity and Surface Tension Gradients on Cellular Convection in Fluid Layers with Parabolic Temperature Profiles. *J. Heat Transfer, Trans. ASME*, August 1970, pp. 351-358.
27. Soberman, R.K.: Onset of Convection in Liquids Subjected to Transient Heating from Below. *Physics of Fluids*, vol. 2, 1959, pp. 131-138.
28. Jeffereys, H.: The Surface Elevation in Cellular Convection. *Quart. J. Mech. and Appl. Math.*, vol. 4, pt. 3, 1951, pp. 283-288.
29. Hoard, C.Q.; Robertson, C.R.; and Acrivos, A.: Experiments on the Cellular Structure in Bénard Convection. *Int. J. Heat Mass Transfer*, vol. 13, 1970, pp. 849-856.
30. Koschmieder, E.L.: On Convection under an Air Surface. *J. Fluid Mech.*, vol. 30, 1967, pp. 9-15.
31. Batchelor, G.K.: Heat Transfer by Free Convection Across a Closed Cavity Between Vertical Boundaries at Different Temperatures. *Quart. Appl. Math.*, vol. 12, October 1954, p. 214.

REFERENCES (Concluded)

32. Eckert, E.R.G.; and Carlson, W.D.: Natural Convection in an Air Layer Enclosed between Two Vertical Plates with Different Temperatures. *Int. J. Heat Mass Transfer*, vol. 2, 1961, pp. 106-120.
33. Spradley, L.W.; Bourgeois, S.V.; Fan, C.; and Grodzka, P.G.: A Numerical Solution for Thermoacoustic Convection of Fluids in Low Gravity: Summary Report. NASA CR-2269, May 1973.
34. Gebhart, B.: Random Convection Under Conditions of Weightlessness. *AIAA J.*, vol. 1, 1973, pp. 380-383.
35. Pak, H.Y.; Winter, E.R.F.; and Schoenals, R.J.: Convection Heat Transfer in Contained Fluid Subjected to Vibration. In *Augmentation of Convective Heat and Mass Transfer*, A.E. Bergles and A.L. Webb, eds., ASME, N.Y., 1970, p. 148.
36. Koft, A.: Hoffmann LaRoche Report RCR 14444.
37. Spiegel, E.A.: Convection in Stars. I. *Annual Review of Astronomy and Astrophysics*, vol. 9, 1971, pp. 323-352.
38. Takashima, M.: Thermal Instability of Fluid Layer Bounded Below by Solid of Finite Conductivity. *J. Phys. Soc. Japan*, vol. 31, no. 1, July 1971, pp. 283-292.
39. Ostrach, S.: Role of Analysis in the Solution of Complex Physical Problems. *Third Intl. Heat Trans. Conf.*, Chicago, August 1966.
40. Churchill, S.; and Hellums, J.D.: Dimensional Analysis of Natural Convection. *Chem. Engr. Prog. Symp. Ser.*, vol. 57, 1964, p. 75.
41. Lovin, J.K.; and Spradley, L.W.: User's Manual, Lockheed Orbital Heat Rate Package. LMSC-HREC D162218, Lockheed Missiles and Space Company, Inc., April 1970.
42. Lovin, J.K.: Lockheed-Huntsville Thermal Analyzer. TM 54/20-338, LMSC-HREC D225095, Lockheed Missiles and Space Company, Inc., Huntsville, Ala., July 1972.

APPROVAL

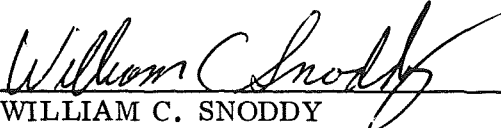
APOLLO 17 HEAT FLOW AND CONVECTION EXPERIMENTS

FINAL DATA ANALYSES RESULTS


By T. C. Bannister, P. G. Grodzka, L. W. Spradley
S. V. Bourgeois, R. O. Hedden, and B. R. Facemire

The information in this report has been reviewed for security classification. Review of any information concerning Department of Defense or Atomic Energy Commission programs has been made by the MSFC Security Classification Officer. This report, in its entirety, has been determined to be unclassified.

This document has also been reviewed and approved for technical accuracy.



WILLIAM C. SNODDY
Chief, Electromagnetic and Solid State
Physics Division



CHARLES A. LUNDQUIST
Director, Space Sciences Laboratory

DISTRIBUTION

Internal

DIR Dr. R. Petrone	S&E-ASTN-MEV Mr. R. Ruff Ms. M. Johnston	S&E-AERO-Y Mr. W. Vaughan
DEP Dr. W. Lucas Mr. J. Shepherd	S&E-ASTN-MT Mr. A. Krupnick Dr. R. Snyder Dr. R. Allen	S&E-AERO-YE Mr. O. Vaughan
AD-S Dr. E. Stuhlinger Dr. G. Bucher Mr. M. Kent	S&E-COMP-DIR Dr. H. Hoelzer	S&E-SSL-DIR Dr. C. Lundquist Mr. R. Hembree
S&E-DIR Dr. H. Weidner Mr. L. Richard Dr. W. Haeussermann Mr. B. Montgomery	S&E-COMP-RRF Mr. F. Rodrigue Mr. R. Graham	S&E-SSL-X Dr. J. Dozier
SAT-MGR Mr. R. Smith	S&E-PE-DIR Dr. M. Siebel Mr. H. Wuenscher	S&E-SSL-S Dr. W. Sieber Mr. B. Blake (5) Mr. L. Russell
SAT-E Mr. L. Ginn (5)	S&E-PE-A Mr. B. Yates Mr. R. Berge	S&E-SSL-T Mr. W. Snoddy Mr. T. Bannister (30) Mr. G. Arnett Mr. E. Miller Mr. B. Jones
PD-MP-P Mr. H. Dudley Mr. K. Hudson Mr. T. Carey Mr. K. Taylor	S&E-PE-M Mr. J. Williams	S&E-SSL-TR All Members (25)
S&E-R-DIR Dr. W. Johnson	S&E-PE-MW Mr. G. Parks Mr. V. Yost Mr. E. Hasemeyer	S&E-SSL-P Dr. R. Naumann
S&E-ASTN-DIR Mr. K. Heimburg Mr. J. Kingsbury	S&E-PE-MX Mr. P. Schuerer Mr. R. Nichols Mr. G. Adams	S&E-SSL-PM Mr. R. Holland Mr. J. Parker
S&E-ASTN-P Mr. H. Paul	S&E-QUAL-EX Mr. J. Boggess	S&E-SSL-N Dr. R. Decher
S&E-ASTN-M Mr. R. Schwinghamer Mr. E. Cataldo	S&E-QUAL-ATE Mr. D. Taylor	S&E-SSL-C Reserve (5)
S&E-ASTN-MM Mr. E. McKannan Mr. R. M. Poorman	S&E-QUAL-ATA Mr. F. Dolan	A&PS-PAT Mr. L. Wofford
		A&PS-MS-IP (2) A&PS-MS-IL (8) A&PS-MS-H A&PS-TU (6)

External

National Aeronautics and Space Administration Washington, D.C. 20546 Attn: E/Dr. C. Mathews ES/Mr. F. Williams Mr. J. Bredt (5) M/Mr. D. Myers MA/Mr. C. Lee MAE/Mr. L. Casey MTX/Mr. W. Armstrong RS/Mr. D. Novik RW/Mr. G. Deutsch RRT/Dr. R. Nash SL/Mr. W. Keller SM/Dr. R. Allenby Col. D. Senich	Howard University Washington, D.C. 20001 Attn: Dr. A. Ukanwa	Lockheed Missiles and Space Co. Research Park Huntsville, Alabama 35807 Attn: Mr. J. Farrior Mr. G. Reny Mr. J. Benefield Dr. P. Grodzka (5) Mr. R. Hedden Dr. S. Bourgeois Mr. L. Spradley Mr. P. Johnston Mr. P. Biscenius Mr. K. Heimendinger Mr. R. Wyman Mr. R. Chaney Mr. A. Marino Mr. R. Osmer
NASA, Johnson Space Center Houston, Texas 77058 Attn: AA/Dr. C. Kraft CB/Col. Stuart A. Roosa Cmdr. Ronald E. Evans CD2/Ms. J. Lee CD12/Mr. C. Perner ED2/Mr. E. Weeks EP5/Mr. R. Rice FC4/Mr. L. Hirsh PD9/Mr. G. Mulraney PG/Mr. P. Jaschke Mr. J. DeLeonardis Mr. F. Laurentz PH/Mr. N. Stewart SN/Mr. B. Miller	University of Southern California Los Angeles, California 90007 Attn: Professor W. Wilcox	Dr. J.R.A. Pearson Department of Chemical Engineering University of Cambridge Cambridge, England
Director NASA, Langley Research Center Langley Station Hampton, Virginia 23365	Case Western Reserve University Cleveland, Ohio 44106 Attn: Professor S. Ostrach	Dr. D.A. Nield Department of Mathematics University of Auckland Auckland, New Zealand
Jet Propulsion Laboratory, 180-302 California Institute of Technology 4800 Oak Grove Drive Pasadena, California 91103 Attn: Mr. E. Christensen	Lehigh University Bethlehem, Pa. 18016 Attn: Professor H. Leidheiser	Professor B. Gebhart College of Engineering Upson Hall Cornell University Ithaca, N.Y. 14850
The University of Texas Austin, Texas 78712 Attn: Dr. L. Koschmeider	University of Pennsylvania Philadelphia, Pa. 19104 Attn: Professor S. Churchill	Dr. Peter D. Richardson Division of Engineering Brown University Providence, Rhode Island 02912
	Massachusetts Institute of Technology Charles Stark Draper Laboratories 68 Albany Street Cambridge, Massachusetts 02139 Attn: Dr. H. Gatos Dr. A. Witt Dr. J. Melcher	Dr. John Carruthers Bell Research Labs Murray Hill, New Jersey 07974
	Scientific and Technical Information Facility (25) P. O. Box 33 College Park, Maryland 20740 Attn: NASA Representative (S-AK/RKT)	Dr. John Berg University of Washington Seattle, Washington 98105
		Hayes International Corp. P. O. Box 1568 Huntsville, Alabama 35807 Attn: W.T. Weissinger